UNIVERSITY OF SOUTHAMPTON

Remote Spectroscopic Monitoring of Liquids Via Silica Optical Fibres

by

Steven James Mackenzie

Department of Electronics and Computer Science

The Optoelectronics Research Centre

A thesis submitted for the degree of PhD December 1997

UNIVERSITY OF SOUTHAMPTON

ABSTRACT

FACULTY OF ENGINEERING
ELECTRONICS AND COMPUTER SCIENCE
Doctor of Philosophy

REMOTE SPECTROSCOPIC MONITORING OF LIQUIDS VIA SILICA OPTICAL FIBRES

by Steven James Mackenzie

This thesis describes advances in the modelling and characterisation of sampling techniques and extrinsic optical fibre sensors for remote or on-line emission spectroscopy of liquids, using the inelastic scattering processes of Raman and fluorescence spectroscopy.

A semiconductor laser has been used as an excitation source, coupled via an optical fibre to a measurement cell; the collected light has been analysed with a spectrograph based around a holographically-produced concave diffraction grating and a cooled CCD detector. Its design, construction, and performance are described. This equipment has been interfaced to a PC, which has been programmed to direct excitation light alternately between two measurement cells, and process the signals from them, to achieve optimum rejection of interference from the measured data.

A mathematical model of the scattered-light collection efficiency of a number of optical-fibre probes, including parallel-optical-fibre and single-fibre types has been derived, and shown to be valid within experimental error. The model variables include the optical fibre numerical aperture and core radius (both of which may be different for each fibre in the probe), axial separation of the probe fibres, and analyte refractive index and absorption. Several representative optical-fibre probe configurations are compared in the light of this new model.

The interface between optical-fibre probes and various novel light-guiding sampling arrangements has been investigated. Mathematical models of coupling between fibre probe and sample cell, and the signal enhancements achieved by using various cell configurations, have been derived. These have been compared with experimental results from Fresnel-reflection light-guiding cells, metallic-reflection light-guiding cells, and waveguiding cells based on low-refractive index polymer films and free-falling streams of analyte. The model includes sample absorption, and accounts for the reflectivity and surface quality of the cell walls, and it has been shown to be more complete and accurate than any previously published work on the topic. In particular, no previous references had been found on the use of the low-refractive index polymer Teflon-AF as a waveguide cladding, or the use of free-falling water streams for the enhancement of collected light in spectroscopic work.

The cell configurations will enhance the scattered light collection efficiency of any parallel-optical-fibre probe: by coupling a 100 mm long free-falling stream of an aqueous solution of fluorescent dye with a parallel-optical-fibre probe, the measured light collection efficiency of the fibre probe increased by 9 times in this work.

Remote Spectroscopic Monitoring of Liquids Via Silica Optical Fibres

Contents

Acknowledgements

Mark Johnson (of North West Water) and John Dakin proposed this project, and its initial direction, to evaluate the potential of optical-fibre chemical sensing in water industry applications, and they have provided patient advice and motivation throughout. There are, of course, many other people who have also freely given their time and experience to me during my work, only some of whom can be mentioned here.

Professor Hendra, and all in the Raman Spectroscopy group, have provided sound advice, opinion, and use of their equipment, especially at the beginning of my work. It has been a privilege to work in the ORC, and to benefit from the knowledge and expertise of the people within it. The staff in the mechanical workshops of the Physics and Electronics departments have been expert in their interpretation of my requirements, and it is certain that none of the apparatus described in this thesis would work, were it not for their input. In particular, thank you to Ken Frampton and his team in the Zepler Building.

The support staff in the Mountbatten Building have all been helpful in suggesting how I can best start each project I have undertaken, provided me with equipment, and their time. Special thanks to Gary Dempster, who during his time at the ORC in the mechanical workshop fabricated, and helped me to make, many of the early pieces of equipment.

Again, thank you to all my colleagues in the ORC, especially those without whom I may have finished this work more quickly, but it wouldn’t have been so enjoyable; and thank you to Emma for everything.

This work was funded by the EPSRC and North West Water through a CASE grant, and carried out in the Optoelectronics Research Centre at Southampton University.

1. Introduction

Optical fibre based sensing schemes have become accepted in applications as diverse as distributed temperature and strain sensing, motion sensing, and chemical sensing. Fibre techniques have succeeded because they have unique advantages over established sensing methods: advantages such as the immunity of optical signals to electronic interference, the absence of ignition risks in flammable environments, and the ability to make distributed measurements remote from the bulk of the measurement hardware. Several text books, such as that written by Boisdé and Harmer[1], or the compendia edited by Wolfbeis[2], or Dakin and Culshaw[3], describe some of the applications in on-line monitoring and process control that have been fulfilled by optical fibre techniques.

This thesis describes several novel methods and procedures for Raman or fluorescence detection, and how some of the generic methods of sensing chemicals over silica optical fibres can be better quantified and improved. A compact and potentially portable spectroscopic instrument is described, which incorporates recent advances in optical source and detector technologies, and other optical components. It has been interfaced to a number of novel optical-fibre probes and novel sample cells, and to a computer which was programmed to control data acquisition, processing, and recording. This thesis does not describe a single complete optical-fibre, on-line, or remote-chemical-monitoring system, but the elements that are described in this work are the components that would form such a system. The work described has been multi-disciplinary, involving spectroscopy, optics, electro-optics, electronics, and material science.

1.1. Background

There has been a long standing interest in chemical monitoring over standard (*ie* silica) optical fibres, particularly where measurements must be made in inaccessible or hostile environments[4]. Early process monitoring applications measured optical absorption from uranium or plutonium in nuclear power plants; later fluorescence was measured which increased the measured signal to noise ratio[5]. More recently, Raman spectroscopy has been applied in pharmaceutical and petrochemical applications[6].

This project was initially conceived in conjunction with a major utility company, North West Water, to apply Raman spectroscopy over optical fibres to measurement problems in the water industry. For instance, chloroform is formed during the chlorination of tap water if there is any hydrocarbon contamination of the water, and so it would be desirable to continuously monitor for the presence of chloroform or hydrocarbons. Initial calculations (reproduced in appendix A) suggested that this is feasible; however, it has been found that, because of sample fluorescence and other instrumental factors, detection of the levels of contamination of interest to the water industry was not practical with the type of equipment envisaged for use in this project. Contamination limits are specified at the minimum concentration measurable using high precision liquid chromatography techniques: in many cases it could not be hoped to apply optical-fibre sensors with useful accuracy or speed of response. However, the work in this thesis is applicable in many other industries, from brewing to petrochemical processes.

Two basic approaches to sensing using optical fibres are possible: either *direct* optical interaction with an analyte; or *indirect* analysis using chemical indicators, *ie* compounds which change their optical properties by reaction with the analyte. An alternative division of optical fibre sensing schemes can be made: *intrinsic* sensing schemes, in which some measurable property of the probe itself is modulated by the analyte (*eg* transmission through a fibre); and *extrinsic* schemes, in which the optical interaction within the analyte is measured.

Direct, extrinsic techniques have been pursued in this work. These have the advantages that the methods used are non-destructive to the sample under test; they are versatile (one form of probe can be appropriate to many analytes); and response to changes in the environment of the sensor can be rapid. This approach does have the potential disadvantage that it is often not as selective as methods using indicator chemistry, because compounds within a chemical family can exhibit similar optical properties when monitored directly.

1.2. Analytical Techniques

The quantized nature of the universe, most obvious at the atomic and molecular level, allows information about the constituents of matter to be deduced from optical spectra. Because molecules and atoms can only emit or absorb photons (particles of light) with energies that correspond to certain allowed transitions between quantum energy states[7], optical spectroscopy is one of the most valuable tools of the analytical chemist. It can provide a rapid non-destructive analysis of many important compounds and radicals, and optical fibres permit remote on-line monitoring.

The region of the electromagnetic spectrum which is efficiently transmitted (with attenuation below 10 dB/km) by silica optical fibres extends from 600 nm to 1900 nm[8]. This makes the electronic transitions and the overtones of molecular vibrational transitions accessible to remote investigation over standard optical fibres. Over much shorter lengths, near UV spectra can be measured. (For IR analysis, fluoride, silver halide and chalcogenide glasses[9] extend the short range possibilities to about 8000 nm, allowing the fibre-remoted study of vibrational transitions, although such fibres are both expensive and fragile.)

Spectroscopic analysis over optical fibres has been successfully implemented for on-line process control[10][11], and new configurations and techniques are continually being incorporated into sensor schemes. In this section the direct, extrinsic sensing schemes which are appropriate for use in conjunction with optical fibres are listed, with a review of previously published work in those areas.

1.2.1. Transmission spectroscopy

This technique has found wide application in chemical, biological and environmental monitoring and process control, due to its generic nature, safety, and ease of application. In 1988 Boisdé reported that over a kilometre of optical fibre had been installed at French Atomic Energy Commission sites for the purpose of on-line process monitoring[12]. The samples monitored ranged from measurements of a single species in a restricted analytical medium, through simultaneous determination of several species, to trace measurements in a complex medium. In some cases, single wavelength measurements were appropriate; in other cases full spectral measurements were necessary. It was claimed that the first (unpublished) work was done as early as 1974, with differential measurement at wavelengths of 477 nm (absorption peak) and 520 nm (low absorption reference wavelength) monitoring Pu(IV) concentration in aqueous solution.

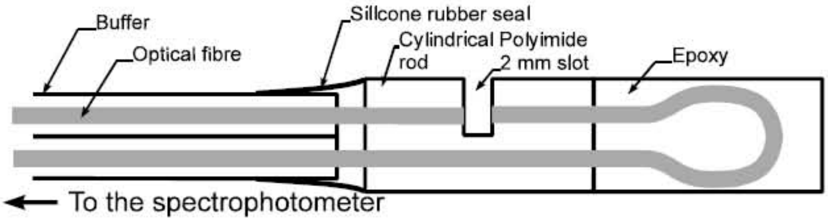

Figure 1.1 An early transmission probe as described by Freeman[13]

The simple fibre-fibre probe of Freeman[13] (figure 1.1), was used to determine copper sulphate concentration in an electroplating bath. Light from a 820 nm LED was coupled into one of the fibres, and a fraction of the light transmitted across the gap was collected by the other fibre. The intensity of this light was then measured by a photomultiplier (although a photodiode could probably have been used). Freeman found excellent correlation between the Cu^{2+} concentration and the absorbance of the light transmitted between the fibres over the concentration range 0.2-0.4 M. Of the other constituents of the plating bath, sulphuric acid was found to influence optical transmission the most, with increased sulphuric acid concentration lowering the apparent absorbance of the solution (probably due to increased solution refractive index, which would decrease the apparent optical pathlength through the solution).

For a simple fibre-to-fibre probe, changes in the refractive index of the analyte can modify the output-light cone angle to a different extent at the reference wavelength than at the measurement wavelength (optical dispersion). This problem can be reduced by lensing the fibres, so that the light is collimated before it enters the sample. Researchers at the Westinghouse Savannah River Company (Aiken, USA) have been developing absorbance probes for in line monitoring since the 1970s[14][15]. A lens assembly from one of their probes is shown in figure 1.2.

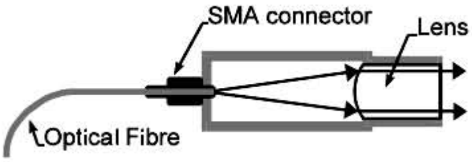

Figure 1.2 Savannah River Company probe lens assembly[14]. The flat front face minimises distortion due to solution refractive index changes.

These probes have been used in pairs, for instance across a process stream, with light transmitted through the analyte from one assembly to another. If the light is collimated when it leaves the flat glass-liquid interface, changes in the refractive index of the analyte have no effect on the intensity of collected light.

An alternative arrangement is to position a mirror facing the end of a single optical fibre. A medical application of a single-fibre probe using a fixed mirror is described by Coleman, who used an optical fibre threaded through a hyper-dermic needle with an aluminium reflector close to its tip[16], as shown in figure 1.3. Coleman described applications for *in vivo* analysis in regions previously too small to sample, and presented *in vitro* measurements of bilirubin in human blood. By using a 25 mW argon ion laser source at 457.8 nm, Coleman measured a minimum detectable absorption coefficient of 0.005 m^{-1} corresponding to bilirubin concentrations between 0.05 M and 1.3 M.

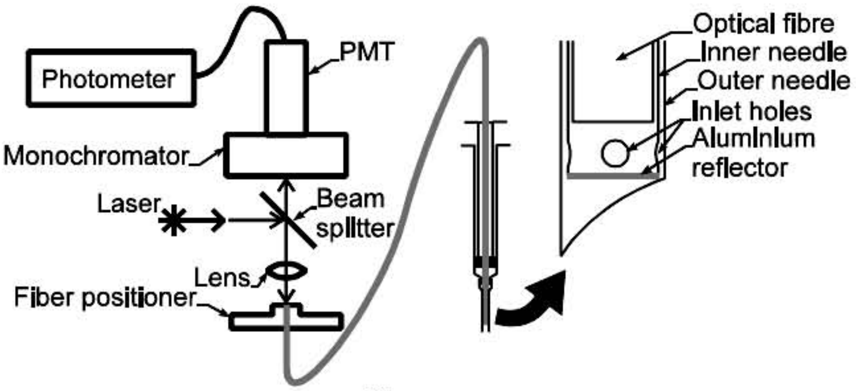

Figure 1.3 *In vivo* arrangement described by Coleman[16]. The optical path length is twice the distance between the fibre tip and the reflector.

1.2.1.1. Diffuse reflectance and evanescent wave spectroscopy

In addition to simply measuring the transmission of a beam of light through a sample, there are other ways in which the qualitative absorption spectrum can be deduced. The first recorded demonstration of an optical fibre absorption measurement (by M Polanyi in 1962)[17], used 50 μm core glass fibres to measure the diffuse reflectance of blood at 805 nm and 660 nm. From these measurements, the absorption spectrum of the blood around 660 nm, and hence its oxygen saturation could be determined. By using the non absorbed wavelength of 805 nm as a reference, fluctuations in parameters such as fibre bending losses could be corrected for. The small size of optical-fibre probe heads (and chemical resistance of silica components) mean that very little interference is caused to any process under observation.

Evanescent wave spectroscopy (an optical fibre variant of attenuated total-internal reflection) is another technique which is used to measure absorbance, but as an intrinsic technique it is not within the scope of this work. It has been compared with emission techniques in appendix A, and shown to offer comparable sensitivity when working with silica fibres.

1.2.2. Photoacoustic spectroscopy

A photoacoustic signal results from the absorption of radiation, followed by dynamic pressure changes due to thermal expansion, and the technique has been applied to gas and liquid phase sensing. Photoacoustic techniques can be very sensitive, and, as part of the collaboration with North West Water during this work, photoacoustic techniques were investigated by Jane Hodgkinson in the laboratories of North West Water[18].

1.2.2.1. Detection of photoacoustic surface movement

In condensed phase samples, a bulk pressure wave may cause the displacement of a free surface, which can be sensitively detected in a number of optical ways[19]. These include measurement of the curvature, gradient, or displacement of the surface.

Hand *et al* have used a fibre-optic Michelson interferometer to measure the displacement of the surface of liquids[20][21]. A pulsed Nd:YAG laser was used as the pump source, directed onto one focus of an elliptical cell. Acoustic waves generated in this region were reflected by the cell walls to form a second focus at the liquid surface of the cell, thus amplifying the displacement. The resulting transient surface deflection was detected with the interferometer (figure 1.4).

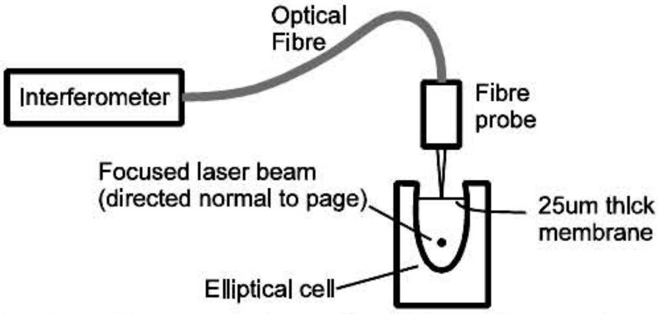

Figure 1.4. Apparatus used to detect surface movement caused by photoacoustic waves in an elliptical cell (modified from Hand[20]).

Using pulsed optical excitation offers a number of advantages, at the expense of an increase in system cost and complexity. The acoustic pulses produced have a large high-frequency component, enabling the short-wavelength pressure waves to be focused by a small cell (a fourfold signal enhancement has been reported[20]); also, time gating the transient response removes any spurious signals arising from absorption at the cell windows, which can otherwise be a significant limiting factor in photoacoustic spectroscopy[22].

1.2.2.2. Detection of photothermal refractive index changes

A photoacoustic volume change may cause a corresponding change in the refractive index of the sample medium, which can be detected using thermal lensing techniques, photothermal deflection, or measurement of the optical path length through a sample.

Thermal lensing and photothermal deflection spectroscopy (PDS) are particularly suited to the analysis of liquid phase samples. Thermal lensing occurs when a beam of light (usually from a laser) is partially absorbed by an analyte, causing a thermal gradient in the fluid. The resulting refractive index changes create a transient lens in the sample, which usually defocuses the beam. This may be detected using a photo-detector having a small acceptance aperture.

In photothermal deflection spectroscopy, higher sensitivity can be gained using a second CW beam, not absorbed by the analyte, to probe the refractive index changes. A detector may be split into two halves, such that a deflected beam has an increased intensity on one half and a decreased intensity on the other. The ratio of the two intensities gives a measurement which is unaffected by changes in the source intensity.

Different possible configurations are: *collinear PDS*, which includes arrangements where the probe beam travels at a small angle to the pump beam, to give a large interaction length, or probe beam parallel with the pump beam, positioned at the point of maximum response (maximum $\partial n/\partial r$); *transverse PDS* arrangements use a probe beam orthogonal to the pump beam.

Bohnert and co-workers have used both collinear and transverse PDS for the trace detection of pesticides in water[23]. A schematic diagram of the apparatus used for transverse operation is shown in figure 1.5.

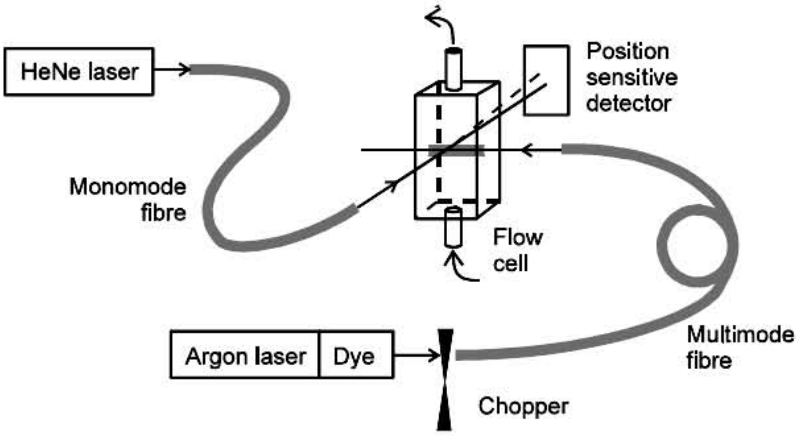

Figure 1.5. Schematic diagram of sample cell used for transverse photothermal spectroscopy of pesticides in water. Picture modified from Bohnert[23].

Transverse PDS was compared with a spectrophotometer (Cary 2400), which had a low noise level corresponding to an absorbance of 0.0002 AU. Detection limits for a number of pesticides were better for the photothermal method, by factors ranging between 2 and 20 for various compounds. Collinear PDS improved the detection limits by a factor of four, so that for example, 2,4-dinitrophenol would be detected at the 0.5 ppb level. The fact that different pesticides responded differently might be explained by differing photoacoustic generation efficiencies for each chemical. Clearly, a strong photoacoustic signal is only possible if the energy absorbed by a molecule is converted to heat rapidly, *ie* within the integration time of the experiment. Other non-thermal relaxation pathways are possible for molecules, including fluorescence.

1.2.3. Fluorescence spectroscopy

Remote monitoring of sample fluorescence via optical fibres is a long standing *in situ* monitoring technique. Measurements made by fibre probes can provide qualitative and quantitative information, with an additional degree of selectivity provided by the choice of excitation wavelength and the fluorescent lifetime of a particular analyte. Although broad band sources can be used to excite fluorescence, lasers are usually preferred for use with optical fibres, as their output is more easily focused to a small spot. The acronym LIF is often used for laser induced fluorescence.

Ground water monitoring of uranium was carried out by workers at the Lawrence Berkeley and Lawrence Livermore laboratories in the US[24]. Their method of uranium detection was based on its fluorescence, when excited at 488 nm by an argon ion laser source. There are strong fluorescence lines at 520 nm, 527 nm and 530 nm and the technique has now been used in the laboratory down to levels of 10^{-14} M.

Because fluorescence bands are quite broad, the additional information provided by fluorescent lifetime measurements is often necessary to distinguish compounds. For instance, Chudyk found that phenol, toluene and xylene (all single-ring aromatic compounds, with peak emission around 295 nm) were initially indistinguishable in their vapour phase[25]. However, by measuring the fluorescent decay time τ with a pulsed 266 nm source, phenol (τ=2.1 ns in cyclohexane[26]) could be easily distinguished from toluene (τ=34 ns) and xylene (τ=31 ns).

The electronics required to perform time-resolved fluorescence spectroscopy (TRFS) has been simplified by Bublitz[27]. By counting photons from the fluorescence in two adjacent arrival-time windows and ratioing the counts, engine oil in water was detected at concentrations below 1 mg/L, and polyaromatic hydrocarbons (PAH) concentration at the μg/L level. The fluorescence was excited by a 2 ns pulse from a multi-gas UV excimer laser, using 248 nm to excite the BTEX compounds (benzene, toluene, ethylbenzene and xylene) and 337 nm for PAHs. Light was emitted between 260 nm and 370 nm for BTEX and between 370 nm and 500 nm for PAHs. The initial laser pulse triggered two gated photon counters, first from 0 to 100 ns, and then from 120 ns to 220 ns after the initial laser pulse.

The light emission from impurities in natural water had a short decay time, and the photons from this source were counted in the first time window. The signal count in the second window was thus due to the longer-decay-time contaminants. By taking the ratio of the two signals the concentration of impurities could be deduced from a look-up table. The PAH emission wavelength coincided with the emission of the natural humic matter, and a further parameter had to be introduced to account for this.

Better detection limits for detecting PAHs *in situ*[28] were achieved by Panne and Neissner. Full TRFS was used, and detection limits down to the ng/L range were achieved for benzo-fluoranthenes and benzo-pyrenes. The probe consisted simply of two 600 μm core diameter silica fibres, angled at 11° to each other, with their end faces close together. The collected light was transmitted to the input of an f/3.8 spectrometer via a circular-to-linear fibre-bundle converter (for increased resolution), and a photodiode array at the focal plane was used to resolve the wavelength spectrum. The laser was pulsed (0.6 ns FWHM) and the detected signal was gated, to integrate for 5 ns at any time after the pulse. After deconvolution of the system response, a time resolution of 0.5 ns was claimed.

A problem that is encountered with high optical power at wavelengths below 350 nm is photo-degradation of the optical fibre. Interaction of intense UV light with silica fibres leads to fluorescence and a decrease of fibre transmission through the formation of colour centres. Although this damage is minimised by using so-called 'UV-enhanced', high OH^- fibre, Hillrichs proposed placing a frequency doubling arrangement at the *probe* end of the transmission fibres[29]. The excitation light is then efficiently transmitted through the fibre at 532 nm, with a relatively low attenuation coefficient (0.16×10^{-4} cm^{-1}, compared with 11.5×10^{-4} cm^{-1} at 266 nm) and without significant photo-degradation of the fibre. Despite the fact that the energy is converted (in a small BBO (BaB_2O_4) nonlinear optical crystal[30]) to 266 nm with only 1% efficiency, Hillrichs calculated that, for fibre lengths over 30 m, this is the most efficient way to transmit light to the sample, and, in any case, avoids cumulative damage to the fibre.

1.2.4. Raman spectroscopy

Fibre-remote Raman spectroscopy has found use in a wide range of process control and remote monitoring applications. The interest in the technique stems from its generality and its compatibility with cheaply available optical fibre components. Qualitative and quantitative information can be deduced from the Raman spectrum of most molecules, without any need for indicator chemistry. Any wavelength of light may be Raman scattered by a molecule, and the optimum for many analyses lies conveniently within the transmission window of silica optical fibres, which efficiently transmit visible and near-IR light (but not the wavelengths used in most IR absorption work). The major weakness of the technique is the low intensity (generally four to six orders of magnitude lower than typical fluorescence) of Raman scattered light, and much work has been done to efficiently collect this light and separate it from any interference.

A common problem in measuring Raman spectra of (in particular) organic molecules is sample fluorescence. By using time resolved methods as described in section 2.4.2 longer lived fluorescence can be eliminated from (effectively instantaneous) Raman scattering by pulsing the excitation light source and gating the detector so that only 'early' Raman light is received. For samples containing only one fluorescent component, Raman light can be separated by phase resolved methods, such as that demonstrated by Demas[31].

Demas demonstrated the nulling of unwanted fluorescence signals from Raman spectra by modulating the excitation light. The fluorescence lifetime of a fluorescent compound is usually significantly greater than that for the Raman scattering process, so the frequency of modulation can be varied until the fluorescence signal is 90° out of phase with the Raman signal. Lock-in detection can then be used to reject the fluorescent light. Demas resolved the Raman spectrum of water from a solution of rhodamine 6G laser dye (excited at 514.5 nm). Although results were good, the phase resolved technique is essentially analogue, and so it is most suitable for use with scanning monochromators (rather than spectrographs using multi element output arrays), which makes for long measurement times. A time constant of one second was used to resolve Raman peaks barely visible in the non-phase resolved measurement, much more successfully than by subtraction of a normalised background measurement of rhodamine fluorescence. Demas postulated that slight errors in the systems cancellation of the fluorescent background may be due to variations of the fluorescent lifetime of two overlapping bands of the single fluorescent molecule, limiting the techniques ultimate sensitivity.

One means of maximising the amount of Raman scattered light generated within a sample is to pass the excitation beam through the cell multiple times, or to use an arrangement in which the excitation light has a large interaction length with the sample and subsequently scattered light is guided to the collection optics. Such an arrangement can be formed using a capillary cell. If the walls of the capillary are sufficiently thin light launched coaxially travels mostly within the analyte. Even better, if the walls of the capillary are made of a material with a lower refractive index than that of the analyte, a waveguide is formed which confines the excitation and scattered light emitted within the collection optics of the spectrograph to the capillary. Walrafen reported enhancements of up to 1000 times by using such capillaries of up to 25 m in length for the Raman spectrum of benzene. Unfortunately large numbers of potential analytes have refractive indices lower than that of silica (1.47), *eg* most aqueous solutions.

The cure process of epoxy resins has been studied using Raman spectroscopy via optical fibre, for instance by Chike[32]. Fully utilising the information available in the Raman scattered light from the material, both the extent of the cure process, and the temperature of the system were measured. The temperature could be measured by comparing the intensity of the anti-Stokes Raman shifted light (light shifted to a shorter wavelength), which changes exponentially with temperature. The variation of the Stokes lines is only slight and hence the ratio of the two measurements can be used to deduce the temperature at the sampling point. The degree of cure was calculated by taking the ratio of the epoxide ring stretch at 1240 cm^{-1} which is linearly dependant on the progress of the cure and the 1186 cm^{-1} vibration of a component not affected by the cure. These results were compared with infra-red absorbance measurements (through 1 mm of sample), and found to be in excellent agreement, and although the infra-red measurements were made at close to optimal conditions, the authors felt that there was room to improve the apparatus for the *in situ* Raman measurement.

The arrangement used to gather the Raman light from within the epoxy composite was simply a pair of parallel 200 μm core optical fibres bonded into an SMA connector, and polished down to a 3 μm finish. This 'pencil probe' arrangement was simply dipped into liquid samples prepared with a suitable epoxide concentrations to simulate the glue at various stages of cure. In practical applications such parallel fibres could be left within the material after cure, possibly for use as sensors for chemical degradation or to measure the temperature of the material in use.

An application in the nuclear industry for which the technique has been investigated is the detection of water in sodium nitrate slurry[33]. Although Raman is not the most obvious technique for this application (water has very strong IR absorption bands and would be easily identified by these) the Raman information would be obtained as a by-product of other measurements made. Two approaches were investigated, first the direct detection of the water bending vibration around 1630 cm^{-1}, and more successfully by taking the ratio of the intensities of the solid sodium nitrate Raman line and the intensity of the dissolved nitrate line (which is shifted by 17 cm^{-1}).

Direct measurements of the 1630 cm^{-1} line of water (chosen in preference to the more intense lines around 3300 cm^{-1} because of its much smaller variation in the presence of electrolytes and with temperature) could be detected down to a concentration of 2.5%. Referencing the intensities of the two phases of the nitrate peak (in conjunction with measurements of the temperature of the system to correct for variations of the solubility of the nitrate) limits of detection below 1% were achieved. Again, only two fibres were used to make these measurements (parallel 400 μm core fibres), so improvements in the collection optics and hence detection efficiencies are possible.

1.3. Summary of This Thesis

This thesis describes the progress made in increasing the range of applications amenable to spectroscopy over optical fibres. An outline of the relevant spectroscopic theory is given in chapter 2, along with details of the experimental equipment and techniques required to resolve optical spectra. This work is concerned with the measurement of optical emission, but absorption and scattering is also discussed in chapter 2, as these can be important issues in experimental measurements.

Chapter 3 describes the hardware that has been designed and built during the course of this work, including the software written to both control the operation of the experiments and process the measured data. The performance of the spectrograph, which is based around a holographically-produced concave diffraction grating and thermo-electrically cooled CCD detector, is described. Optical filtering arrangements for the semiconductor lasers used as excitation sources are described, along with the filtering optics at the input to the spectrograph. The electronic interface between the spectrographic hardware and PC is described, and the software that was written to control the hardware, and process and store the measured data is outlined. This software allows the elimination of instrumental and experimental artifacts (such as variable offsets in the detector signal, or background emission from the analyte under investigation), by the comparison of the spectrum from the analyte with that of a similar reference sample.

Chapter 4 contains the details of the mathematical model that was developed to describe parallel-optical-fibre probes and single-optical-fibre probes, and the comparison of this model to experimentally measured data. The optical fibres within the modelled probe need not be identical, and the model is shown to be accurate within experimental error for parallel-fibre probes in a wide range of configurations and environments. Several representative probe configurations are compared using the results of the mathematical model, to illustrate the effects of the relative diameters of the optical fibres within each probe. Practical constraints are applied to the total number of fibres within each probe, and it is shown that probes comprising few, large-cored, fibres are more efficient collectors of scattered light than those comprising many smaller cored fibres, where the number of fibres is limited by their total height when arranged as an array at a spectrometer input slit.

In chapter 5 several novel sample cells are described, and the interface between them and an optical-fibre probe is investigated. Mathematical models of the optical coupling efficiency of a probe to the cell, and the signal enhancement provided by the cell, are developed. Experimental measurements have been made, and these are compared with the model. Of the cell designs presented in this work, the designs based on the low-refractive-index polymer Teflon-AF, and based on a falling stream of analyte, are unique in spectroscopic applications.

The thesis is concluded in chapter 6, and some suggestions are offered for future work in the light of the experience gained during this project.

2. Principles of Optical Spectroscopy

The term ‘spectroscopy’ is applied to a vast range of experimental techniques in which one or more of the measurable properties of a system are resolved into a range of energies, wavelength, or other appropriate unit. Examples of the measured property of the system might be the energy of electrons emitted from a material’s surface, the time delay between light being absorbed and then re-emitted in the bulk of a sample, or the mass to charge ratio of ions. This work is concerned with optical spectroscopic techniques suitable for remote analysis of liquid analytes via optical-fibres.

In this chapter the techniques of optical absorption and emission spectroscopy, which are the most appropriate techniques to this goal, are described; the mechanisms of elastic scattering and Fresnel reflection are discussed for their relevance to cell design and as possible sources of optical interference; then the principles of Fourier transform and grating spectrometers, used to measure optical spectra, are described.

2.1. Absorption Measurements by Transmission

The most common form of optical spectroscopy is absorption (or transmission) spectroscopy, which is a measure of the amount of light absorbed by (or transmitted through) a sample over a range of optical frequencies. In order of increasing photon energy, the mechanisms for the absorption may be rotational or vibrational transitions of a molecule (in the microwave to IR), overtones of these (IR to visible), or electronic transitions in atoms or molecules (in the visible to UV region).

Whatever the physical basis of the absorption, the experimentally measured parameters are related via the Beer-Lambert law:

$$A = \log_{10}\left(\frac{I_0}{I}\right) = \varepsilon(\nu)cl \qquad \textbf{(2.1)}$$

According to the expression above, the absorbance A is proportional to the concentration of the analyte c and the path length through the sample l (quantitative information), and the molar absorption coefficient ε is a function of the optical frequency ν (qualitative information). I_0 is the intensity of a beam of collimated light before it enters the medium, and I is its intensity after it has travelled a length l. While A is parameter that is directly measured, in most theoretical treatments of underlying physics it is more convenient to work with the parameter α, which is expressed in equation 2.2.

$$\alpha = \frac{1n(10)}{l} \cdot A \tag{2.2}$$

The basis of most absorption measurements is implicit in equation 2.1; a collimated monochromatic beam of light is transmitted through an absorbing sample, and its intensity is referenced to that of a beam of light that did not pass through the sample. The instruments which make these measurements are called spectrophotometers, and sample holders are available to make measurements over a wide range of absorbance, such as very thin cells for highly absorbing liquids, or long path-length cells for measurements of gases or weakly absorbing liquids. Often the path of the light is folded through the cell, using mirrors or prisms, so that the beam of light makes multiple passes through a small cell.

2.1.1. Limitations of absorption measurements

Absorption spectroscopy as a means of quantitative spectroscopic identification may be limited by a number of factors[35]. At high concentration, the linear relationship of the Beer-Lambert law breaks down because solute-solute interactions become significant. This can usually be compensated for by calibrating the solution absorbance against reference solutions of known concentration.

Sampling problems are encountered for samples of very high absorbance if insufficient light is transmitted through the sample to make an accurate measurement. In such cases very thin transmission cells are used, or techniques such as *evanescent wave spectroscopy*, where light is removed from the evanescent field of light undergoing total internal reflection (hence the alternative name for the technique of *attenuated total-internal reflection*)[34].

In the visible and near infra-red region (the most convenient part of the spectrum for study over optical fibres) absorption is due to broad, and often weak, overtones of molecular vibrations. If these overlap with strong absorption bands of the solvent, then often no useful information can be deduced. Water is particularly bad as a solvent in this respect, with many broad overtones extending into the visible spectrum.

Conversely, if the solute absorbance is very low, the task of measuring very low concentration solutions is hampered by the problem of measuring a small differences in transmission between the solution, and the solvent by itself. Shot noise in the collected light will limit such measurements.

2.2. Emission Techniques

2.2.1. Fluorescent emission

The process of fluorescence in a compound involves the photon-induced excitation of electrons to higher energy levels (*ie* an absorption process), followed by their spontaneous return to a lower energy level, with consequential re-emission of a photon.

The re-emitted photon usually has a lower energy than the incident photon, as energy is often lost by phonon excitation processes (loss of energy to molecular vibrations).The lower energy emission band is called a Stokes band. A band with higher energy than the incident beam is called an anti-Stokes band.

Many aromatic compounds exhibit fluorescence when excited by UV light, but there are also some compounds and materials (*eg* certain organic dyes) having high fluorescence efficiency of optical re-emission when excited by less energetic photons (at other, longer wavelengths). The conversion efficiency is often expressed as a percentage, known as the quantum efficiency η, which is the percentage of the number of absorbed incident photons which result in re-emitted fluorescent photons.

$$\eta = \frac{\text{No. of fluorescent photons}}{\text{No. of absorbed photons}} \times 100\% \tag{2.3}$$

It is essential to effectively separate the desired fluorescent light from the scattered incident light. Fortunately, this problem is assisted by the difference in wavelength arising from the inelastic nature of the fluorescence process. Therefore it is only necessary to provide effective optical filters to remove the incident light from the detected fluorescence signal. If several fluorescent compounds are present, each having different fluorescent wavelengths, they may be detected independently using wavelength-selective bandpass filters or a grating spectrometer with a focal-plane detector array.

2.2.1.1. Time resolved fluorescence

This technique takes advantage of the statistical nature of the fluorescence processes. If a large number of molecules are excited by a short pulse of light to the same excited state, and then begin to fall back to their ground state, then

$$I = I_0 \exp(-t/\tau) \tag{2.4}$$

where the fluorescent light intensity I decays exponentially with the time t after optical excitation. I_0 is the peak intensity and τ the fluorescent lifetime.

In order to measure τ, two basic methods are used. The first (time-domain analysis) involves measuring the decay function, following short-pulse optical excitation, and computing the value of τ from this function. The second (frequency-domain analysis) uses a source with a sinusoidally-modulated incident light intensity. Either the frequency variation of the fluorescent light intensity as the modulation frequency is varied, or the phase delay between fluorescence and excitation signals (both of which are related to the value of τ) can be monitored. Because of the weak received signal, the frequency-domain methods usually use a coherent electronic detector based on a mixer circuit. This recovers the desired frequency component in the detected signals corresponding to the original sinusoidal modulation signal. If there are compounds in the analyte having distinctly different fluorescent lifetimes, they may be separated using either of the above time-resolved techniques. Also, the time-resolved techniques are complementary to any method of separation of signals in the wavelength domain.

A more typical fluorescent process consists of the excitation of an electron, its non-radiative decay to an intermediate level and subsequent radiative transition back to the ground state. In this case the non-radiative decay is also described by an exponential decay, with its own characteristic time constant. As long as the non-radiative time constant is much shorter than the radiative time constant (as it usually is) equation 2.4 remains valid.

2.2.1.2. Limitations of fluorescent spectroscopy

One of the primary problems of fluorescence spectroscopy is the non-linear variation with concentration at high levels of analyte, *ie* when absorption of the incident light becomes large. This causes a reduction in the fluorescent signal for two reasons. Firstly, it reduces the mean optical excitation level in the sample and secondly, at high absorption levels, causes all the absorption to take place close to the point of entry of light into the sample. (In the latter case, efficiency of light collection may be less, due to geometric effects of the measurement apparatus).

Other problems can occur, due to a strong dependence of the fluorescent signals on a variety of environmental parameters. Oxygen usually quenches (*ie* reduces) fluorescence. The pH of a solution, its temperature and any impurities can all influence the fluorescence lifetime and intensity. In addition, many fluorescent materials can become bleached during light absorption. This *photo-bleaching* might be reversible if it is merely due to a long fluorescent lifetime (saturation behaviour); if it is due to a non-reversible photo-chemical reaction it may gradually cause permanent depletion of the fluorophore. As expected, photo-bleaching is most serious at high illumination levels, but unfortunately intense sources are often required for trace analysis.

2.2.2. Raman scattering

In this section a brief description of the origin of the Raman effect in gases and liquids is presented, with the important predictions of semi-classical and quantum descriptions of the phenomenon of Raman scattering.

2.2.3. Review of the polarizability theory of Raman scattering

Predicted by Adolf Smekal in 1923 and first observed in 1928 by Sir Chandrasekhara Venkata Raman (who was at the time unaware of Smekal's prediction), the spontaneous Raman effect is the basis of an active branch of analytical spectroscopy. In a modern Raman experiment, laser light is shone into a sample and the wavelength spectrum of the scattered light is analysed. The molecular vibrational frequencies may then be deduced from the wavelength shifts acquired by the inelastically scattered light. Different molecules impart their own characteristic spectra of wavelength shifts, from which useful information on the molecules structure may be deduced. Quantitative information for compounds in solution may be derived from the intensity of the inelastically scattered light.

2.2.4. Stokes and anti-Stokes lines

The electric dipole moment (vector) $\underline{\mu}$ induced in a molecule by an externally applied electric field, $\underline{E}$, is

$$\underline{\mu} = \underline{\underline{\alpha}} \cdot \underline{E}. \qquad \textbf{(2.5)}$$

For light plane polarised along an arbitrary x, axis the electric field vector of the incident radiation is given by

$$\underline{E} = E_{0,\mathrm{x}} \cdot \sin(\omega t). \tag{2.6}$$

The molecular polarizablility $\underline{\underline{\alpha}}$ is a tensor quantity. The tensor matrix (equation 2.7) is symmetric about its major axis, and so contains only six independent elements.

$$\underline{\underline{\alpha}} = \begin{pmatrix} \alpha_{xx} & \alpha_{xy} & \alpha_{xz} \\ \alpha_{yx} & \alpha_{yy} & \alpha_{yz} \\ \alpha_{zx} & \alpha_{zy} & \alpha_{zz} \end{pmatrix} \tag{2.7}$$

If, for illustration, a hypothetical molecule with an isotropic polarizability is considered, only the elements on the major diagonal are non-zero. If the molecule is vibrating with an angular frequency ω_{vib}, and the polarizablility is a function of the separation of the nuclei, such that

$$\alpha_{\mathrm{xx}} = \alpha_{\mathrm{xx,eq}} + \alpha'_{\mathrm{xx,eq}} \cdot \sin(\omega_{\mathrm{vib}} t) \tag{2.8}$$

where the ‘eq’ subscript indicates the equilibrium value, and the prime indicates the first differential with respect to the deviation from equilibrium separation. Then plane polarized radiation incident on the molecule induces an electric dipole $\underline{\mu}$, which from equation 2.12 written in component form is

$$\begin{gathered} \mu_x = (\alpha_{\mathrm{xx,eq}} + \alpha'_{\mathrm{xx,eq}} \cdot \sin(\omega_{\mathrm{vib}} t)) E_{\mathrm{x}} \cdot \sin(\omega t) \\ \mu_x = \alpha_{\mathrm{xx,eq}} E_{\mathrm{x}} \cdot \sin(\omega t) + \frac{1}{2} \alpha'_{\mathrm{xx,eq}} E_{\mathrm{x}} \left(\cos((\omega - \omega_{\mathrm{vib}}) t) - \cos((\omega + \omega_{\mathrm{vib}}) t) \right) \end{gathered} \tag{2.9}$$

The intensity of radiation emitted from such a dipole is proportional to the change in electric field (dipole moment) squared, and the oscillation of the electric dipole moment contains components (side-bands) with angular frequencies ω-ω_{vib} and ω+ω_{vib}. Quantum mechanics shows that these frequencies may take only discrete values, determined by the mass of the atoms in the molecule and the nature of the chemical bonds between the atoms. The bands of lower frequency scattered light are referred to as *Stokes lines*, and the bands at a higher frequency (and hence higher energy) than the exciting light are termed *anti-Stokes lines*[35].

Also apparent from equation 2.9 is that the intensity of radiated Raman light is determined by the square of the differential polarizability α'_{eq}, and will not be observed at all if the vibration does not induce a change in the polarizability. Often physical intuition is sufficient to predict which vibrations of a simple molecule are likely to be Raman active. More rigorously these can be determined by group theory[35]. Equation 2.9 does not describe the relative intensities of the Stokes and anti-Stokes bands, which is quantum mechanical in origin (section 2.2.8).

2.2.5. Wavenumber (spectroscopist's) units, cm^{-1}

Whereas the wavelength of light, λ, is the natural parameter to use when describing the optics of a system, it is the energy difference, E_{tr}, between the incident light and the collected light that is of direct relevance in spectroscopy. This energy difference is normally quoted either as the difference in frequency between the incident and scattered photons (*ie* E_{tr}/h, where h is Plank's constant), or as a wavenumber[35] (E_{tr}/hc, where c is the speed of light). In Raman spectroscopy the traditionally accepted units of wavenumber are cm^{-1}. Molecular vibrational frequencies are also traditionally quoted in cm^{-1}, and to convert a frequency ν in Hertz to a frequency in wavenumbers $\bar{\nu}$; $\bar{\nu} = \nu/c$, where c is the speed of light.

It should also be noted that, because λ and σ are not linearly related, when rescaling a plot of intensity *vs* wavelength to one of intensity *vs* frequency shift (or *vice versa*), a correction should be applied to the intensity across the graph, so that the integrated area (which represents energy) under each peak remains constant. Analogous to changing the variable in an integration[36], to accurately represent a measurement in constant divisions of the variable u on a graph against the variable v multiply the measured values of u by du/dv. (Another example of this is the Plank radiation curve, which is often plotted against frequency and wavelength[37]).

2.2.6. Frequency dependence of scattered light intensity

Any light (below the frequency of the electronic resonances) may be used to excite a Raman spectrum. The scattered radiation is essentially that of an oscillating electric dipole[38], the dipole-moment of which is given by equation 2.9. The intensity I of radiation at a frequency ν emitted from such a dipole can be shown to obey

$$I \propto \nu^4. \qquad \textbf{(2.10)}$$

2.2.7. Depolarization ratio, ρ_p

In a liquid, molecules are orientated at random to one-another, and the scattering from such a sample corresponds to the average over all molecular orientations. The results are expressible in terms of two quantities associated with the tensor $\underline{\underline{\alpha}}$ (equation 2.7), the mean value $\bar{\alpha}$ and the anisotropy γ.

$$\bar{\alpha} = \frac{1}{3}(\alpha_{xx} + \alpha_{yy} + \alpha_{zz})$$
$$\gamma^2 = \frac{1}{2}\left((\alpha_{xx} - \alpha_{yy})^2 + (\alpha_{yy} - \alpha_{zz})^2 + (\alpha_{zz} - \alpha_{xx})^2 + 6(\alpha_{xy}{}^2 + \alpha_{yz}{}^2 + \alpha_{zx}{}^2)\right) \quad \textbf{(2.11)}$$

For the case where the polarizability is not isotropic, γ is non-zero, and linearly polarized radiation is *depolarised* to some extent after scattering. The depolarization ratio[39] (for polarized incident light) ρ_p may be derived from $\bar{\alpha}$ and γ,

$$\rho_p = \frac{I_x}{I_z} = \frac{3\gamma^2}{45\bar{\alpha}^2 + 4\gamma^2}. \quad \textbf{(2.12)}$$

In equation 2.12 I_y and I_z are the measured intensities of light polarized parallel to the *x* and *z* axes respectively, measured at 90° to the direction of the incident light, which is polarized parallel to the *z* axis.

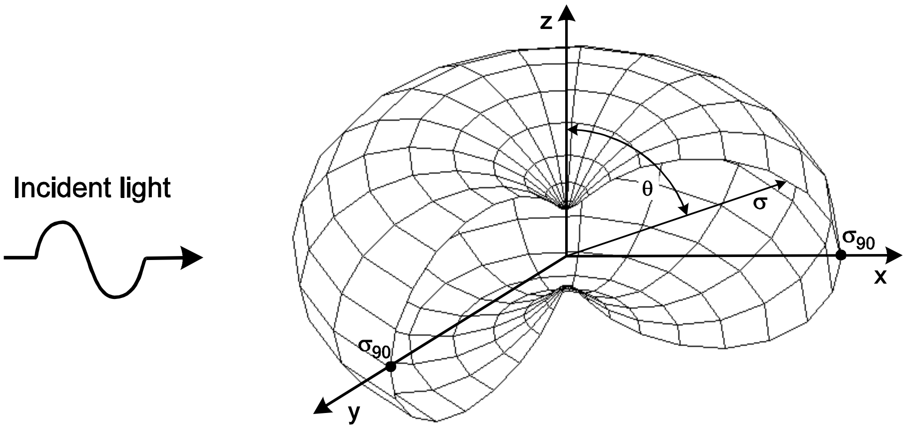

Figure 2.1 A section from a diagram showing the relative intensity of scattered radiation vs scattering angle, in a liquid of depolarization ratio, $\rho_p = 0.17$.

The surface in figure 2.1 shows the intensity distribution of Raman scattered light in water. It is calculated from equation 2.13 (modified from Marshall[40] to take into account all polarisations of scattered light and standard spherical coordinates)

$$\sigma = \sigma_{90} \cdot \left((1 - \rho_p)\sin^2(\theta) + \rho_p\right) \quad \textbf{(2.13)}$$

where σ represents the differential scattering cross section integrated over all molecular orientations and σ_{90} is the light scattered at 90° by one molecule.

The units of σ are sr^{-1} (reciprocal steradians).

2.2.8. Review of the quantum theory of spontaneous Raman scattering

While the classical polarizability theory of section 2.2.3 does account for the inelastically scattered Raman spectra of molecules, it can not explain even qualitatively why the spectra are manifest as a series of discrete bands. This is the realm of quantum mechanics[41], and some relevant results are presented here with the selection rules which determine which vibrational transitions are allowed, and hence are observed in a Raman spectrum.

2.2.9. The molecular potential well and its allowed states

The qualitative form of the potential well between two nuclei, for instance in a diatomic molecule, is shown in figure 2.2[35]. The exact form of this curve is generally not known, but as can be seen from the figure, the textbook problem of the parabolic potential is a reasonable approximation for the lower energy part of the curve.

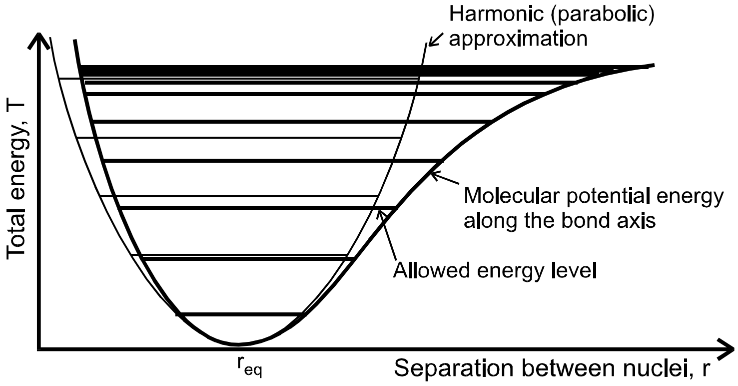

Figure 2.2 The general form of the internuclear potential along a bond axis, and a parabolic well as assumed in the harmonic approximation, and the quantum mechanically allowed energies.

The properties of systems governed by a parabolic potential are well covered in any undergraduate physics compendium[42]. Classically, a harmonic oscillator will vibrate at the same frequency regardless of how much energy is stored in its vibrational motion. The quantum mechanical analogue of this behaviour is that the allowed energy levels that the system may occupy are equally spaced in energy as shown in figure 2.2. The allowed energy levels E_V that a harmonic oscillator may take are

$$E_V = h\nu(1/2 + V) \qquad V = \pm 0, 1, 2, \ldots \tag{2.14}$$

where V is the vibrational quantum number and ν is the (classical) frequency of vibration.

Typical molecular vibrational frequencies studied in a Raman experiment are between 1.5×10^{13} Hz and 1.35×10^{14} Hz, corresponding to energy levels spaced, in the harmonic approximation, by 1×10^{-20} J to 9×10^{-20} J. Transitions between these levels correspond to the energy (and frequency) of IR photons and this is the basis of IR absorption spectroscopy, where photons of energy corresponding to the difference between the energy levels may be absorbed. The interaction between molecule and photon is different for Raman scattering: in this case the photon is not absorbed, but forms a short lived (~10^{-13} sec) virtual state with the molecule. Effectively the entire ladder of allowed energy states is raised by the energy of the photon. When a virtual state decays, the molecule does not necessarily return to its original energy state (figure 2.3).

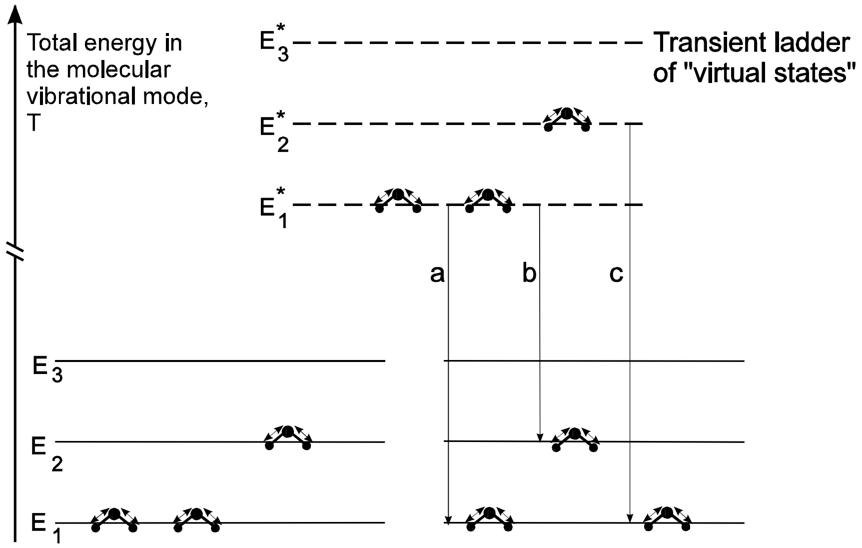

Figure 2.3 Three molecules and their vibrational states throughout a scattering process (a) ΔV=0, Rayleigh scattering (b) Stokes scattering, ΔV=1 (c) Anti-Stokes scattering, ΔV=-1.

The population of the Energy levels E_1, E_2, etc, are governed by a Bose-Einstein distribution[43], and at room temperature the population of levels above the ground state decreases rapidly, which accounts for the much weaker intensity of the anti-Stokes bands in a Raman spectrum.

2.2.10. Quantum mechanical selection rules

The probability of transition $\underline{\underline{R}}_V$[35] between two eigenstates of a vibrating molecule is given by

$$\underline{\underline{R}}_V = E_x \int \psi_{V'}^* \underline{\underline{\alpha}} \psi_{V''} \, dx \tag{2.15}$$

where x is the internuclear displacement from equilibrium. If $\underline{\underline{\alpha}}$ is expanded to a Taylor series, equation 2.15 can be rewritten as

$$\underline{\underline{R}}_v = \underline{\underline{\alpha}}_{eq} \int \psi_{V'}^* \psi_{V''} \, dx + \left.\frac{d\underline{\underline{\alpha}}}{dx}\right|_{eq} \int \psi_{V'}^* \, x \, \psi_{V''} \, dx + \frac{1}{2!} \left.\frac{d^2\underline{\underline{\alpha}}}{dx^2}\right|_{eq} \int \psi_{V'}^* \, x^2 \, \psi_{V''} \, dx + \cdots \tag{2.16}$$

where $\underline{\underline{\alpha}}_{eq}$ and the subsequent derivatives are the values at mechanical equilibrium. Because $\psi_{V'}$ and $\psi_{V''}$ are eigenfunctions of the same Hamiltonian, the first integral in equation 2.16 must be zero, unless $V' = V''$ which corresponds to elastic (Rayleigh) scattering of the photon. The integral of the second term can be shown to be finite only when $V' - V'' = \pm 1$ (for the parabolic potential well approximation), which may be written as in equation 2.17.

$$\Delta V = \pm 1 \tag{2.17}$$

The higher terms in equation 2.16 decrease rapidly due to the factorial prefactor.

Raman scattering intensity is proportional to $(\underline{\underline{R}}_V)^2$, and so again, the intensity of the inelastically scattered Raman light is proportional to the first differential of the polarizability squared (as in section 2.2.4).

2.2.11. Anharmonic effects

Two types of anharmonicity may be apparent in a vibrational spectroscopy measurement: *mechanical anharmonicity* is anharmonicity in the inter-nuclear potential (*ie* a deviation from the parabola of figure 2.2); *electrical anharmonicity*, arises from the differential polarizability $\underline{\underline{\alpha}}'$ being a function of position (other than a constant). The result of both these deviations from the theory presented above is a relaxation of the vibrational selection rule of equation 2.17 (*ie* the third, and subsequent, terms in equation 2.16 become significant), allowing transitions between any two vibrational levels, so called *overtones*.

The deviation of the molecular potential well from the parabolic approximation becomes more pronounced as the amplitude of a vibration moves the constituent atoms further from their equilibrium positions (figure 2.2). This results in the decrease in the energy level spacing, towards a continuum, so that transitions that are allowed by equation 2.17, but starting from different energy levels, will release different energies (while the parabolic approximation predicts that any transition between adjacent energy levels is equivalent). At the temperatures of concern in this work, only the lower vibrational energy levels are occupied.

In this work the probability of transitions due to anharmonic effects is low, and has been ignored.

2.2.12. Rules of thumb in Raman spectroscopy

Only those vibrations which result in a change in the polarizability of the molecule will scatter light inelastically, and are said to be Raman active. Diatomic molecules always have Raman active vibrations, and in general if a vibration preserves all of the symmetry elements of a molecule then the vibration will be Raman active.

Vibrations which result in particularly large changes in polarizability produce more intense Raman signals. These are often vibrations of atoms bonded by π-bonds, or large resonance bonds (*eg* benzene). Stronger Raman bands are normally expected from bonds between elements in the second and subsequent rows of the periodic table (as they have more electrons), cyclical molecules (such as benzene) and hydrogenic molecules (those containing hydrogen).

Liquids with large intermolecular interactions (such as those due to hydrogen bonding, in the case of water) will have broad bands, as the frequency at which a molecule vibrates will be affected by the particular orientation of the molecule with respect to its neighbours.

The intensity of the scattered radiation is proportional to the fourth power of the incident photon frequency, and has a spatial distribution as shown in figure 2.1. Typically a proportion of order 10^{-2} of the incident photons will be scattered elastically, and a fraction of only 10^{-4} of this shifted in wavelength. As higher frequency radiation is used to increase Rayleigh and Raman scattering a compromise arises for the best wavelength for Raman analysis, eventually the photon energies will correspond to electronic transitions within the sample. A sufficiently high energy photon may be absorbed by the molecule (rather than scattered) and then re-emitted as fluorescence (after a characteristic fluorescence lifetime much greater than the 10^{-13} seconds of a scattering event). Fluorescence bands are spectrally-broad and typically four to six orders of magnitude stronger than the weak Raman lines[44]. Fluorescence is not normally a problem with infrared excitation, but becomes significant with radiation in the visible to ultra-violet region. Except for rare two photon absorption events, fluorescence is usually of a lower energy than the radiation which excites it, and so is seldom a problem in the study of the even weaker anti-Stokes bands.

2.2.13. Absolute intensity measurements

Making absolute determinations of the amount of light scattered into the optics of a spectrometer or interferometer is difficult. The small intensity of the Raman scattered light, and the precautions taken to reject any inelastically scattered light, both necessitate careful calibration with a reference radiance standard. In practice, if the absolute value of the scattered radiance must be found, the intensity of the spectrum is compared with that of a secondary standard[45][46][47].

Absolute Raman scattering cross sections found in this way are tabulated for some gases and organic liquids in Weber[45]. More recent measurements of liquids (organic and halide ion solutions) have been made by Eysel[46][48] and the scattering cross section of water is measured and discused by Marshall[40]. Fischer[49] and co workers have demonstrated for aqueous solutions at concentrations below 1 M, the background Raman spectrum due to the water is unchanged in shape, although its intensity may decrease slightly.

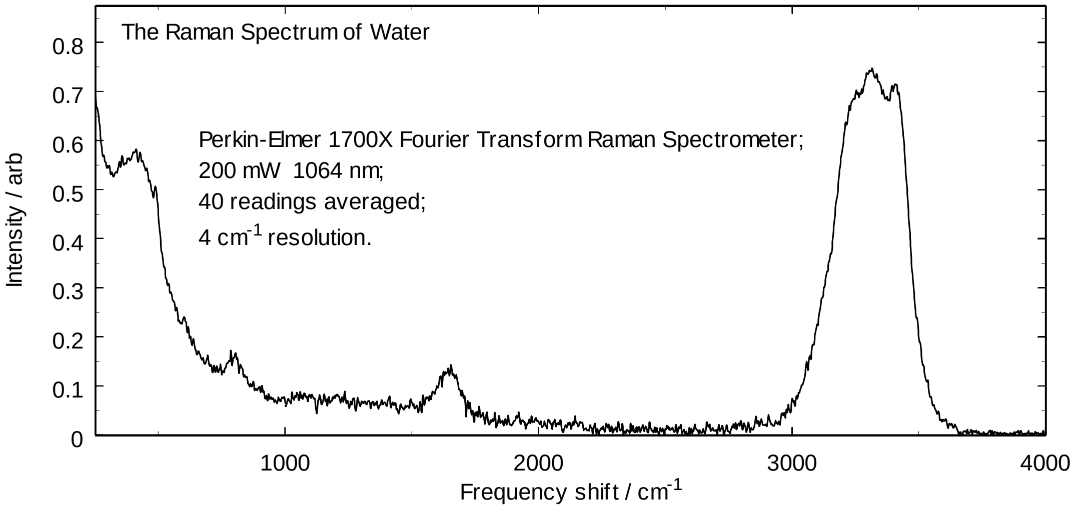

Figure 2.4 Experimentally measured Raman spectum of water, recorded using a commercial Fourier transform interferometer, with 1064 nm incident light from a Nd-YAG laser.

It can be seen that the bands of (hydrogen-bonded) water (figure 2.4) are much broader than those of the two non-polar solvents (figure 2.5); the rise in Raman scattering intensity towards the laser line is due to hydrogen bonding. The rising baseline in figure 2.5 is an artifact of the (dispersive) spectrometer optics, and is believed to be due to fluorescence of the optical components. The frequency shifts in figures 2.4 and 2.5 are towards lower frequencies, *ie* Stokes bands are plotted.

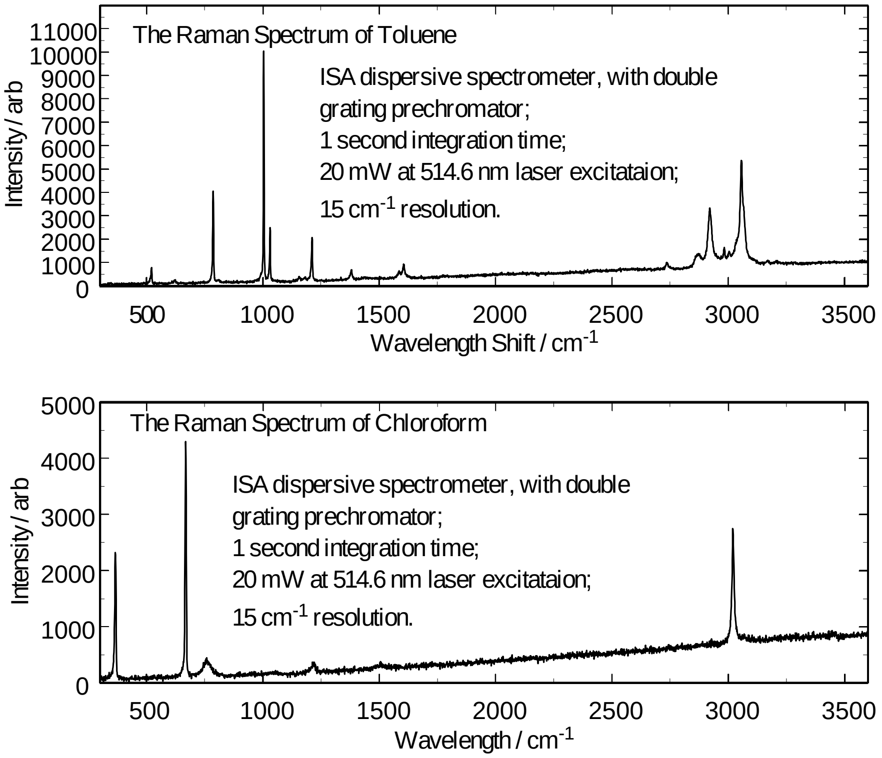

Figure 2.5 The Raman spectra of chloroform and toluene recorded using a commercial dispersive spectrometer equipped with a CCD camera and double grating prechromator.

In comparing the spectra above, although the intensity scale of the FT device cannot be directly related to that of the dispersive spectrometer, it may be noted that the scattering cross section (integrated over its width) of the 1002 cm^{-1} line of toluene is only 30% greater than that of the 3400 cm^{-1} line of water[45][40], although the peak scattering cross section of the toluene line is over an order of magnitude greater.

2.2.14. The resonance Raman effect

A related phenomenon is that of *resonance Raman scattering*[39]. If progressively higher photon energies are incident on a sample, eventually the ν^4 dependance of equation 2.5 breaks down. This happens as the energy of the incident photons approaches that of the molecular electronic levels. The Raman scattering cross section may increase by 10^6 as the electronic energy level is approached, for instance, Hofmann and Moser[50] measured an intensity increase by a factor of 850 in the 813 cm^{-1} line of KNO_2 as the incident wavelength was changed from 436 nm to 254 nm. At even shorter wavelengths Barletta and Veligdan[51] found the scattering cross section of CCl_4 to increase by 1.6×10^4 with 248 nm incident light.

Although the Raman scattering cross section can rise dramatically at resonance, the scattered radiation may be concealed by a simultaneous increase in absorption, or by fluorescence emission. The effect is not beneficial to this work. By choosing a sufficiently short incident wavelength for resonant Raman scattering from a particular molecule, it is more likely that problems from fluorescence of other compounds in our analyte will be encountered. For instance, the electronic absorption spectra of toluene[52] and chloroform[53] are in the ultraviolet, and any attempt to produce Raman spectra from these in a cross-contaminated analyte will certainly suffer from fluorescence masking.

2.2.15. Surface enhanced Raman scattering (SERS)

Between 1974[54] and 1977[55] experiments studying the Raman scattering intensity of molecules adsorbed on to the surface of metal electrodes showed that the Raman scattering intensity of the adsorbed molecule could be increased by as much as 10^6 times. While, because of the problems associated with surface fouling, this surface enhancement effect has not been used in this work, it is described briefly here for completeness, and as a potential extension to what has been done. Garrell[56] has written an introduction to the subject, including analytical applications, and Chang and Furtak[57] edited a convenient introduction to the theory.

The models used to describe the origin of SERS may be broadly divided between molecular and electromagnetic descriptions. Molecular theories contend that the polarizability $\underline{\underline{\alpha}}$ is enhanced, that molecules adsorbed on to a metal surface may be orientated preferentially with respect to the incident electric field and that the electronic structure of the molecule may be altered such that the incident light approaches the energy of a modified molecular resonance. Electromagnetic explanations invoke image fields in the metal substrate, electric field vector enhancements due to the shape of the substrate (‘lightening rod’ effects), surface plasmons, and charge transfer between the substrate and molecule. In general, both molecular and electromagnetic enhancement mechanisms both play a part in the enhancement effect, although the relative importance of the molecular and electromagnetic models varies widely from case to case.

The experimental results are remarkable, both in the magnitude of the observed enhancement, and the wide range of analytes amenable to the technique. Silver, copper, and gold are the most commonly used substrates[57], the most universal substrate being silver. Pyridine adsorbed on to silver substrates displays an enhancement of up to 10^6, approximately constant between 700 nm and 500 nm[57][58]. The enhancement varies for different adsorbates, and for each vibrational band of a molecule, and is a function of the incident wavelength. Silver substrates display a maximum enhancement between 500 nm and 700 nm, whereas copper and gold substrates are most efficient in the near infrared (NIR)[57].

In the laboratory, many environmentally important classes of molecule have been studied with SERS. For instance, Alak[59] has demonstrated detection of 10^{-6} M concentrations of chlorinated pesticides in aqueous solution in a 4 second integration time. Storey *et al*[60] have measured chlorinated hydrocarbons *in situ* at 10 ppm in ground water, and low ppm sensitivities for benzene and napthalene in ground water have been reported by Carron *et al*[61]. However, despite its attraction for low level measurement, the use of SERS for *in situ* analysis is effectively not a direct spectroscopy as described at the beginning of this chapter, due to the involvement of the surface layer. It requires a carefully prepared probe, which is, by the nature of the technique, susceptible to fouling.

2.3. Elastic Light Scattering

Fluorescent emission and Raman scattering can both be described as *inelastic* processes: the energy of the scattered photons is not conserved. The light has a different frequency (and hence a different wavelength) after the interaction, and it is this change which enables us to deduce the presence of an analyte. However, light is more commonly scattered without any change in energy: the frequency of the photons is unchanged, and the process is termed *elastic*. Elastic light scattering can been used to measure the size, density, and shape of scattering particles[62], but in this work it can be the major source of noise in the measurement of the inelastically scattered light; to avoid inelastically scattered light, one needs to know where it is coming from, and where it is going to.

2.3.1. Rayleigh scattering

When light is scattered by particles that are sufficiently well spaced that the scattering from each is incoherent, and small enough that the scattered light may be considered to originate from a single point, then the scattering may be described by the theory of Rayleigh scattering. As in Raman scattering from molecules, the scattering centres behave individually as electric dipoles, and the scattering pattern has the text book dipole distribution and $1/\lambda^4$ variation of intensity[38]. Because the scattering from each centre is unrelated to that from the next, the net irradiance at any point is simply the sum of the irradiances of each scattering centre. All matter will scatter light by this mechanism.

2.3.2. Mie scattering

The Mie scattering theory includes the size, shape, refractive index, and absorptivity of the scatterers, and reduces to Rayleigh scattering as a special case[38]. It should be used where the size of the scattering centres is larger than $\lambda/10$, *ie* when the scattering within each particle becomes the sum of the scattering from *coherently* radiating dipoles. As the size of the scattering centres increases with respect to the wavelength of the scattered light, the scattering becomes concentrated in the forward and reverse directions, and the scattering intensity becomes independent of the scattering wavelength (*ie* white light scattering). Particles of dust, water droplets, net curtains, and materials with gross random variations of refractive index will scatter light by this mechanism. For particles much larger than the wavelength of the scattered light, the macroscopic laws of refraction and Fresnel reflection apply, resulting in mainly forward scattering.

2.3.3. Fresnel reflections

Fresnel reflection is the term given to the partial reflection of light incident on a boundary between materials with different refractive indices. Fresnel reflection is a consequence of the same electromagnetic equations and boundary conditions as Mie scattering, but applied to macroscopic situations[63]. The reflectance and transmittance coefficients R and T are given for non-magnetic media by equations 2.18 and 2.19. The subscripts $\perp$ and $\parallel$ refer to the cases that the electric field vector is perpendicular or parallel to the *plane of incidence*[1] respectively, i and t are the angles of incidence and transmission with respect to the surface normal, n_i and n_t are the refractive indices of the incident and transmitting media.

$$\begin{aligned} R_\perp &= \left(\frac{n_\mathrm{i}\cos(i) - n_\mathrm{t}\cos(t)}{n_\mathrm{i}\cos(i) + n_\mathrm{t}\cos(t)} \right)^2 \\ T_\perp &= \left(\frac{2\,n_\mathrm{i}\cos(i)}{n_\mathrm{i}\cos(i) + n_\mathrm{t}\cos(t)} \right)^2 \end{aligned} \tag{2.18}$$

---

[1] The plane of incidence is the plane in which the incident, reflected, and transmitted rays all lie.

$$R_{\parallel} = \left(\frac{n_{\mathrm{i}}\cos(t) - n_{\mathrm{t}}\cos(i)}{n_{\mathrm{i}}\cos(t) + n_{\mathrm{t}}\cos(i)} \right)^2$$

$$T_{\parallel} = \left(\frac{2n_{\mathrm{i}}\cos(i)}{n_{\mathrm{i}}\cos(t) + n_{\mathrm{t}}\cos(i)} \right)^2 \qquad \textbf{(2.19)}$$

The angle of incidence *i* is related to the angle of transmission *t* by Snell's law, equation 2.20.

$$n_{\mathrm{i}}\sin(i) = n_{\mathrm{t}}\sin(t) \qquad \textbf{(2.20)}$$

Equations 2.18 and 2.19 do not apply to films with thicknesses comparable to the coherence length of the light propagating through them; optical interference will modify the reflectance and transmittance at such an interface, *ie* in the case of anti-reflection coatings[64].

2.4. Making Optical Spectroscopic Measurements

The techniques which may be used to resolve different wavelengths of light from one another, and quantify the energy in each measured spectral band, are briefly described here with their relative merits. Light intensity measurements are described in section 2.5.

2.4.1. Fourier transform spectrometers

This is not so much a spectroscopic arrangement, rather a generic means of processing the optical signals without a traditional monochromator to analyse the light spectrum. The method involves detection of the optical signal, via an interferometer having a scanned path-length difference. A two-path interferometer acts as an optical filter, having a periodic transmission $T(\nu)$, with a function of optical frequency ν where

$$T(\nu) \;=\; 1 + \sin\bigl(k(\nu)\bigr) \qquad \textbf{(2.21)}$$

The constant, *k*, depends on the optical path differences in the interferometer. When a complex light spectrum $I(\nu)$ is passed through an interferometer onto a detector with a spectral response $D(\nu)$. then the detected signal is $S(\nu)$. $S(\nu)$ is given by

$$S(\nu) = \int_{\nu=\nu_{\max}}^{\nu=\nu_{\min}} I(\nu)\cdot T(\nu)\cdot D(\nu)\cdot \mathrm{d}\nu \qquad \textbf{(2.22)}$$

The function *S* represents the correlation between the sinusoidal transmission function of the interferometer and the combined spectral responses of the input light spectrum and the spectral response of the detector. Clearly, the correlation is best with spectral variations having the same (optical-frequency) periodicity as the interferometer. In the simplest case, where $I(\nu)$ is a narrow line spectrum of constant frequency, the signal S represents a single (sample) point on the sinusoidal response. If the path-length of the interferometer is now scanned, its periodic transmission-response function will translate across the frequency band (and also change its period versus frequency). The detected signal will therefore vary, as the correlation between the spectral features and the periodic interferometer response varies. In the simplest case of the line spectrum, the detected signal will vary sinusoidally as the interferometer is swept. More complex spectra can be considered to consist of a linear addition of a series of such narrow-line spectra, each having an appropriate amplitude. For a complex spectral response, the variation of the detected signal with time, as the interferometer is swept, represents the inverse Fourier transform of the original spectrum. The spectrum can therefore be recovered by Fourier transformation of the temporal variations in detected signal, resulting when the interferometer is scanned. This is again illustrated by the simple example of the line spectrum, which results in a sinusoidal temporal response. The Fourier transform of a sinusoidal signal has a single value, corresponding to the single frequency of the line spectrum.

When compared to conventional spectrometers, the Fourier transform system has several advantages. The first is that it is relatively easy to obtain high spectral resolution by using a long ‘path’ difference interferometer (10 cm path difference at 1 µm wavelength, results in a fractional resolution of around 1 part in 10,000). The second is that a significant fraction of the source light is incident on the detector at all times, because the mean transmission of the interferometer is much higher than that of a narrow band grating monochromator, thereby improving the optical efficiency. The third is that the interferometer can be designed with a large optical aperture, giving much higher optical throughput from radiance-limited optical sources. The advantages are less significant when only moderate resolution is needed and low-noise (*eg* CCD) detector arrays can be used, as these also allow parallel detection of each spectral component.

The main disadvantage is normally the need for a precisely-aligned interferometer, with its necessary thermal and mechanical stability. Fourier Transform spectroscopy is applicable to a wide variety of spectroscopic techniques, including transmission, reflectance, fluorescence and Raman spectroscopy, as, in all of these cases, it can be used for spectral analysis before the detection system.

2.4.2. Dispersive (grating) spectrometers

For use in this project a spectrograph based around a holographically ruled concave diffraction grating from Jobin-Yvon/ISA (section 3.2) has been designed and built. The main results relevant to its operation are presented here. For more information the reader should consult one of the many text books dealing with diffraction grating physics, such as the one written by Thorne[7].

2.4.3. Diffraction grating equations

Referring to figure 2.6, the equation relating the angle of incidence *i* and reflection (diffraction) *r* for collimated light of wavelength λ on to a planar diffraction grating ruled with a pitch (line spacing) *d* is

$$m\lambda = d\left(\sin(i) + \sin(r)\right). \tag{2.23}$$

Here *m* is a positive or negative integer (including zero), and is referred to as the *order* of the diffracted beam. The zeroth order, *m*=0, represents specular reflection, *i*=-*r*. If an order is on the opposite side of the zeroth order to the incident beam then m is negative, illustrated in figure 2.6(a). The angles *i* and *r* are both measured in the same direction, with respect to the normal of the grating.

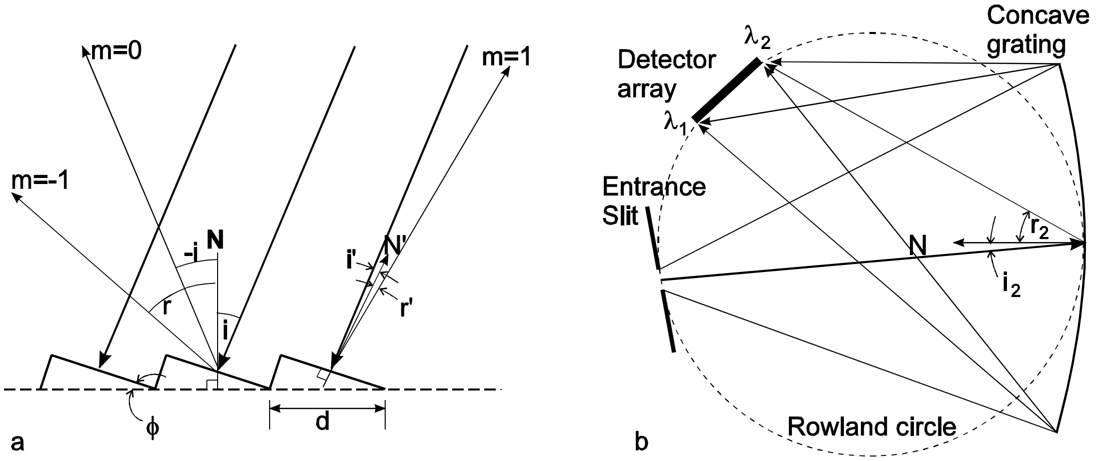

Figure 2.6 (a) A ray diagram of light incident on to a blazed diffraction grating. (b) Using a concave grating eliminates the need for focusing optics.

The input of a spectrometer is usually a slit, and the light from this slit is collimated by lenses or mirrors in the spectrometer. These focusing optics can be eliminated through the use of a concave grating. The angle of diffraction is calculated as before, the angles *i* and *r* being measured between rays incident on to the centre of the grating and the normal to it. The configuration illustrated in figure 2.6(b) is that of Rowland[7], who showed that a concave grating can act as its own collimator. The entrance slit is on the *Rowland circle*, a circle with a diameter equal to the radius of curvature of the diffraction grating, and for small apertures the diffracted rays are also focused on to the Rowland circle. The particular benefit of this configuration is that the first type coma[38] of the image of the entrance slit is zero. By careful control of the groove spacing[65] other optical aberrations can be corrected too.

Evidently, from equation 2.23, light of wavelength λ can be diffracted at several angles (r), corresponding to the different orders (m). This is wasteful, and may contribute to the stray light within a spectrometer. In fact light can be directed preferentially into orders at a particular angle by blazing the diffraction grating, as illustrated for the $m=1$ case in figure 2.6(b). In this case, the incident and refracted light are both almost along the groove normal, an arrangement known as the Littrow configuration[7][65]. In general, the diffracted light will be concentrated into any order in which light is specularly reflected from the groove surfaces; *ie* $i'=-r'$.

For a spectrograph, the *angular dispersion* of the grating can be found by differentiating equation 2.23, where i is a constant, to give

$$\frac{\mathrm{d}r}{\mathrm{d}\lambda} = \frac{m}{d\cos(r)}. \qquad \textbf{(2.24)}$$

For a grating with focal length f the *linear dispersion* is defined as

$$\frac{\mathrm{d}\lambda}{\mathrm{d}x} = \frac{f}{dr/d\lambda} \qquad \textbf{(2.25)}$$

where dx is an incremental distance across the focal plane of the detector. From the linear dispersion the wavelength incident on each part of the detector array, and the resolution of the spectrometer, may be found (assuming that diffraction at the input slit is negligible).

When perfectly monochromatic light is incident in to a spectrometer through, for instance, a slit, an image of the entrance slit is formed at the detector. The minimum dimension of the image is diffraction limited by the size of the dispersing element, assuming that the whole of the element is illuminated. For a circular diffraction grating, of diameter D, the diameter of the central portion of the diffracted image a, can be found by considering the grating as a circular aperture[38], so

$$a = 1.22\frac{2f\lambda}{D} \qquad \textbf{(2.26)}$$

where f is the focal length of the spectrometer and λ is the wavelength of the diffracted light. If the image of the slit is larger than a, then the resolution of the spectrometer is simply determined by the geometrical image of the entrance slit and the linear dispersion of spectrometer (assuming that the detector width is less than that of the image). For the 70 mm diameter grating used in this project the diffraction limited image size is 5.5 µm and so the system resolution is determined by our entrance aperture, defined by fibre ends of diameter 400 µm.

2.4.4. Stray light and ghost lines

An effect which may further limit the performance of a spectrometer, especially if low intensity bands must be resolved from much higher intensity ones, is *stray light*[65]. The term encompasses all spurious light incident on to the detector, other than that at the wavelength of interest, and can be broadly divided between *randomly scattered light* and *focused stray light*. Randomly scattered light may be a result of dust or imperfections in the optical surfaces or reflections within the spectrometer housing of optically misaligned light, or light in those orders of diffraction not directed towards the output. Focused stray light arises from optical aberrations of the focusing optics in the spectrometer and re-entrant spectra.

Obviously optical misalignment can be avoided, and this includes matching the numerical aperture of the input light to that of the focusing optics of the spectrometer. The effect of other reflections can be reduced by *baffling* the spectrometer, which essentially entails erecting partitions within the spectrometer wherever possible, between potential sources of stray light, and the optical detector. Minimising or correcting for the effects of optical aberrations is a trade off between optical perfection and size and simplicity, but one should also be aware that even the best optical components are not perfectly polished, and the more optical surfaces are introduced in to the system, the greater the potential scattering from surfaces.

A related phenomenon in diffraction grating spectroscopy is that of ghosting, where periodic errors in the ruling of the grooves result in spurious maxima in the diffracted spectrum. This is a problem in 'traditionally' produced gratings, which are fabricated by mechanically ruling a diamond point back and forth across the surface of a polished blank. Any periodic variations in the groove spacing d (figure 2.6, equation 2.23) will result in ghost lines focused on to the detector.

Ghost lines are eliminated by the use of holographically produced gratings, which have no periodic ruling errors. The stray light performance of a holographically ruled diffraction gratings is typically a factor of ten better than that of a mechanically ruled grating[65], and in addition, the ruling pattern can be optimised to correct for certain geometric aberrations as well. Even a perfect diffraction grating will randomly scatter light though, as it is impossible to perfectly polish a surface. However, by making use of concave diffraction gratings which both collimate the incident light, and refocus diffracted light on to the detector, all other scattering surfaces can be eliminated from an optical system.

2.4.5. Grating f-number and spectrograph numerical aperture

The light collecting properties of the input aperture of a spectrometer are either quoted as an f-number (*f/#*) or a numerical aperture (*NA*) (figure 2.7). The two are related by equation 2.27.

$$NA = \frac{1}{2(f/\#)}. \tag{2.27}$$

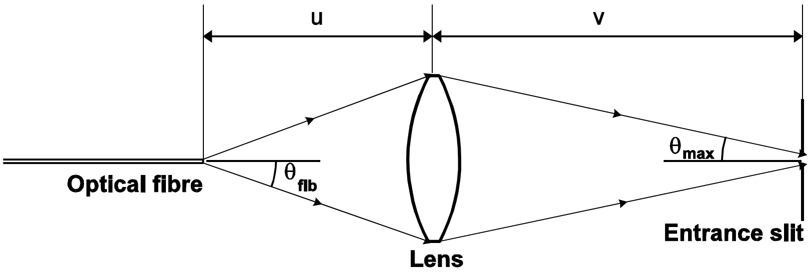

Figure 2.7 Matching the numerical aperture of a fibre to a spectrograph.

An optical fibre is also characterised by its numerical aperture, and if the numerical aperture of the fibre is greater than that of the spectrometer then the source *NA* must be *matched* to the acceptance *NA* of the spectrometer. This can be achieved with a lens of focal length *f* as shown in figure 2.7, where *u* and *v* are related to *f* by

$$\begin{aligned} u &= f\left(1+\frac{\tan(\theta_{fib})}{\tan(\theta_{max})}\right) \\ v &= f\left(1+\frac{\tan(\theta_{max})}{\tan(\theta_{fib})}\right) \end{aligned} \tag{2.28}$$

Such matching results in a magnification of the fibre tip at the entrance slit, given (for paraxial rays) by

$$M_a = \frac{\theta_{fib}}{\theta_{max}} \tag{2.29}$$

2.5. Detector Technologies

The optical intensities across the output plane of the spectrograph must be converted into electronic signals to be measured. The wavelengths of light used in this work (approximately 700 nm to 900 nm) fall conveniently within the sensitive range of silicon devices[66]. Several detector configurations were investigated during the course of this work, including arrangements using discrete photodiodes, self-scanning photodiode arrays, and charge coupled device (CCD) detectors.

It was found that while discrete photodiodes in a transimpedance configuration could offer the best signal to noise measurements in theory, in practice better performance was achieved using detector array integrated circuits, such as self-scanning photodiode arrays (PDAs).

2.5.1. Discrete photodiodes

Photodiodes are specialised variants of the p-n junction semiconductor diode structure[66]. The doping of the device is controlled such that the junction region between the p-type and n-type material is very lightly doped (*eg* p-π-n), or not doped at all (p-i-n), so that the depletion region of the device is large, and well defined, under reverse bias. Photons that are absorbed by the material within, or close to, the depletion region generate electron hole pairs, which are swept apart by the electric field gradient in the depletion region. This generates an electric current, which is detected by an external electronic circuit. Except in the rare case of multiple-photon absorption, only photons of energy greater than the characteristic band gap of the semiconductor material will be absorbed, which for silicon devices corresponds to photons of wavelength 1100 nm or shorter.

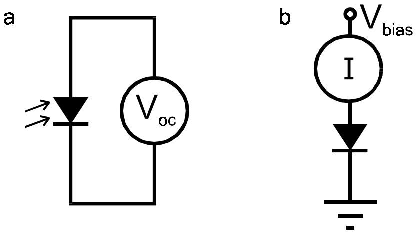

Figure 2.8 a) A photodiode in the photovoltaic mode: the open circuit voltage across the device terminals is measured. b) In the photoamperic mode the current through the device is measured, and the voltage across the terminals is kept constant at zero, or a negative value.

Photodiodes are used in one of two modes of operation[66]: in the *photovoltaic mode*, where the photodiode is connected across the high impedance terminals of a voltage measuring circuit; or in the photoamperic mode, where the terminals of the photodiode are kept at a constant voltage, and current generated by the device is measured using a low impedance current measuring circuit (figure 2.8). In the photovoltaic mode the output voltage is related to the incident light intensity[66] by equation 2.30.

$$V_{\mathrm{oc}} = \frac{kT}{q} \ln\left(\frac{I_{\mathrm{ph}}}{I_0} + 1 \right) \tag{2.30}$$

V_{oc} is the open circuit voltage across the photodiode, k is Boltzmann's constant, T is the absolute temperature, q is the electronic charge, I_0 is the small reverse saturation current of Shockley's ideal diode equation[66], and I_{ph} is the photocurrent generated in the device, which is proportional to the intensity of the light falling onto the device.

As well as being non-linear, the voltage across a photodiode in the photovoltaic mode is low pass filtered by the device shunt resistance and capacitance, both functions of the voltage across the diode, and ill-defined parameters. The photoamperic configuration is much better suited to precise measurements of light intensity. In this case the closed circuit current I_{cc} is related to the photocurrent by equation 2.31, where V_{b} is the reverse bias voltage across the diode.

$$I = I_0 \left(\exp\left(\frac{-qV_{\mathrm{b}}}{kT} \right) - 1 \right) - I_{\mathrm{ph}} \tag{2.31}$$

The current I is usually measured in an active transimpedance configuration, such as that shown in figure 2.9, and the voltage output of the circuit can be linear of several orders of magnitude. For low frequency measurements, it is preferable to user zero reverse bias; then the reverse leakage current term I_0 disappears. Although I_0 is typically very small, and is often neglected, the reverse leakage current and its associated shot noise can be the dominant noise source if the incident light level is low. If the photodiode is to be used to measure rapidly varying signals then it is usually desirable reverse bias it by a few volts. This maximises the device quantum efficiency by maximising the width of the depletion region, and increases the speed of operation of the device by reducing the junction capacitance.

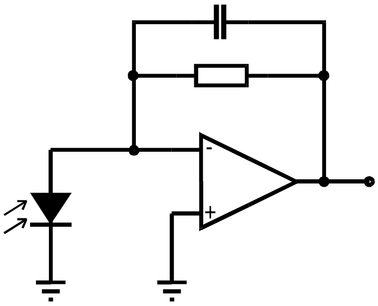

Figure 2.9 An active transimpedance amplifier circuit: because the terminals of the photodiode are both held at the same potential, the voltage output of the circuit remains linear with respect to the incident light intensity over many orders of magnitude. The capacitor is present to maintain stability and reduce the voltage noise bandwidth.

In this work optimum signal to noise ratio was required, and so the photodiode was operated unbiased. Photodiodes with low shunt capacitance lower the voltage noise gain, and may increase the circuit bandwidth. Loop capacitance may be necessary to stabilise the circuit. The operational amplifier should have an FET input stage, as the input bias currents are the dominant noise source for large transimpedance values. The other contribution to the output noise is Johnson (or thermal) noise from the feedback resistor (the value of which defines the transimpedance in this simple circuit), and the photodiode resistance. Johnson noise is an unavoidable consequence of the second law of thermodynamics, and it experiences the same gain in the circuit of through the circuit of figure 2.9 as the photocurrent. However, it can be shown that as long as the photocurrent produces more than 51.2 mV at the output, the shot noise of the photocurrent is greater than the thermal noise of the resistor. The noise performance of a photodiode is typically specified as a noise equivalent power (NEP), which is defined as the optical power input to the system which produces an output equal to that from the noise. As an example, the NEP of one photodiode in the Hamamatsu S3954 discrete photodiode array is quoted as 4×10^{-15} W/Hz^{½}.

Several prototype circuits were built for this work and investigated for suitability. Transimpedances of up to 10 GΩ were studied, and the results of this worked are summarised here: circuits with large transimpedance, above 100 MΩ become microphonic; the resistors available add considerably to the measurement noise, especially at low frequency; and large transimpedances are not useful in the event that there is any optical background in the measurement, as the amplifier will saturate. In addition the circuit complexity is proportional to the number of optical elements in any array.

2.5.2. Self-scanning photodiode arrays

In a self-scanning photodiode array a linear array of photodiodes is built into the same integrated circuit as the electronics required to sequentially read the voltage from each one, as shown in figure 2.10. Light incident onto the photodiodes creates electron-hole pairs by the same mechanism as for discrete photodiodes, but due to the FET switch, this charge is not free to flow immediately into and external circuit, and instead is integrated on the capacitance of the photodiode itself. The accumulated charge on each photodiode in turn is output on the video line (figure 2.10) by opening the FET switches individually.

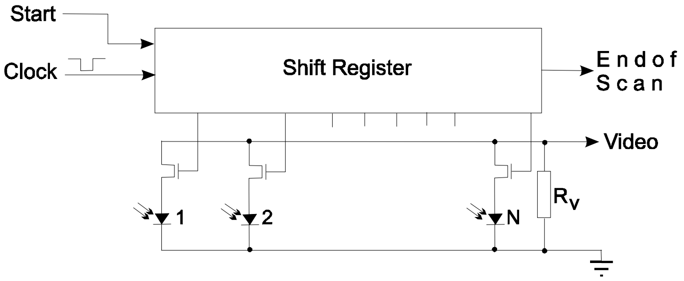

Figure 2.10 A schematic showing the sequential readout of a self-scanning photodiode array via FET switches.

Usually the only signals that need be provided to the array are a regular clock signal and a start pulse to trigger the readout cycle at the end of each integration. Errors in the output voltage are due to integration of switching transients, thermal current, and leakage current, as well as the shot noise in the full-well charge, the thermal noise of the resistors, and noise due to any readout electronics employed (accentuated by the high capacitance on the video line). The former errors are minimised in devices which use differential output of a set of active photodiodes, and a set of dummy photodiodes, identical in construction to the active diodes, but unexposed to the light. The performance of such a device offers little room for user optimisation, except in the choice of readout electronics.

The devices are not typically cooled, and the maximum achievable signal to noise ratio decreases with longer integration times due to the depletion of the stored charge by thermally excited electron-hole pairs in the photodiodes. The device quantum efficiency is similar to that of discrete silicon photodiodes. These devices have primarily found application in optical scanners, but they are migrating into spectroscopic applications, with some devices designed specifically for spectroscopy. The NEP power for each 25 µm×250 µm pixel in the EG&G Reticon self-scanning array, output through the optimum output circuitry as described in the product data sheet, was calculated from a 20 second measurement to be 3.6×10^{-15} W/Hz^{½}. This is smaller than that of the discrete photodiode example given in section 2.5.1 due to the smaller size of the diode; if the output from 144 such pixels is summed, so that the area is equal to that of the diode of section 2.5.1, then the NEP is 4.3×10^{-14} W/Hz^{½}.

2.5.3. Charge coupled device detectors

Charge coupled device (CCD) optical detectors are formed from (usually two dimensional) arrays of metal-insulator-semiconductor capacitors, linked so that the charge stored in each one may be transferred to adjacent capacitors by the correct sequence of bias signals. Charge is created in each capacitor when photons are absorbed in the semiconductor region of the device, which creates an electron-hole pair. The electron-hole pair is swept apart by the internal electric field, and the charge is trapped in the capacitor. The trapped charge can be measured by transferring it to the array output node.

Two distinct types of CCD detectors are made, named according to the process by which charge is transferred to the output: inter-line transfer (ILT), where the charge is transferred via lines of optically-inactive capacitors between each optically-active line; and full-frame transfer (FFT), where the charge is transferred through the optically-active capacitors. For spectroscopic work FFT devices are preferred, as the whole of the device area is optically active. ILT devices are used in video cameras, where interference between one frame and the next must be avoided.

In spectroscopic applications CCDs are usually operated cooled, either by thermo-electric Peltier coolers, or by liquid nitrogen, so that long integration times are possible free relatively from the build up of thermally excited charge. The quantum efficiency of CCD detectors is typically lower than photodiodes, and the dynamic range is lower; however, lower noise readout electronics is possible than for multiplexed photodiode arrays, and when operated at low temperature, they are the preferred option for detecting low light levels.

Using a 2D CCD it is possible to obtain several independent spectra from individual inputs to the spectrograph, *eg* separate optical fibres. This can be useful to make instantaneous calibrations against a reference sample for instance. When the input to the spectrograph is via a single entrance slit, then it is preferable to combine the charge stored in all the pixels of each column, in a process termed *binning*, so that the output of the device is identical to a linear detector array. Charge binning increases the signal to noise ratio of the measurement, and is preferable to external data averaging when the device readout noise is significant[67]. Based on measured values of the thermally accumulated charge and spectral response, the NEP of the Hamamatsu C5809-0907 CCD used in this work was 1.3×10^{-17} W/Hz^{½} for each individual pixel, 5×10^{-16} W/Hz^{½} for a binned pixel of area equal to the diode of section 2.5.1. (The full data sheet of this Hamamatsu detector is reproduced in appendix C, and further details are given in section 3.5.)

The dynamic range of the CCD is limited by the full well saturation, the number of electrons that can be stored in each capacitor. There are separate limits for the individual optically-active elements, and for the end of line capacitor, which must hold all the charge from a line of capacitors.

2.5.4. Electronic interference

As with all low-signal-level analogue circuitry, care must be taken in the design of optical detector circuits to shield the measured electrical signals from any potentially interfering signals from other sources. Such interference may enter the system from power supply connections, circuit interconnections, or signal interconnections between equipment. In this work, with low signal frequencies (*below 1 MHz*), interference is coupled into signal paths either by capacitive or inductive coupling; it is minimised by shielding and correct electrical grounding, as described in the following paragraphs[68].

Interference from the power supply connections can be reduced by using high-frequency bypass capacitors in conjunction with electrolytic capacitors at the supply pins of each IC used. To prevent capacitive coupling of voltages near to the signal path, the path should be kept as small as possible. Where signals are transmitted between equipment or separate circuits, a conducting shield should enclose both signal wires, and the shield should be connected to ground at one end only[68].

The grounding configuration of a circuit can introduce interference by two mechanisms: ground loops, and large currents flowing in ground return paths[69]. A ground loop is formed when more than one path to ground is possible. This configuration forms a loop around which current can flow, and any varying magnetic field which intersects it will induce current to flow around the loop. Also, it is unlikely that any two connections to ground will be at the same potential (for reasons outlined in the next paragraph), and this potential difference will also impress itself onto the measured signal. This can be avoided by using measuring devices with differential inputs: in this way ground loops are avoided, and any other common mode interference at the input to the measuring circuit is rejected.

When current flows to ground through a return path of finite resistance there will be a potential difference between any two points on it. If parts of a circuit that require high currents share the same ground return path as the signal voltages, then a voltage is impressed onto the signal voltage. This problem is avoided by using separate ground return paths for digital, analogue, and high current portions of a circuit. These ground paths should be connected together at only one point in the circuit, as close to the electrical supply as possible.

The same care to avoid electrical interference was taken for each of the detection techniques described in the previous sections of this chapter. In this way electrical interference was kept to a minimum, and in most experiments it was the shot noise of each measurement that was the dominant source of error.

2.6. Conclusions

The techniques applicable to the quantitative and qualitative study of liquids over optical fibres have been outlined in this chapter. In this work emission techniques have been chosen over absorption techniques due to ease of probe construction (single point measurements are possible), and the possibility of making non-contact measurements. Most of the work described in the following chapters has been with fluorescent compounds, but the equipment built has been optimised for Raman spectroscopy because of the specificity of this technique, and compatibility with measuring aqueous solutions.

A dispersive spectrograph was designed and built during this work: a dispersive design was chosen for its mechanical simplicity, as the aim of the work was to build compact portable instrumentation. A Fourier transform spectrometer, while having certain advantages in a laboratory setting, was not suitable for this goal. To make optimum use of a dispersive spectrometer it is vital to make use of ‘the multiplex advantage’ (the possibility of measuring light intensity at many wavelengths simultaneously), so an array detector was used. Arrays of discrete photodiodes, self-scanning arrays, and CCD detectors were all investigated during this work. For optimum compatibility with vertical arrays of fibre, low noise measurement, and low circuit complexity, a CCD detector was interfaced to the spectrograph.

All the equipment used, designed, and built during this project is described in the next chapter.

3. Spectroscopic Hardware and Software Designed and Constructed for This Work

The equipment used in this work is described in this chapter, with analysis of its performance. Much of the equipment was designed and built in the course of this work, along with the software written to control and automate the measurements. The mathematical description of the optical-fibre probes, and description of the cells, is left until chapters 4 and 5, where the different experimental configurations are described. In this chapter the components in the generalised setup illustrated in figure 3.1 are considered.

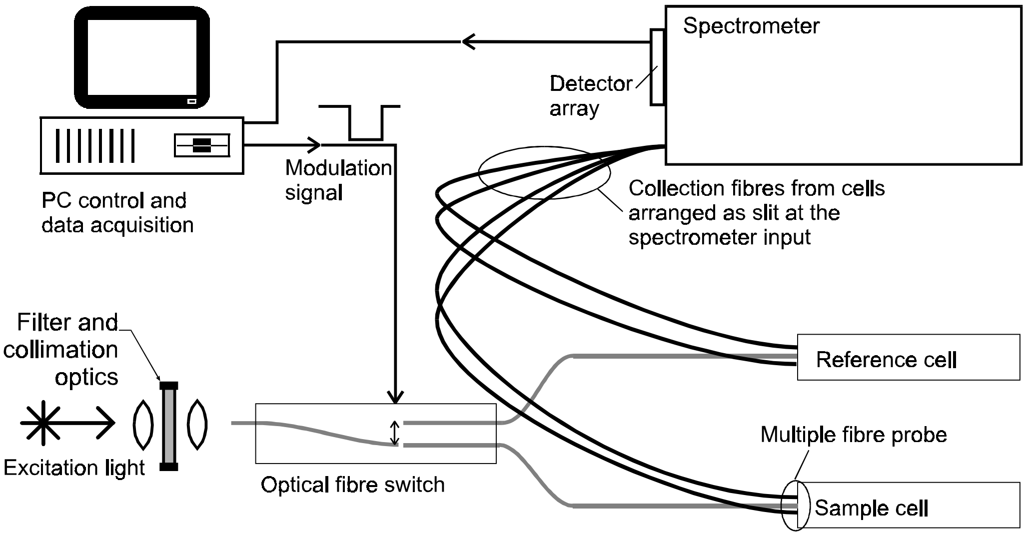

Figure 3.1 A general configuration of the hardware described in this chapter. Laser excitation light is collimated and filtered, so that only light at the laser wavelength is passed. This light is then coupled to the input port of the optical fibre switch, where, under the control of the PC, it is directed alternately to the reference cell or the sample cell. The reference cell contains a well characterised solution with similar properties to the sample (properties such as refractive index and absorption). Some of the light scattered in each of the cells is collected and transmitted by optical fibres to the input of the spectrograph, where it is dispersed across a silicon detector array. The output from the detector array is read into a PC, where the measured spectrum from the reference cell is continuously subtracted from that of the sample cell.

The description begins with the optical source, and follows the signal path through the system. The control, acquisition, and analysis software is described in section 3.6, and the benefits of the novel reference-cell-signal-subtraction scheme are described in section 3.7.

3.1. Optical Sources

3.1.1. Wavelength selection

The optimal excitation wavelength for use for remote emission monitoring depends on the grating efficiency, detector efficiency, the transmission characteristics and length of the optical fibre used to carry light to and from the sample, and the transmission characteristics of the analyte itself. The availability of suitable sources may further limit the available choice of wavelength. In this work we wish to make use of cheap, compact and high optical power laser diodes. Currently, in the wavelength range both transmitted over silica optical fibres, and detected using silicon detectors, devices are available at wavelengths centred about 670 nm, 780 nm and 810 nm.

A comparison of the efficiency of spectrographic systems based around sources at each of these wavelengths, along with the common He-Ne wavelength of 633 nm, is presented in table 3.1. It is assumed that light that is inelastically scattered to a longer wavelength is to be measured, and the parameters are chosen to optimise the system for Raman light collection. Angel[70] has shown that the fibre attenuation is insignificant for fibre lengths of under a kilometre, so if short lengths of optical fibre are used, and the optical path length through the sample is small, then the usual λ^{-4} dependence of Raman scattering intensity with wavelength is obeyed. However, the analysis also includes the effect of sample absorption (water) from an optical cell with a path length of 100 mm (section 5.3).

Table 3.1 Raman scattering and light collection efficiencies using different incident wavelengths (relative to 780 nm).

Wavelength, λ/nm	Wavelength of light shifted by 260 cm^{-1} / nm	Raman scattering efficiency	Relative detector efficiency	Relative collection efficiency with a 100 mm path length sample cell	Total relative efficiency
633	644	2.342	0.73	1.198	2.047
670	682	1.858	0.81	1.185	1.784
780 (reference)	796	1.000	1.00	1.000	1.000
810	824	0.87	1.04	0.963	0.872

A further consideration which may be necessary, depending on the particular application, is the presence of any fluorescent species in the sample. Any fluorescence from a sample is likely to mask the generally much weaker Raman light, and fluorescence can be avoided by using longer wavelength incident light. If it is intended to measure fluorescent light, then the wavelengths of the sample absorption bands should be a primary consideration in the selection of the excitation wavelength. Such factors can only be evaluated on a sample by sample basis; in this work a general system was required to demonstrate concepts and fibre-optic sampling techniques. A wavelength around 670 nm was chosen in order that Raman scattering in most samples could be observed at optimum efficiency with a silicon detector (see section 2.5) without fluorescence problems. There are also many samples that will fluoresce when excited at this wavelength, and these were used when it was convenient.

3.1.2. Semiconductor sources

To meet the dual requirements of high light intensity and monochromaticity in Raman spectroscopy, laser sources are required. To meet the constraints of size and cost, semiconductor sources were chosen for integration into the system. While small, easy to drive, and available at convenient wavelengths, semiconductor lasers have several disadvantages: large beam divergence, fluorescent background, poorly defined polarisation state, a tendency for the laser wavelength to change (especially with changes in temperature), and multiple mode operation. In this system it has been possible to work within these limitations.

Both of the semiconductor diode lasers used in this work had maximum output at 676 nm, and had half power points at 30° in the direction of maximum beam divergence. By using aspherical lenses with high numerical apertures of up to 0.5, designed and produced for use with semiconductor diode lasers, a maximum of 76% of the light can be coupled from the laser diodes into multimode optical fibre. By collimating the light from the laser diode, then passing it through cheap, narrow-band-pass, dielectric filters, as shown in figure 3.4, much of the fluorescent background is rejected.

Because light from the laser might be reflected or elastically scattered back towards the optical-fibre probe, it is important to attenuate any (broadband) fluorescent component of the incident light, which might interfere with the detection of wavelength shifted light from the sample. Care has been taken in this work to filter the laser sufficiently, as described in section 3.1.5.

The electric field vector of light from a semiconductor laser aligns itself with the broad dimension of the emitting area. While in the 180° collection geometry defined by the optical probes used in this work is insensitive to the polarisation of the incident light (a 90° geometry would be sensitive to this), the efficiency of the diffraction grating is dependant on the polarisation of the light incident on to it. In this work we have relied on the lengths of optical fibre between sample and diffraction grating to randomise the polarisation of the light incident on to the grating.

Although it is possible to produce single mode semiconductor lasers, for instance by periodically modulating the refractive index of the laser cavity, such devices are expensive. Because the wavelength resolution of the spectrograph is limited (by the size of the optical-fibres which form the spectrograph input) to 1.2 nm, multiple modes of the laser are not apparent in recorded spectra (and would never be visible in a typical, spectrally-broad fluorescent spectrum in any case). Similarly, any drift in the laser line is negligible compared with the width of the features recorded by the spectrograph, and so although it is possible to eliminate this drift by temperature stabilisation, this was not necessary in this work.

The selection of light source was influenced by application specific constraints of small size and reasonable cost. In this work two semiconductor laser diodes were used extensively, and brief details of both of these are given in the following sections. Both laser diodes were powered by commercial laser diode drivers, as noted in the text that follows.

3.1.3. SDL 7311 pigtailed laser diode

The more expensive of the two devices was an SDL 7311, from SDL Inc, CA, which was pigtailed by Point Source, UK. The diode output was 30 mW in a single longitudinal mode at 676 nm (figure 3.2), and the output from the pigtail was 21 mW. The pigtail comprised 2 m of 50 µm core diameter step-index optical fibre, terminated with an FC-type connector. This arrangement required further filtering of the light to remove the laser fluorescence, using the in-line expanded-beam device shown in figure 3.4a.

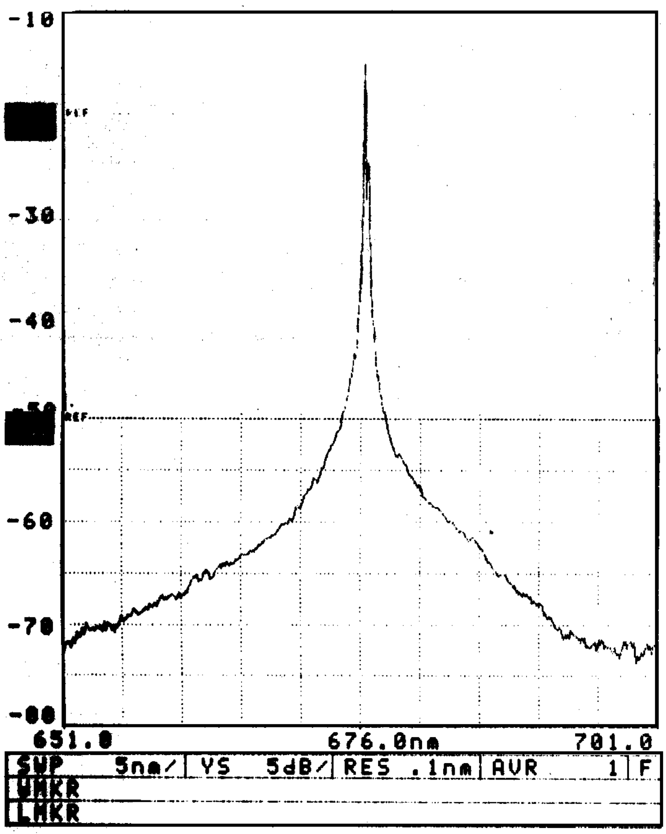

Figure 3.2 The filtered output spectrum of the pigtailed SDL 7311 laser diode, measured using an Ando Q6310B optical spectrum analyser. This picture is a composite of two measurements (showing the high and low intensity regions), and the vertical scale is in dBm. The IRE LDF-670 filter was used (see appendix D).

This device was used in the initial experiments, and was powered via an Access Pacific AP811 laser diode driver.

3.1.4. CorkOpt PC-670-D laser diode

This device was purchased unpigtailed, and also specified to output 30 mW at 676 nm. Optical filtering and lenses to couple the light into an FC-terminated optical fibre were combined in the arrangement illustrated in figure 3.4b. A maximum transmitted power of 14 mW was obtained through a 1 m length of 50 µm core fibre, when using the CVI F10-810-4 narrow band pass filter.

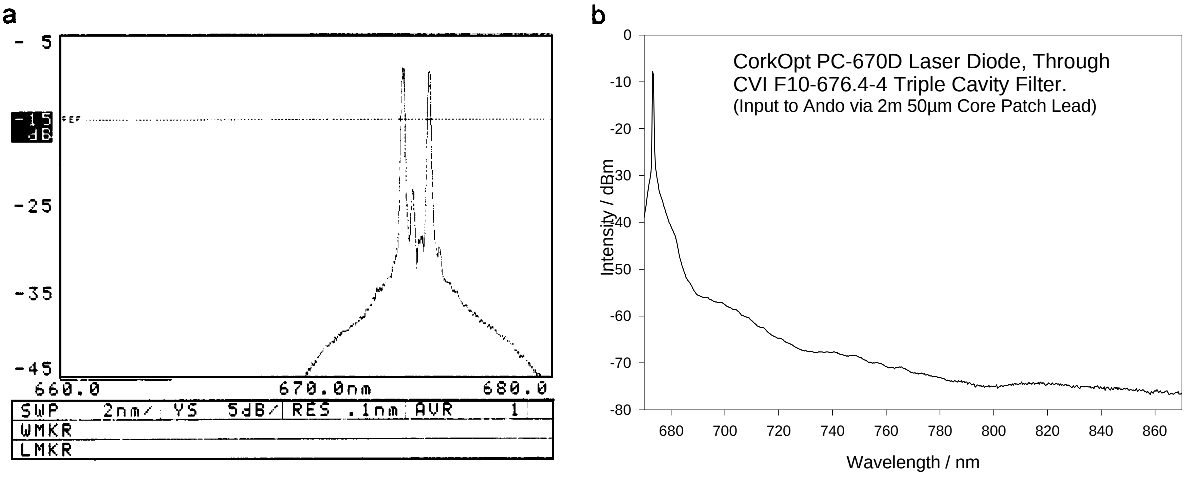

Figure 3.3 The output spectrum from the CorkOpt laser diode with a CVI F10-810-4 narrow band pass filter, measured using the Ando Q6310B optical spectrum analyser. a) A the modes in the laser line (which changed relative intensity with time). b) The fluorescent tail of the laser after filtering.

The spectral profile is shown in figure 3.3; the diode is clearly multimode in operation, with a total spectral width approaching 1.5 nm.

This device was powered using an ILX-Lightwave LDX-3412 precision current source.

3.1.5. The filtering optics

For the reasons given in section 3.1.2, it is important to filter the light from a semiconductor laser if it is hoped to measure the light inelastically scattered by it. Laser filters with a high optical density (OD, the negative log to base ten of the transmission) outside of the pass-band must be used, and in this work all of the laser filters had specified ODs greater than 4. It is necessary to use dielectric filters, as filters based on coloured glass will fluoresce. Dielectric filters often incorporate coloured glass as a substrate and additional blocking element, but fluorescence can be avoided in this case by orienting the dielectric stack (recognisable as the shiny side of the filter) away from the laser. In this way fluorescence from the coloured glass will be blocked by the dielectric layer.

It should also be noted that the transmission of light through a dielectric filter is a function of the angle of incidence, which is why the light has been collimated before filtering in this work. Although dielectric filters are available with sharp transition regions within a few nm of the pass band, in this system we have studied the wavelengths longer than approximately 30 nm than the laser wavelength, and so standard, less expensive filters were sufficient.

Two filtering and collimation devices were designed during this work, shown in figure 3.4. Both were made from 2 pieces of aluminium, which were joined together by three M3 bolts. A rubber O-ring was clamped between the two halves of the shell, and by individually adjusting the bolt tensions, the position of the output focus could be moved. The moulded aspherical lenses used in the design were anti-reflection coated for less than 1% reflection between 600 nm and 950 nm, and were mounted with a 0.5 mm pitch thread (from Thor-Labs, UK).

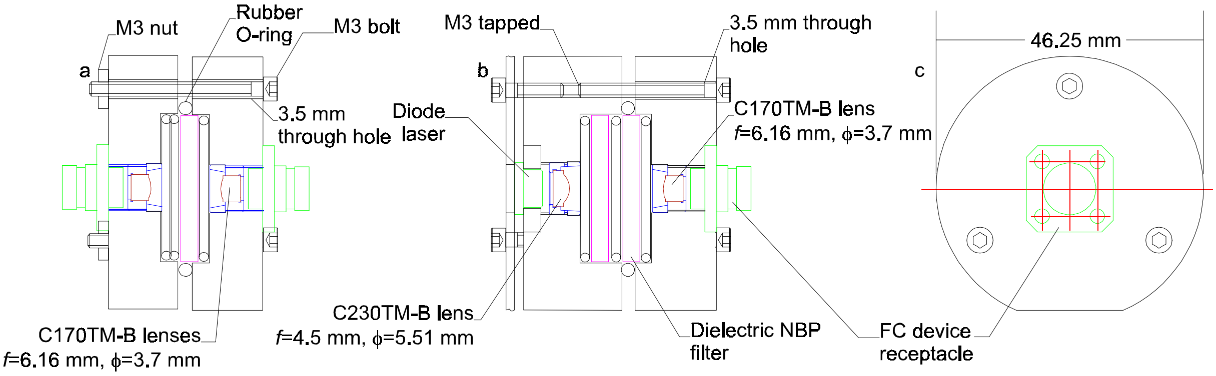

Figure 3.4 The arrangements used to filter and focus light from semiconductor laser diode sources. All lenses are anti-reflection coated so that the reflection between 600 nm and 950 nm is below 1%. a) In-line filter used with the SDL-7311; two C170TM-B lenses (Thor Labs, UK) are used. b) Focusing and coupling arrangement used with the CorkOpt diode; c) Front view; the FC device receptacle accurately holds the optical fibre at the focal position of the lens.

The loss through the in-line filter device (figure 3.4a) was measured as 0.5 dB, plus the loss through the filter that was used (see appendix D). Coupling between the laser diode and the optical fibre was measured as 75%, multiplied by the transmission of the optical filter used.

3.2. The DiCon Optical Fibre Switch

A DiCon optical fibre switch, model number S-12-L-62-FC-S, was used to electro-mechanically switch incident light between either of two optical-fibre probes. The insertion loss (measured at 1310 nm) was within 0.02 dB of 1 dB for both ports, cross talk between the output ports less than 80 dB, and the switching time below 20 mS. The switch was fitted with FC/PC optical fibre connectors on 1 m of low OH^-, 62.5 μm core, fibre at each port.

Switching pulses were provided in synchronisation with the CCD frame readout, via the custom control electronics and software described in sections 3.5.1.1 and 3.6.

3.3. Optical Fibre Bundles

Several optical fibre bundle configurations were investigated during this work, but in each case a central fibre was used to deliver light to an analyte, and the fibres surrounding it carried any scattered light to a spectrometer. The theory of such arrangements is discussed in chapter 4.

Some fibre bundles were manufactured during the course of the work, but the bundles used in the experiments described in this thesis were purchased from Oxford Electronics, UK, because the type of large-core optical fibre used was not available in the ORC. The Oxford bundles comprised 95 µm core fibres, with a 100 µm cladding diameter, and a total diameter (including a polyimide buffer) of 105 µm. The fibres were UV-grade silica, with a step index profile, and the *NA* was 0.22. One end of each bundle was supplied bonded and polished in an SMA-type connector, at the other end the fibres were loose . Three such bundles were purchased, one 40 fibre bundle, and two 20 fibre bundles.

The 40 fibre bundle was used as a straightforward fibre probe; micrographs of the tip are shown in figure 3.5. The centre fibre was identified, and the loose end was bonded into an FC-type fibre optic connector then polished to a 1 µm finish. The number of fibres from the probe which could usefully be employed to collect light was limited by the 3 mm height of the detector (described in section 3.5). A 3 mm wide, 110 µm deep, groove was machined in aluminium, and 27 of the probe fibres were bonded in to it (see figure 3.6). The fibres were chosen so those closest to the centre fibre were included in the slit, except for three fibres suspected of being fractured (due to their dim appearance under the microscope when illuminated from the loose end of the bundle). Further, the fibres were arranged within the slit so that the fibres closest to the centre fibre were closest to the centre of the slit, so that any slight mis-alignment between the slit and the detector affected only the fibres in the outer ring in figure 3.5.

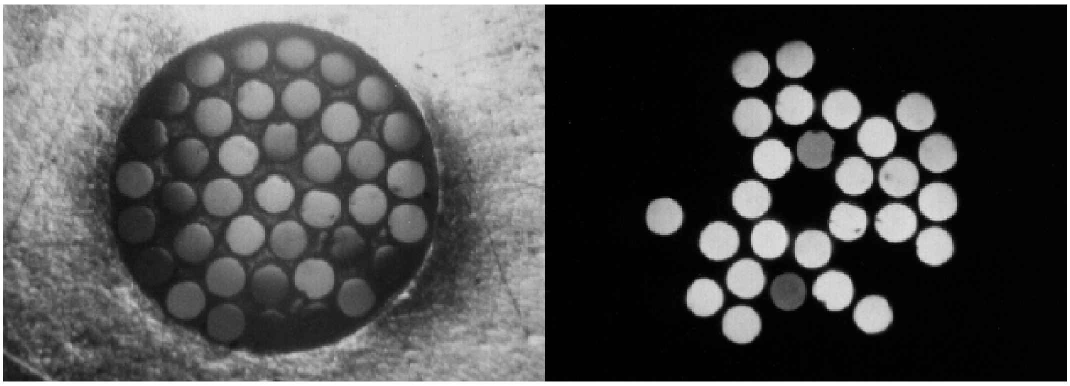

Figure 3.5 The optical fibre bundle was terminated in an SMA-type connector. The probe is shown illuminated from above in the left hand photograph, and the collection fibres (illuminated from the slit) are shown in the right hand photograph. The bundle is 0.8 mm across.

The micrograph in figure 3.7 Shows the optical fibre arrangement in the slit; the fibres are illuminated from the probe end. The second micrograph of figure 3.5 shows the same fibres at the probe end, when illuminated from the slit.

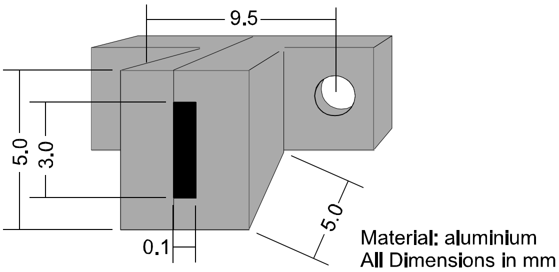

Figure 3.6 Fibres were bonded into a 2-part ferule. This linear array of fibres could then be positioned at the input to the spectrograph, forming an entrance slit. The slit is shown in this figure viewed from the front end (which points into the spectrograph).

By clamping the two parts of the slit shown in figure 3.6 together with a crocodile clip, the fibres could be threaded through the slit in the order described. The fibres were pushed through so that they protruded approximately 40 mm from the slit. Epoxy glue was then applied to the fibres at the back and the front of the slit, and the fibres were gently slid back and forth to spread the glue inside the slit. The glue was reapplied twice, and then allowed to set. The slit was then polished to a 1 µm finish on a rubber polishing mat using the same proceedure as for polishing single fibres in FC/PC connectors.

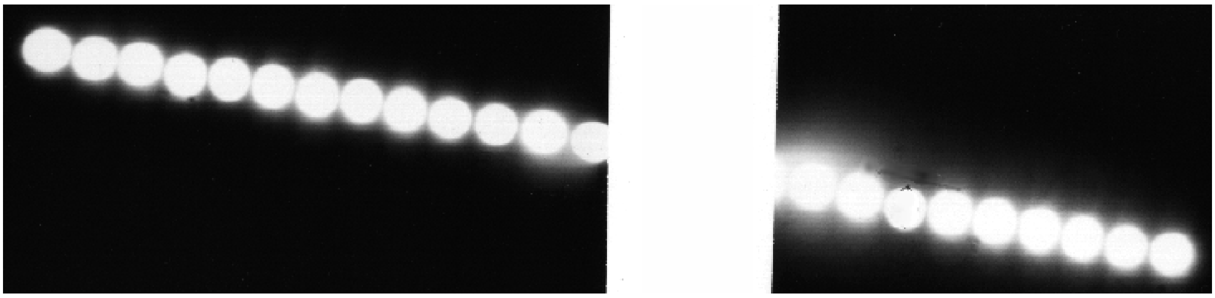

Figure 3.7 The fibres in the slit, which was positioned at the spectrograph input. The fibres are illuminated from the probe end in this micrograph. Not all of the fibres were photographed, but the packing was consistent across the slit.

The two 20 fibre bundles were used to form a bifurcated probe: the centre fibre from each bundle was bonded into a FC/PC ferrule and polished flat; the outer fibres from each bundle were interleaved in the slit, so that 13 fibres from each bundle were bonded into the slit, again with those closest to the centre fibre at the probe end of the bundles positioned closest to the centre of the slit.

3.4. Grating Spectrograph

The compromises made in the design of the spectrograph, more than any other part of the system, determine detection limits and integration times of any measurements made per milliwatt of laser power. The spectrograph must sufficiently resolve the separate wavelength components of the light input to it; at the same time optical throughput must be sufficient to ensure that the absolute signal level at the detector is measurable in an acceptable period of time; in addition, the optical signal to noise ratio must be maximised, because detector signal to noise is irrelevant if the optical signal at the detector is masked by stray light.

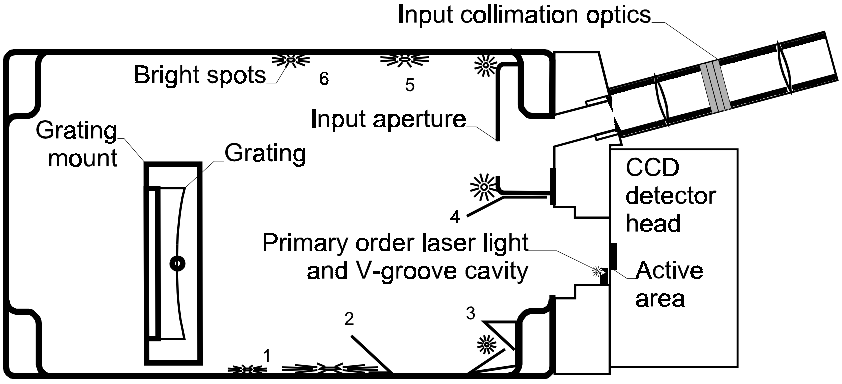

Figure 3.8 A schematic of the spectrograph. Potential baffle positions are marked 1 to 6; no baffles were used at positions 5 and 6, as they did not reduce stray light. The input (optical fibre, array of fibres, or other source) was positioned at the focus of the input collimator using an XYZ translation stage. The marked bright spots correspond to the different orders of the diffracted light at 676 nm (elastically scattered light).

A dispersive spectrograph design was chosen for this work, as, when coupled with an array detector, no movement of the grating is necessary, and the spectrograph can be made compactly using the minimum number of optical elements. To achieve the required optical signal to noise ratio, the design was based around a concave holographic diffraction grating. This was a compromise against the improved efficiency of the mechanically ruled gratings, which are produced with blazed profile to increase the efficiency of diffraction in to particular orders, but which suffer from ghost lines due to periodic errors in the ruling process.

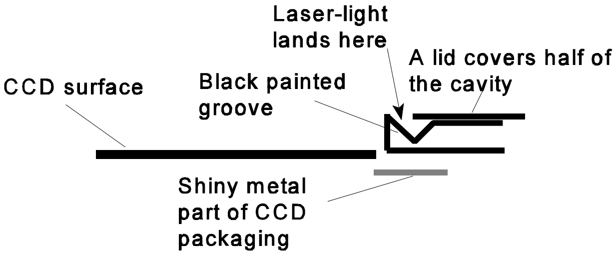

Figure 3.9 A black cavity at the end of the CCD minimised back reflections on to the grating.

3.4.1. Holographic diffraction grating

The diffraction grating was produced by Jobin-Yvon ISA, and a technical drawing based on that supplied by ISA is shown in figure 3.10, with the associated dimensions, and other information, listed in tables 3.2 to 3.4. The grating is a replica, pressed from a holographically produced master. The groove spacing is non-linear, to correct for certain optical aberrations, but 400 grooves/mm is quoted for use in the grating equation of section 2.4.3.

Table 3.2 The diffraction grating specifications, compiled from the manufacturers data.

Part number	523 00 360		
Grating number	43457		
Substrate diameter	70 mm		
Grating (ruled area) diameter	60 mm		
Radius of curvature	211.6 mm		
Groove density (and groove pitch, *d*)	400/mm ($d=2.5\times10^{-6}$ m)		
Ghost line intensity	$<10^{-10}$%		
	500 nm	650 nm	800 nm
Diffraction Efficiency	28%	32%	27%
Spectral range	480 nm to 1000 nm		
Substrate material	ZKN7 glass		

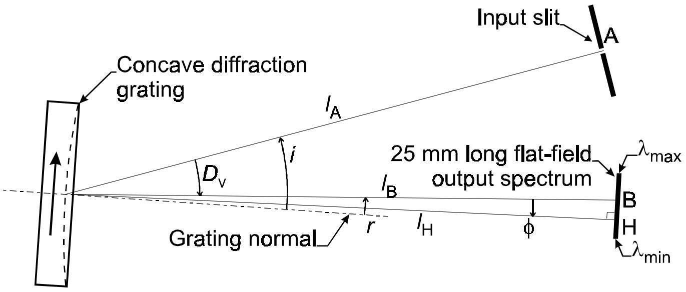

Figure 3.10 The grating arrangement in monochromator and spectrograph configurations. The input slit is at A; in a monochromator the output slit is at B, in a multi-channel spectrograph the flat-field output extends 25 mm, centred on the point B.

Table 3.3 Monochromator dimensions for the 523 00 360 grating.

Distance from entrance slit to grating centre, l_A	210.87 mm
Distance from grating centre to exit slit, l_B	206.77 mm
The deviation between the entrance and exit slits, D_v	15.75°
Diffraction order, m	-1

Table 3.4 Spectrograph dimensions using the 523 00 360 grating.

Length of the flat field spectrum	25 mm
Shortest distance between the flat field spectrum and the grating centre, l_H	206.63 mm
Angle between spectrum normal , l_H, and l_B, ϕ	2.08°

Extreme parameters:	λ	i	r	Entrance dispersion	Flat field dispersion
λ_{min}*	474 nm	-15.12°	4.09°	11.4 nm/mm	12.1 nm/mm
λ_{max}*	1000nm	-17.76°	-5.47°	11.3 nm/mm	11.9 nm/mm

*NB; λ_{min} and λ_{max} are for different grating rotations.

When the deviation D_v between the input slit and the output slit is constant, and the grating is rotated so that the angle of incidence i is varied, i is related to wavelength λ at the output by equation 3.1

$$i = \arcsin\left(\frac{m\lambda}{2d\cos\left(\frac{D_v}{2}\right)}\right) - \frac{D_v}{2} \tag{3.1}$$

If the grating is to be used in the spectrograph mode, where all optical components are stationary, then the angle between the input slit and the normal to the flat-field output spectrum is $D_v+\phi$. A 300 nm region of the spectrum within the range 400 nm to 1000 nm is dispersed across the flat-field output, selected by rotating the grating.

3.4.1.1. Grating mount

The mount designed for the grating (shown in figure 3.11) allows rotation of the grating about its axis of bulk cylindrical symmetry, rotation about the axis parallel to the grooves and tangential to the thinnest part of the grating, and tilt about the axis perpendicular to the grooves and tangential to the centre of the grating. The grating back plate was attached to the back of the diffraction grating using acrylate based “super glue”. It was aligned normal to the grating grooves.

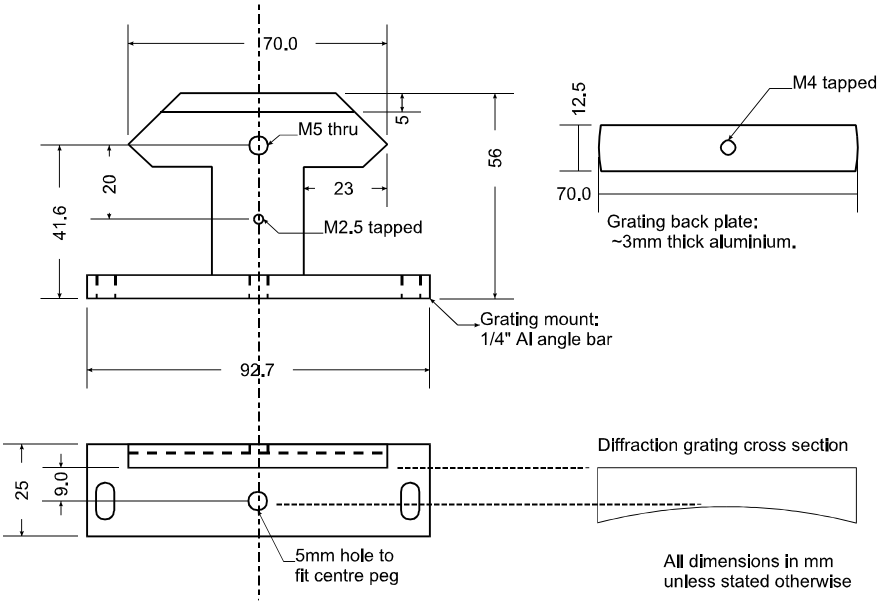

Figure 3.11 The grating mount used to position the concave holographic diffraction grating within the spectrograph.

3.4.2. Input collimation optics

Figure 3.12 shows the optical arrangement at the spectrograph input. The optical source (*eg* optical fibre) is positioned at the focus of the first lens using an XYZ translation stage, and the collimated light is filtered through 9 mm of long-wave-pass colour glass. The second lens refocuses the light at a 3.5 mm × 0.1 mm slit, at the focus of the concave diffraction grating.

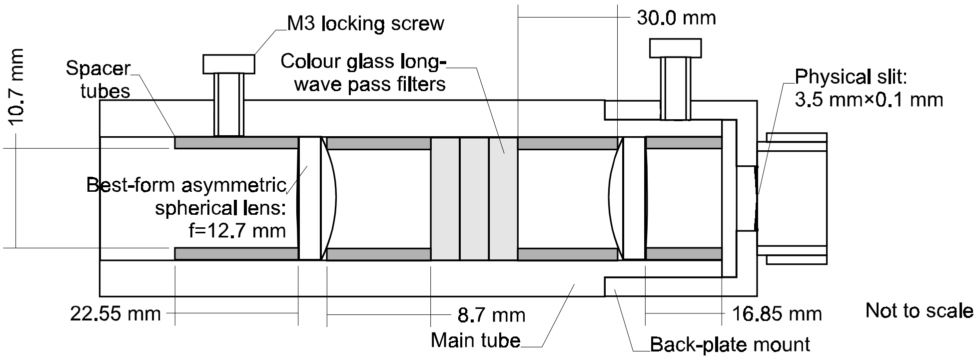

Figure 3.12 The lens and filter arrangement used at the spectrograph input.

The outer surfaces of the two end filters were coated with the same AR coating as the lenses, $R<0.25\%$ between 670 nm and 1000 nm, and index matching fluid was put between the inner filter surfaces. However, because of the physical slit, any stray light formed within the input collimator does not degrade the resolution of the spectrograph. Although the *NA* on the input collimator was less than that of the fibres, it matched the grating *NA*, so spectrograph throughput was not affected. The absorbance of 3 mm thickness filters are shown in appendix D.

3.4.3. Baffles and beam traps

After the light from the input slit strikes the diffraction grating it is dispersed by the diffraction grating it is dispersed by three mechanisms: diffraction from the grating grooves, random scatter, and diffraction from periodic errors in the groove spacing (ghost lines). Any light that is not scattered into the desired diffraction order will interfere with the input signal if it is subsequently arrives at the output of the spectrograph.

Most of the light scattered away from the detector is properly diffracted according to equation 2.23, but a significant fraction of it is in the unused orders. The efficiency of the holographic grating used in this work was approximately 30% over the range 600 nm to 900 nm, see table 3.2, that is 70% of the light might possibly arrive at the detector as stray light. Fortunately, the path of this light is well defined (because the grating is fixed, and the range of input wavelengths is well defined), and it is easy to mount baffles at appropriate positions within the spectrograph to shield the detector from any bright spots on the spectrograph wall.

Initially 5 baffles were mounted in the spectrograph, at the numbered positions in figure 3.8. In order to determine the effect of each one, a 20 mW signal was input directly into the spectrograph, and the detector output was recorded. Each baffle was removed in turn, and the detector output measured again. Removing the baffles at positions 1 and 5 made no difference to the stray light levels, and they were not replaced. Including The remaining baffles reduced stray light at 676 nm by 3.4%. Most of the stray light landing on the detector comes directly from the surface of the grating, as randomly scattered light.

Random light is more insidious, and impossible to completely eradicate due to the nature of the grating substrate (it is impossible to fabricate a perfect mirror even). However, it is a weak phenomenon, and only random scattering of signals several orders of magnitude greater than the signals under investigation can be detected. As the only potential source of light at this intensity is the laser, which is blocked by the input filters, this source of error is negligible.

The holographic grating used in this work has negligible ghosting quoted as $1:10^{10}$, negligible for the purpose of this work, again due to the filtering of light at the laser wavelength at the spectrograph input.

One further potential source of interference is from reentrant spectra: light incident on the detector is reflected by Fresnel reflection, and depending on the geometry of the spectrograph may arrive back at the grating, where it is re-diffracted to a different position on the detector. This can be completely eliminated, at the expense of resolution, by tilting the diffraction grating so that the reflected light does not arrive at the grating, although this was not done in this spectrograph.

Reentrant light at the laser wavelength, reflected from the edge of the detector packaging, caused problems in some of the early measurements made with the spectrograph. This was minimised by inserting the beam trap shown in figure 3.9.

3.4.4. Measured spectrograph performance

The spectrograph throughput was measured as 25%±3.8% at 633 nm, using the arrangement of figure 3.13. The fibre was positioned directly at the input to the spectrograph, without the input optics described in section 3.4.2.

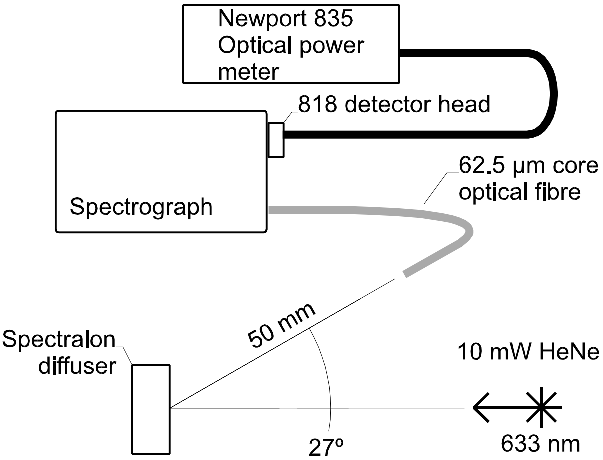

Figure 3.13 The arrangement used to measure the spectrograph throughput. The 62.5 µm, step-index core fibre was positioned at the spectrograph input using an XYZ translation stage.

3.5. Detector Electronics and Control Hardware

A Hamamatsu silicon CCD detector was positioned at the output plane of the spectrograph, which was controlled in synchronisation with the optical fibre switch via custom hardware and software. The active area of the detector was 12.5 mm long, and covered a spectral range of 150 nm.

3.5.1. Hamamatsu CCD detector

The Hamamatsu CCD detector was supplied built in to a package containing a Peltier-type thermo-electric cooler, and most of the electronics necessary to maintain the cooler at a temperature of 0ºC, and to provide the multiple clock phases to the CCD IC itself. The detector active area was 12.28×3.07 mm, formed from 512×128, 24 µm-square pixels. Although the device is a 2-dimensional array, the charge in each column of pixels was binned in each measurement, so the output was equivalent to that from a linear array of 512 elements, each 3.07 mm tall. Complete specifications for the device are given in the data sheets reproduced in appendix C.

Thermally generated electrons degrade the dynamic range and signal to noise ratio in any single measurement period, from the shot noise contribution of the thermal noise, and because the CCD pixels become saturated by thermally produced charge. The rate of thermal charge accumulation has been measured as 450 electrons/pixel/second (averaged over the whole CCD surface).

Assuming that all of the pixels in a column are illuminated and binned, the signal to noise ratio of the detector is given by equation 3.2.

$$\frac{S}{N}=\frac{E_{\mathrm{in}}\cdot A_{\mathrm{pix}}\cdot\#\cdot\tau\cdot(S_{\mathrm{d}}/q)}{\sqrt{E_{\mathrm{in}}\cdot A_{\mathrm{pix}}\cdot\#\cdot\tau\cdot(S_{\mathrm{d}}/q)}+\sqrt{D\cdot\#\cdot\tau}+N_{\mathrm{r}}} \tag{3.2}$$

The terms in the denominator are (from left to right) the shot noise due to the incident light, the shot noise in the accumulated thermal charge, and the readout noise. E_{in} is the irradiance at the detector input, A_{pix} is the pixel area, # is the number of pixels in a column (equal to 128), τ is the integration time, S_{d} is the detector responsivity, q is the charge of an electron, D is the rate of accumulation of thermal charge, and N_{r} is the readout noise in electrons.

3.5.1.1. Control and readout electronics

The CCD detector head requires a clock signal at a frequency up to 1 MHz, and start pulses to initiate readout of the CCD device. These signals were generated by a LabPC+ data-acquisition card (National Instruments, CA) under software control (see section 3.6), however, digital buffer circuitry was required, and a schematic diagram of this is shown in figure 3.14. Power was supplied to the CCD from 2 OEM-type linear power supplies one specified for ±15 V at 0.72 A and 5 V at 2.7 A, the other for +24 V at 0.45 A (part numbers IHBAA-40W and IHA25-0.5 from International Power, CA, supplied by XP Plc, UK). The power supply and buffer circuitry was built into the same case; all connections to the CCD were via a 15-way D-type connector, and connection to the LabPC+ card was via a 2 m long, 50-way ribbon cable terminated with IDC-type connectors. The analogue output from the CCD was routed directly from the 15-way D-type connector to the 50-way IDC cable by a soldered connection. A data sheet for the LabPC+ card is reproduced in appendix C.

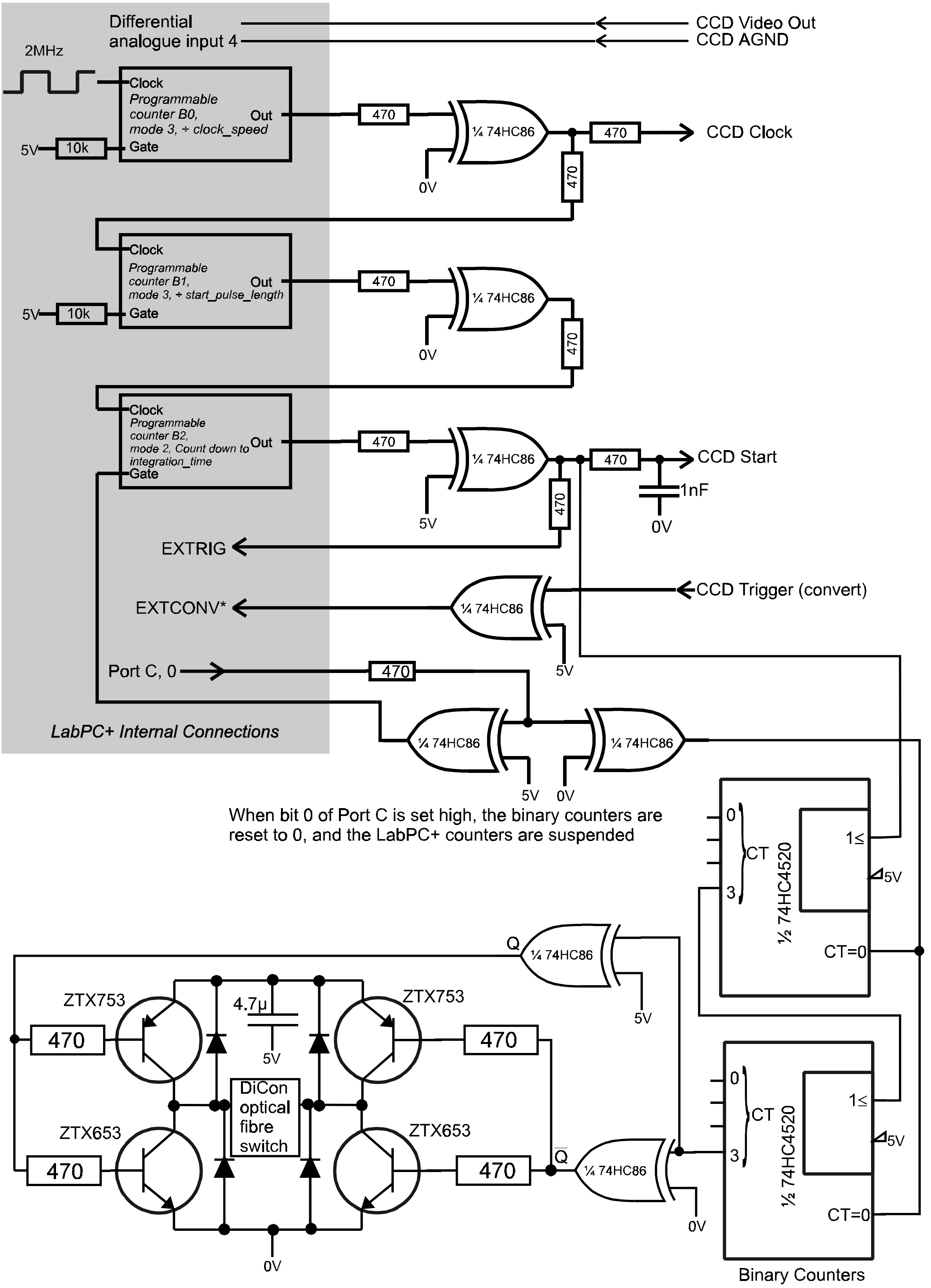

Figure 3.14 A schematic diagram of the control and buffer electronics used to interface the CCD counter to the LabPC+ data acquisition card.

The CCD output voltage was measured by the LabPC+ analogue-to-digital (ADC) converter. This has 12-bit resolution, and a minimum conversion time of 12 µS. The ADC has a software controllable pre-amplifier gain of up to 100, which allows low-level signals to make best use of the 12-bit resolution. The ADC was configured in dual input differential mode (as opposed to single input earth referenced mode); this reduces interference from external noise sources to a minimum. Care was taken to avoid ground line noise by using low inductance ground paths, and isolating the signal path from electrical earth at all parts of the circuit. A 1.5 m long coaxial cable was used to carry the output signal between the CCD head and the 15-way D-type connector, and the 50-way IDC cable was shielded with 3 layers of aluminium cooking foil.

3.6. Control Software

The data acquisition software for this project was written using the ANSI C-conforming National Instruments compiler, *CVI version 3.1*. The operation of the software written to control the Hamamatsu CCD detector, and the source code, is described in appendix B. An overview of the operation of the software is given in this section.

The program, called ccdarray.exe, runs under Microsoft Windows 3.1, and controls both the CCD array and the DiCon optical-fibre switch, which is moved in synchronisation with the CCD frame time. As well as controlling the hardware, the software must display the recorded data, and make certain system corrections. A relative intensity correction with wavelength can be applied to all measured spectra. This corrects for detector photo-response non-uniformity, variations in the detector quantum efficient with wavelength, variations in the grating diffraction efficiency, the input filters at the spectrograph input, and the transmission of the optical fibre bundle used in this work. This correction was derived using a black body source (Optronics Laboratories OL480), at a temperature of 1200ºC and a 0.0125 inch aperture.

All operation of the CCD is controlled via the software window shown in figure 3.15. The File menu controls the recording of data, and the setting of any system background subtraction to be made; the Read_CCD menu is used to start data acquisition, in either *single reading*, *multiple reading* (*ie* averaging), or *continuos reading* mode; and the Axes menu controls the format of the axes used to display the data. The range of the intensity axis can be varied, and it may be switched between either a logarithmic or a linear scale; CCD column number, wavelength, or frequency shift from the laser wavelength can be displayed on the other axis.

All the operating parameters of the the LabPC+ card (preamplifier gain) and the CCD (clock period, start pulse length, and integration length) are set, and continuously displayed, on the front panel. Software operation is also controlled via the front panel. The *System Correction* control selects between no correction, correction for the CCD and grating efficiency only, or correction for the entire optical path from the optical-fibre probe to the detector. The *Averages* control sets the number of averages to be made, in groups of 24. While groups of 24 is arbitrary (it is convenient to fill a memory array which is already defined in the ccdarray program), it should be noted that the CCD displays a noise component with a period of 4 readout cycles (see appendix C), so any averaging should be in multiples of 4.

The *Read Mode* control selects between *normal*, *background subtracted* (which subtracts a previously stored background from each measurement), and *reference cell subtracted* (which subtracts spectra from a reference cell from a subsequently recorded spectrum from a sample cell, in conjunction with the DiCon optical-fibre switch and Oxford Electronics bifurcated fibre-bundle). The *Shots* control may be set from 1 to 25, and determines the number of sequential spectra recorded in each data set.

Also on the front panel is space to record the data file name, text describing the probe configuration, and other any comments, which are all saved in the data file. The most recently acquired spectrum or average is displayed on the graph, and when the aquisition is complete, the individual spectra in the set can be displayed using the arrows on the *Displayed Spectrum* control (double click it to automatically step through each spectrum).

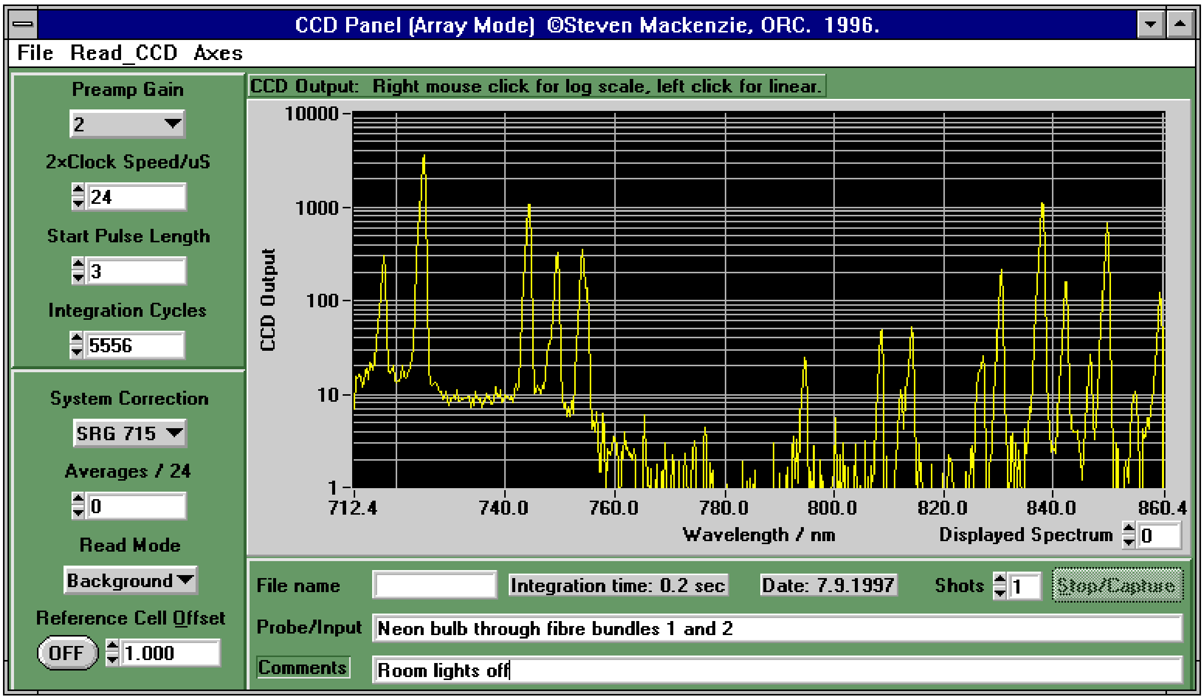

Preamp Gain: 2
2xClock Speed/uS: 24
Start Pulse Length: 3
Integration Cycles: 5556
System Correction: SRG 715
Averages / 24: 0
Read Mode: Background
Reference Cell Offset: OFF 1.000
Displayed Spectrum: 0
File name:
Integration time: 0.2 sec
Date: 7.9.1997
Shots: 1
Probe/Input: Neon bulb through fibre bundles 1 and 2
Comments: Room lights off

Figure 3.15 The interface to the CCD Array readout program. Data is acquired and saved using the menu bars at the top of the screen. System parameters are entered directly into the boxes in the window. All parameters, the date, and any comments typed into the appropriate boxes are saved with the data. Here the intensity is shown plotted against a log scale to accentuate the lower peaks and the readout noise.

Data is filed by using the *File data* option from the *File* menu, and the intensity profiles for each of the recorded spectra is saved in columns as ASCII text, along with other information, as shown in figure 3.16.

```
Hamamatsu C5809 CCD Data. Date: 27.7.1997
Read mode:    1
LabPC+ ADC gain:    1
Integration Time: 2.000160e-01 seconds
No. of averages:    0
System correction:    3
Probe/input arrangement: fibre 2, 4.5mL/L of 600mg/L PB -+4%, 14.9mW
Comments: 5x24 readings in background, laser = 134.2mA
     Wavelength/nm  Wavenumber shift   Normalised data
        860.660000       3209.005178     -3134.819149    -200555.657909    -179129.950854
        860.370400       3205.094235         1.083672          1.083672          5.727958
        860.080800       3201.180658        -0.308891         -0.308891          7.799513
        859.791200       3197.264445         0.142926          1.286336          7.003382
```

Figure 3.16 The first 14 rows of a typical data file from the program ccdarray.exe. Three columns of data have been recorded in this example; each data set comprises 512 points, corresponding to the 512 CCD columns.

The first line of the data file is a line of text which identifies the source of the file, and the date on which it was recorded. An integer is recorded for the read mode (0=normal, 1=background subracted, 2=reference cell subtracted), and for the system correction (0=none, 1=CCD and grating only, 2=undefined, 3=full system correction). If no averaging was performed then the number of averages is recorded as 0, otherwise the total number of readings that are averaged in each spectrum is shown.

3.7. Signal Processing Schemes and Reference Cell Subtraction

Of the automatic data conditioning described above, the system correction and background subtraction schemes are commonly found in many instrument control packages, supplied with commercial spectroscopy equipment. Even so, correction for instrumental response is often omitted in measurements using dispersive equipment[71], although not in the measurements presented in this work.

The reference cell subtracted mode is an original element of this system, and its operation and effects will be described in this section. The technique should allow the detection level of any impurity to be reduced, by continuously comparing the signal from the analyte, in the sample cell, to that from a reference sample of well known characteristics. This compensates for any drift in the components of the system, or in the properties of the sample itself, due to environmental changes. The effect of the referencing is similar to using a lock-in amplifier technique, but more effective, as offset originating in the sample itself (such as any background fluorescence) is rejected too. The essential elements of the scheme are shown in figure 3.17, which is a copy of figure 3.1, repeated here for convenience. Although the technique is illustrated here with optical-fibre probes, it is equally appropriate to use any other method of light delivery and collection. It is, however, particularly convenient to use optical-fibre probes because of the ease with which they may be positioned and interfaced with different samples.

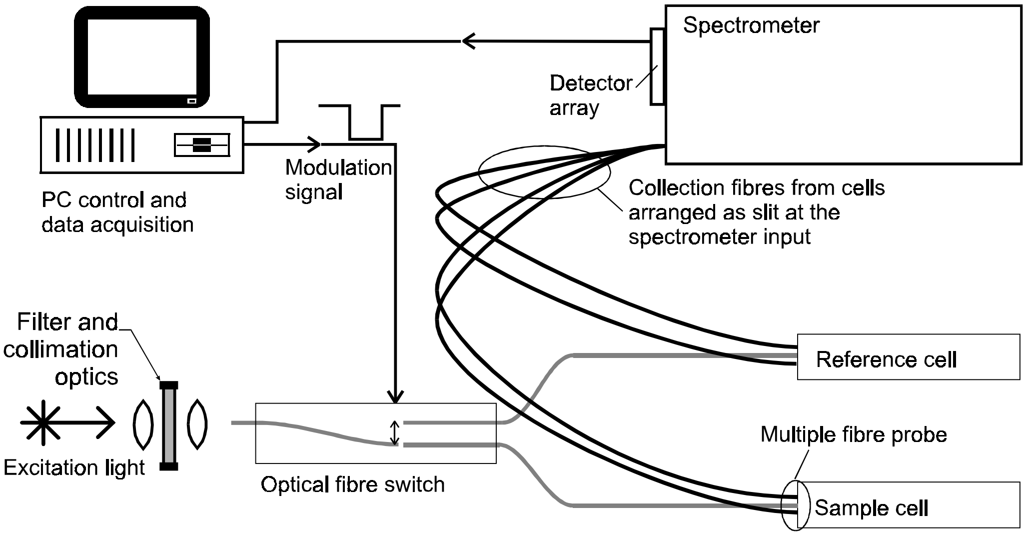

Figure 3.17 (Figure 3.1 repeated.) A general configuration of the hardware described in this chapter.

Unfortunately, it was not possibly to evaluate this technique experimentally, due to a cracked delivery fibre in one of the arms of the bifurcated fibre probe. Time constraints prevented the reassembly of the bundles for proper evaluation.

3.7.1. Operation

Excitation light is delivered to each cell in turn via the centre fibres of the bifurcated probe described in section 3.3. The excitation light is periodically switched between the two cells so that each cell is illuminated for the same amount of time. This switching is controlled via the timing circuitry of the Lab-PC+ card and the CCD buffer circuitry, as shown in figure 3.14, so that 32 consecutive readings from the CCD are made; the first 16 with the referenced cell illuminated, and the last 16 with the sample cell illuminated.

Light scattered from the samples and collected by the fibre probes is delivered to the spectrograph via the slit arrangement described in section 4: 13 fibres from each bundle are interleaved in a vertical array. The light from the fibre is dispersed onto the CCD detector, and measured using the 12-bit analogue to digital converter of the LabPC+ card. Because during the finite switching time of the optical fibre the reading from the CCD is spurious, the first and last reading from each cell is discarded. The average of the 14 valid readings from the reference cell is then subtracted from the average of the readings from the sample cell, and this result is stored as running average. This cycle is repeated as required.

Any offset between the readings from the two cells, which may be caused by extra attenuation in one port of the optical fibre switch, or differences in the collection efficiencies of the fibre probes, can be recognised by differences between the intensity of common features in the two spectra. In the case of an aqueous solution, a suitable reference might be one of the Raman bands of water, for instance. Such differences may be removed either by scaling the recorded output from one of the cells by a suitable constant during the data processing (an option which has been built in to the ccdarray program), or by attenuating the light delivered to one of the cells by some mechanism.

3.7.2. Effect on the signal to noise ratio.

If the noise in the measurement electronics is negligible, then the effects of increasing the integration time of the CCD, or averaging many frames from the CCD (and then perhaps subtracting a previously measured background), are similar to those of a low pass filter at the

CCD output: high frequency noise is removed from the measured signal. The longer the measurement time T, the lower the effective frequency cut-off of the measurement (approximately $2\pi/T$), and the better the signal to noise ratio.

Alternatively, by constantly subtracting the background measured from a reference sample, which shares all the features and the environment of the signal from the analyte, variations over a period any greater than the time taken to measure one referenced spectrum, t, (32 CCD frames for the equipment as set up in this work) are also rejected, setting a high-pass cut-off of approximately $1/t$. In this way the system behaves as a narrow band pass filter, better than the simple low pass filtering effect of long integration time and background subtraction. This could be especially significant if pink noise, which has a power spectrum that is inversely proportional to frequency, is a significant feature of the detector output, such as from a photodiode in combination with a transimpedance amplifier.

3.7.3. Possible causes of error

The results from this signal processing scheme may be adversely affected by any detector non-linearity with optical power. This would be apparent if there was a significant difference between the average intensity collected from each sample, perhaps due to a gross coupling mismatch between one probe and the sample, or because of a strong background emission from one sample, and hence an offset between the signal measured from the two cells.

3.8. Conclusions

The major items of equipment that have been designed and built, or purchased, for use in this work have been described in this chapter, as has the software which was written to control the CCD detector and optical switching, and to condition the measured data.

The resolution of the spectrograph is limited by the diameter of the optical fibre cores at the entrance slit. The optical fibres used in most of the work described were 95 µm core diameter (105 µm outer diameter), limiting the wavelength resolution to 1.2 nm. Using smaller diameter core fibre (of the same outer diameter) would give better resolution, but decrease the amount of light collected by the optical fibres (see chapter 4). A resolution of 1.2 nm was sufficient for the characterisation of the system elements described in this thesis. However, when monitoring analytes with particularly narrow spectral features (such as Raman lines, which can be less than

1 cm^{-1} (0.05 nm at 700 nm)), then a higher signal-to-noise ratio could be achieved with better resolution. The resolution improvement should be achieved using a diffraction grating with a higher dispersion (which would not alter the optical power incident onto the detector). Better resolution achieved by using a narrower physical slit in the spectrograph, or by using optical fibres with a smaller core diameter, results in a lower collected optical power, and no overall signal-to-noise advantage. A decreased spectral range could be acceptable if specific analytes were to be monitored, with characteristic features within a small spectral range. (Better resolution offers no advantage if the spectral features are broader than the spectrograph resolution.)

A 676 nm semiconductor laser source was used during this work so that a wide range of samples could be studied, with emitted light in the region of optimum responsivity of the silicon detector. The measured characteristics of the semiconductor lasers used have been presented (the characteristics of the optical filters used in this work are given in appendix D). The components in, and the construction of, the spectrograph have been described, with the measured performance of the system. The operation of the spectrograph depends on computer control, and the electronic and software interface has been described (a full software listing, and further details of the software operating procedures are given in appendix B). Finally, a description of the advantages of the novel data averaging techniques available using the software and bifurcated optical-fibre probes have been given.

A selection of Raman spectra measured using the spectrograph are presented in appendix E.

4. Optical-Fibre Probe Designs

The intensity of Raman scattered light, or the fluorescent light from a *weak* solution of an analyte, is always much less than the intensity of elastically scattered light. For optimum signal to noise ratio measurements of fluorescent or Raman emission the collection of any elastically scattered or reflected light must be avoided. As was mentioned in chapter 2, the elastically scattered light may often be concentrated in the forward direction, but fluorescence and Raman scattered light is equally intense in the forward and backward direction. A back-scattering collection geometry, collecting light scattered directly back towards the light source, is therefore the most desirable arrangement, as the ratio of inelastically scattered light to elastically scattered light that is collected is raised[2]. This is also a particularly convenient arrangement for any remote measurement, as access to the sample is only required at one point.

In this work the theory of fluorescent or scattered light collection via single and multiple optical-fibre probes has been addressed. In this chapter mathematical models for such optical-fibre probes are derived in terms of the fundamental parameters of the analyte and probe, and shown to be more accurate and complete than any previously published models found by the author.

4.1. Review

4.1.1. Single-fibre probes

Only a single optical fibre is necessary to perform extrinsic measurements of wavelength-shifted, *ie* inelastically scattered light (figure 4.1). Probes of this type are small, cheap, and efficient collectors of scattered light. They are commonly used for fibre-remoted measurements of fluorescence and absorption in the UV-VIS-NIR regions of the electromagnetic spectrum.

---

[2] In this work, and especially in this chapter, the light incident onto, or into, the sample has been referred to as the *emitted* light (because it is emitted from the probe). It may also be termed excitation light, and other authors may then term any subsequently scattered light, as well as light that is absorbed and then re-emitted, as emitted light.

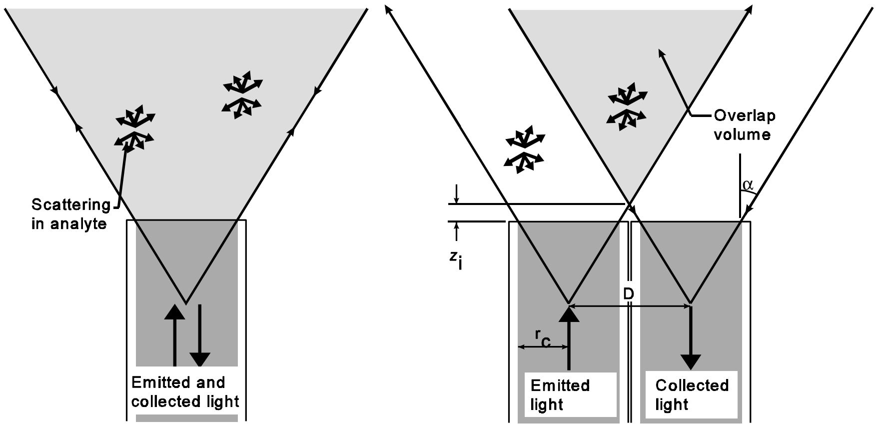

Figure 4.1 a) A single-fibre probe; the overlap between the emission cone and the collection cone is complete. b) A multiple-fibre probe; light is only collected from part of the illuminated volume, as the emission cone and collection cone do not completely overlap, and no light is collected from the region $z<z_i$.

However, the sensitivity of measurements made with a single-fibre probe can be limited by back reflections (Fresnel reflection) from the fibre tip. Polishing the tip of the fibre at an angle can direct the light reflected at the probe tip out of the optical fibre, but collection of the distributed backscatter from the whole length of the fibre is unavoidable. Although a spectrometer with suitably high stray light rejection may be able to remove virtually all of the scattered and reflected light at the incident wavelength, when a single-fibre probe is used then Raman scatter and fluorescent light, both originating within the fibre core, will interfere with weak signals from the analyte.

The unwanted fibre fluorescence, which is normally particularly troublesome with UV or short-wavelength visible excitation, is less intense when using high OH^- content (wet) silica, UV-grade, fibre. Generation of Raman light within the silica cannot be similarly avoided as this broadband scattering results from the vibrations in the glass itself, although these vibrations are all below 1400 cm^{-1}. A measured Raman spectrum of pure silica glass is shown in figure 4.2. These interfering components can be almost entirely rejected from measurements made through multiple-optical-fibre probes by using filters at, or close to, the fibre probe tip[72][73].

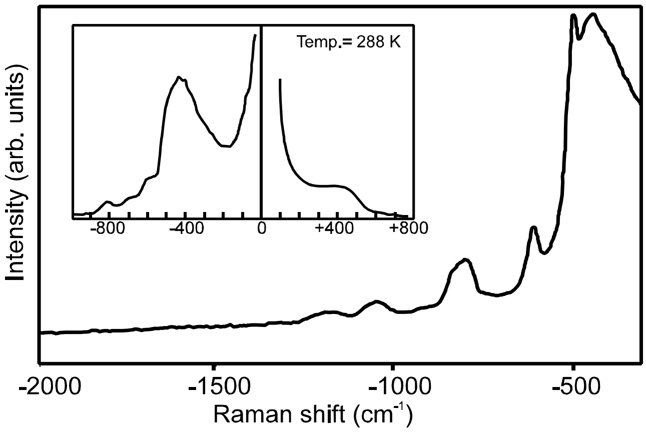

Figure 4.2 The (Stokes) Raman spectrum of a vitreous (fused) silica fibre, recorded by Ma[73], with the low wavenumber and highly temperature dependant anti-stokes spectrum shown inset.

4.1.2. Multiple-fibre probes

If separate optical fibres are used to carry light to and from the probe, then the optimum placement of optical filters can be used to reject any potentially interfering light. A narrow-band-pass filter after the emission fibre ensures that only light at the laser wavelength reaches the analyte. A notch filter (or a long or short-pass filter) before the collection fibres, or close to the probe tip, can remove any elastically scattered (unshifted) light which could generate fibre Raman or fluorescence between the analyte and the spectrometer. Because much more unshifted light than shifted is usually collected in a Raman measurement, removing this component can reduce the stray light within the spectrometer too.

There are two broad classes of multiple-fibre probe: those where separate delivery and collection fibres are used in the probe, and those where the light from the delivery and collection fibres is multiplexed into a (short) length of a single fibre. Probes in the first category are less efficient than those in the second, due to the incomplete overlap of their emission and collection cones. Probes in the second category can have efficiencies approaching those of single-fibre probes. Light can be coupled in and out of the short sensor stub via a dielectric colour-separation filter, which can efficiently reflect light in one band of wavelengths while transmitting light outside that band. The emission and collection cones then overlap as in a simple single-fibre probe, unfortunately filter transmission is typically below 80% if a sharp transition between transmitting and reflecting regions is required.

A further advantage of using bundles of optical fibres to collect light scattered from an analyte is that a circular light-collection area is easily transformed to match a linear slit at the spectrograph input. Light is usually most efficiently collected from a circular region of the analyte (for instance around a focused spot of excitation light). The resolution of a dispersive spectrometer (*ie* one in which the different wavelengths of light are separated by a diffraction grating or prism) is usually limited by the width of the input slit. By rearranging the collection fibres as a linear array, all of the light collected from the circular input aperture can be coupled through a spectrometer input slit, with the same f-number as the collection fibres. (This would be impossible to achieve using conventional optics: either the image of the circular collection aperture must be demagnified, requiring a lower f-number input slit, and potentially overfilling the internal optics of the spectrograph; or part of the image of the collection aperture must be discarded, with consequent loss of signal.)

4.1.3. Improving the efficiency of optical-fibre probes

The amount of light collected by multiple-fibre probes may be increased either by arranging the collection fibres at an angle to the emission fibre, or by angle-polishing the tips of the emission and collection fibres (figure 4.3). An angle of 9° between fibres of *NA* 0.22 will increase the collected light intensity by about 70% with respect to parallel fibres in a clear colourless analyte of refractive index 1.33. The optimum angle increases as the fibre *NA*, or the sample refractive index increases[74].

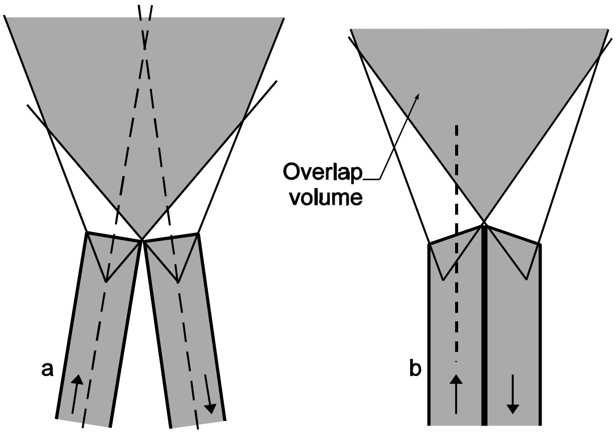

Figure 4.3 The overlap between the emission and collection cones may be increased by a) angling the two fibres with respect to one another b) angle polishing the tips of the fibres.

As well as the difficulty of fabricating such probes accurately and consistently, the efficiency of angle-polished probes varies more rapidly with changes in sample refractive index than simple parallel-fibre probes. Also, when angled-optical-fibre probes are coupled with capillary cells (as will be discussed in chapter 5), because the emission and collection cones have separate axes, it may be impossible to confine the light within both the emission and collection cones. No results from angled or angle-polished fibre probes are presented in this work.

4.2. Parallel-Fibre Probe Model

In this section a mathematical expression for the intensity of the light collected by a dual-fibre, parallel, flat-tipped fibre probe that is immersed in a scattering analyte is developed. By setting the fibre separation to zero, the model also describes a single-fibre probe. The model is compared to other models from the literature[74][75][76][77][78], and shown to be a more complete and more accurate representation of experimental measurements.

The system modelled is shown in figure 4.4: parallel, flat-tipped, step-index fibres are aligned with their end faces lying in the plane z=0, and separated by a distance D between the fibre axes. The collection fibre has core radius r_c and numerical aperture NA_c; the emission fibre has radius r_m and numerical aperture NA_m. The region of space where z>0 is filled with an absorbing and scattering sample of refractive index n. By setting the fibre separation to 0, and making the fibre parameters for collection and emission fibres identical, the model also describes a single-fibre probe.

The model is based on ray optics, rather than on fibre modes, which is appropriate for the large-core, multimode fibres under consideration. Scattering is assumed to be isotropic, which is valid for fluorescent light, and within 5% for Raman scattered light as long as $\theta_{NAm}+\theta_{NAc}<13^o$ ($\theta_{NAm}+\theta_{NAc}$ are as marked on figure 4.4, where *eg* θ_{NAm}=asin(NA_m/n)). Fresnel reflection at the probe tip has been ignored, but for a probe immersed in water this only amounts to a small fraction of a percent. There is also a small approximation involved in the inclusion of the analyte absorbance at the emission wavelength, α_m, which introduces less than 1% error as long as the product $\alpha_m r_0$<0.01.

It should be noted that this theory takes no account of leaky fibre modes. In the context of this model, leaky modes comprise rays which do not pass through the fibre axis, which make an angle to it greater than that required for total internal refection, but which, because of the cylindrical shape of the fibre, meet the core cladding interface beyond the critical angle, and are therefore reflected[79]. Such rays are not fully guided, but can propagate over thousands of metres. This means that the model is strictly valid only when the collection fibre length is greater than a few kilometres, or is a short length of graded-index-core fibre, where the leaky modes increase the effective fibre NA to that of a step index fibre with no leaky modes. Only light originating just outside the collection cone, or in regions 1, 3, or 4 in figure 4.4 can excite leaky modes. The relative contribution of leaky modes to the light collected is seen to be small when this model is compared to experimental data (section 4.3).

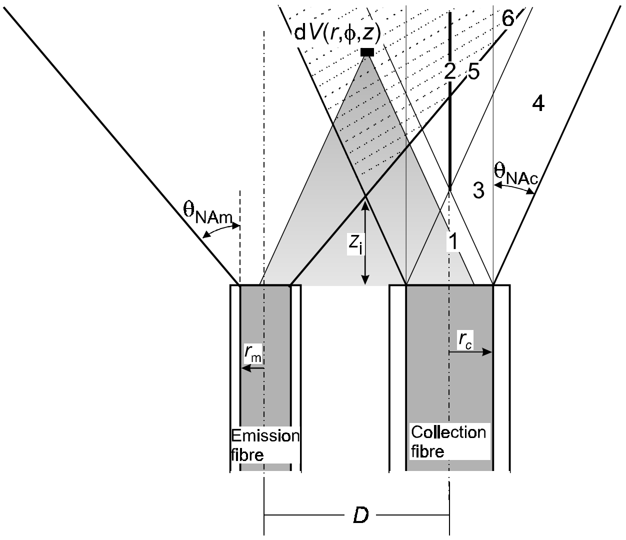

Figure 4.4 The probe comprises parallel, step-index, multimode fibres. Light from the emission fibre, of radius r_m, forms a cone of light having an angle θ_{NAm} to the fibre axis (the emission cone). Light scattered within a cone of angle θ_{NAc} incident on to the core of the collection fibre (the collection cone) will be transmitted by the collection fibre, provided that it is within the collection fibre numerical aperture, and not absorbed before reaching the collection fibre.

Because only light originating in the intersection between the emission and the collection cones is collected, shown hatched in figure 4.4, there exists a distance z_i before which no light is collected, where z_i is given by equation 4.1.

$$z_i = \frac{D - r_c - r_m}{\tan(\theta_{NAc}) + \tan(\theta_{NAm})} \tag{4.1}$$

The two quantities that are of interest when evaluating the performance of an optical-fibre probe are the collected light intensity per unit length from a plane of differential thickness dz parallel to the fibre tips, d$P(z)$, and the integral of d$P(z)$ from the fibre tips to a depth z in the scattering medium, $P(z)$. Both of these quantities are normalised with respect to the emission intensity, and the scatterer number density and scattering cross section. The first of these, d$P(z)$, is termed the *differential efficiency* of the probe; it can be used to find the region from which most of the scattered light is collected (at the maximum of the differential efficiency, where d$P(z)$=0). If a planar sample is under investigation the optimum separation between probe and sample is at the value of z where d$P(z)$=0. The second quantity, $P(z)$, is referred to as the *efficiency* of the probe; it is the total intensity of light collected from the analyte between the fibre tip and a depth z.

The rest of this section (4.2) describes the details of the numerical integrations made to calculate dP(z) and P(z). Any reader who is only interested in the results of those integrations may move ahead to section 4.3, where the mathematical predictions are compared with experimentally measured values.

Three coordinate systems are used in the model: two circular-cylindrical sets, (r, ϕ, z) and (r', ϕ', z'), which share the cylindrical axes of the emission fibre and collection fibre respectively, and a spherical-polar set, (ρ, θ, ϕ), centred on the differential scattering volume dV(r, ϕ, z). The intensity of light which is scattered from a differential volume element dV(r, ϕ, z), and then accepted by the collection fibre, is dP_{dV}(r, ϕ, z), given by equation 4.2.

$$\mathrm{d}P_{\mathrm{dV}}(r,\phi,z)=E_{\mathrm{T}}E(r,z)\cdot n_{\sigma}\cdot\sigma\cdot T_{\mathrm{c}}(r,\phi,z)\cdot\Omega(r,\phi,z)\cdot\mathrm{d}V(r,\phi) \quad \textbf{(4.2)}$$

E_{T} is the total intensity of the light emitted from the probe tip; E(r, z) is the normalised irradiance of that light in the plane z, across the collection cone, which is symmetric with respect to ϕ, and includes any absorption at the incident wavelength; n_{σ} is the number density of scatterers per unit volume; σ is the scattering cross section of each scatterer; T_{c}(r, ϕ, z) is the average transmission at the collected wavelength between dV(r, ϕ, z) and the collection fibre tip; Ω(r, ϕ, z) is the collection solid angle from the scattering volume, *ie* the solid angle within which scattered photons will be accepted by the collection fibre, (which does not necessarily encompass the whole of the collection fibre surface); and dV(r, ϕ) is the volume of the cylinder of differential thickness dz from which the scattering originates. More complete expressions for each of these quantities will be given shortly.

To find dP(z), dP_{dv}(r, ϕ, z) must be normalised (by dividing out the constants n_{σ}, σ, and E_{T}), and integrated over the z plane. Because light is only scattered from within the emission cone, and only collected from the collection cone, the integral need only be made within the overlap region between these two cones. If $z<z_{\mathrm{i}}$ (from equation 4.1), then there is no overlap, and dP(z) is zero; when $z>z_{\mathrm{i}}$, the overlap region falls into one of the classes illustrated in figure 4.5, depending on the emission and collection fibre core radii and numerical apertures, the fibre spacing, and the distance z from the plane z to the fibre tips. The circular cross section through the emission cone has a radius r_{NAm}(z), and through the collection cone the radius is r_{NAc}(z), both as given in equation 4.3.

$$\begin{aligned} r_{\mathrm{NAm}} &= r_{\mathrm{m}}+z\cdot\tan(\theta_{\mathrm{NAm}}) \\ r_{\mathrm{NAc}} &= r_{\mathrm{c}}+z\cdot\tan(\theta_{\mathrm{NAc}}) \end{aligned} \quad \textbf{(4.3)}$$

The areas of integration on these planes, *ie* the overlap of emission and collection cones, are shown shaded in figure 4.5. Previous workers have either performed the integration of $dP_{dv}(r, \phi, z)$ over the whole of the collection cone[74], using a step function to discriminate between the regions within and without the emission cone, or have defined the boundaries and performed the integral in rectangular Cartesian coordinates[75]. The first method precludes the use of efficient numerical algorithms, and neither method makes full use of the symmetry of the system to reduce the calculation time, particularly in the case of a single-fibre probe, where the problem is fully symmetric about the *z* axis.

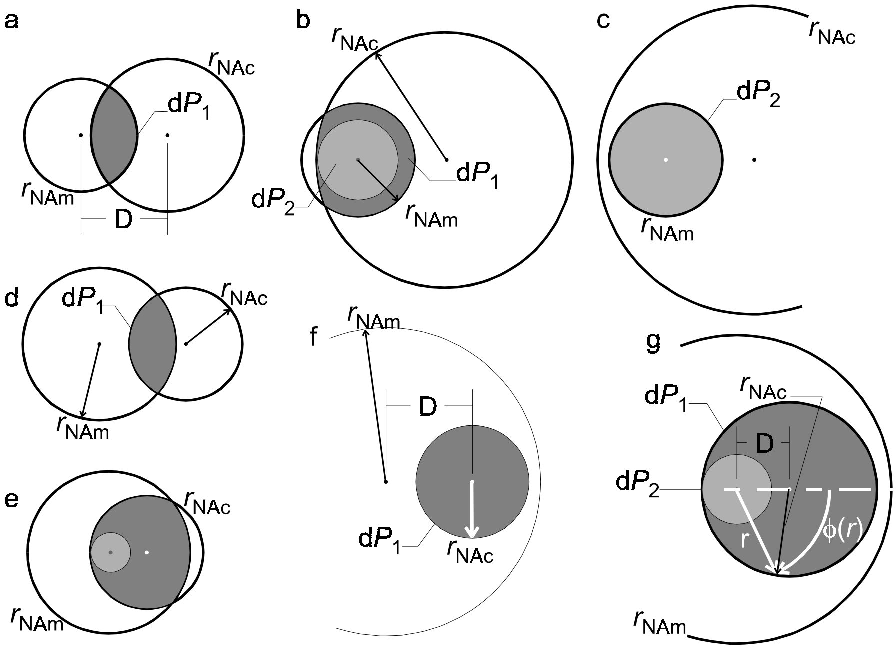

Figure 4.5 Planes of constant *z* through the region of overlap between the emission cone and the collection cone: the shaded regions represent the area of the integration to find $dP(z)$, in certain cases subdivided into dP_1 and dP_2, to simplify the integration. The integrations in each case are over the variables r and ϕ (as marked in part g). The cases a to g are descried mathematically in table 4.1.

Depending on the overlap between the collection and emission cones, the limits of the integration can most easily be defined if the integration is found as the sum of two parts, $dP_1 + dP_2$. These integrals are given in equation 4.4, and are shown shaded in figure 4.5.

$$dP_1(z) = 2\int_{r_1(z)}^{r_2(z)} \int_{0}^{\phi(r,z)} dP_{dV}(r,\phi,z)\cdot r\,d\phi\,dr\,dz$$

$$dP_2(z) = 2\int_{0}^{r_1(z)} \int_{0}^{\pi} dP_{dV}(r,\phi,z)\cdot r\,d\phi\,dr\,dz \qquad \textbf{(4.4)}$$

In the equations of 4.4, the differential element dV has been described in circular-cylindrical coordinates by the product rdϕdrdz. The element dP_{dV} is integrated over ϕ and then r; there is no integration over dz at this stage. The factor 2 is introduced because the inner integral, which is symmetrical about ϕ=0, is only over half of the overlap region (from 0 to π, instead of from -π to π). The function $\phi(r,z)$, which is the upper limit of ϕ in the integral dP_1, is found by applying the cosine rule[80] to the triangle formed by D, $r_{\mathrm{NAc}}(z)$, and r (see figure 4.5g), and is given in equation 4.5.

$$\phi(r,z) = \mathrm{acos}\left(\frac{D^2 + r^2 - r_{\mathrm{NAc}}^2}{2Dr}\right) \tag{4.5}$$

For the case of a single-fibre probe, where D=0, then d$P_{\mathrm{dV}}(r, \phi, z)$ is fully symmetric with ϕ, and only dP_2 of equation 4.4 is required to compute the integral, so the inner integral may be replaced by the constant factor π. (For the double fibre case this symmetry is broken by the factors $\Omega(r, \phi, z)$ and $T_c(r, \phi, z)$ in d$P_{\mathrm{dV}}(r, \phi, z)$). The other limits of the integrals, given in table 4.1, are determined by the overlap between the emission and collection cones, as shown on figure 4.5.

Table 4.1 The limits of equation 4.4, for the cases illustrated in figure 4.5.

Case	Condition	Integral	Limits
a	$r_{\mathrm{NAc}} \le D$ & $r_{\mathrm{NAm}} \le D + r_{\mathrm{NAc}}$ & $r_{\mathrm{NAc}} \ge r_{\mathrm{NAm}}$	dP_1	$r_1 = D - r_c$, $r_2 = r_{\mathrm{NAm}}$
b	$r_{\mathrm{NAc}} > D$ & $r_{\mathrm{NAc}} < D + r_{\mathrm{NAm}}$ & $r_{\mathrm{NAc}} \ge r_{\mathrm{NAm}}$	dP_1 + dP_2	$r_1 = r_{\mathrm{NAc}} - D$, $r_2 = r_{\mathrm{NAm}}$
c	$r_{\mathrm{NAc}} \ge r_{\mathrm{NAm}} + D$	dP_2	$r_1 = r_{\mathrm{NAm}}$
d	$r_{\mathrm{NAc}} \le D$ & $r_{\mathrm{NAm}} \le D + r_{\mathrm{NAc}}$ & $r_{\mathrm{NAc}} < r_{\mathrm{NAm}}$	dP_1	$r_1 = D - r_c$, $r_2 = r_{\mathrm{NAm}}$
e	$r_{\mathrm{NAc}} > D$ & $r_{\mathrm{NAm}} < D + r_{\mathrm{NAc}}$ & $r_{\mathrm{NAc}} < r_{\mathrm{NAm}}$	dP_1 + dP_2	$r_1 = r_{\mathrm{NAc}} - D$, $r_2 = r_{\mathrm{NAm}}$
f	$r_{\mathrm{NAm}} > D + r_{\mathrm{NAc}}$ & $r_{\mathrm{NAc}} \le D$ & $r_{\mathrm{NAc}} < r_{\mathrm{NAm}}$	dP_1	$r_1 = D - r_{\mathrm{NAc}}$, $r_2 = D + r_{\mathrm{NAc}}$
g	$r_{\mathrm{NAm}} > D + r_{\mathrm{NAc}}$ & $r_{\mathrm{NAc}} > D$ & $r_{\mathrm{NAc}} < r_{\mathrm{NAm}}$	dP_1 + dP_2	$r_1 = r_c - D$, $r_2 = r_c + D$

The exact form of the function $E(r, z)$, the normalised irradiance across the emission cone, has been shown by Plaza[74] to be of little significance to the result of the integrations of equation 4.4, and other workers[76] have taken it as constant across the emission cone. In this work, exact expressions have been used for all other quantities, and there is no additional penalty in using an accurate expression for $E(r, z)$. However, two small approximations are made in the expression used to describe $E(r, z)$ in equation 4.2: an approximation for the exact form of the irradiance distribution, and for the absorption between the fibre tip and the scattering volume $\mathrm{d}V(r, \phi, z)$.

It can been shown by a simple ray analysis that, if light is coupled into an optical fibre through a small spot at the centre of the end-face, then the power within the core, and therefore *at the probe tip*, follows a $1/r$ distribution[81]. Away from the fibre tip the intensity distribution depends on the angular distribution at the input of the fibre, but is distorted by any scattering and mode conversion within the fibre, and any sample absorption. Equation 4.6 has been chosen to describe the normalised irradiance when the fibre is illuminated by a diode laser source. This equation is compared with the experimentally measured irradiance from an optical fibre later, in figure 4.7.

$$E(r,z)=\frac{1}{N}\cdot\frac{w}{\pi\left(r_{\mathrm{m}}+z\frac{NA_{\mathrm{m}}}{n}\right)^{2}}\cdot\exp\left(-w\left(\frac{r}{r_{\mathrm{m}}+z\frac{NA_{\mathrm{m}}}{n}}\right)^{2}-\alpha_{\mathrm{m}}\sqrt{r^{2}+z^{2}}\right) \qquad \textbf{(4.6)}$$

$$N=\int_0^r\int_0^{2\pi}\frac{w}{\pi r_m^2}\exp\left(w(r/r_{\mathrm{m}})^2\right)r\,\mathrm{d}\phi\,\mathrm{d}r=1-\exp(-w)$$

In equation 4.6 the factor N scales the function so that at, in the absence of absorption (or at the fibre tip), the total power across the emission cone is 1; w (termed the *beam width parameter* here) determines the width of the Gaussian. Sample absorption at the wavelength emitted from the probe is accounted for by the term in the exponential, α_{m}, the sample absorbance at the incident wavelength. This assumes that all light originates from the centre of the fibre, which is obviously false; however, it is a good approximation more than a few fibre radii from the tip, and the pathlength is in error by at most $r_0\alpha_{\mathrm{m}}$, when z=0. The error in $E(r, z)$ associated with this approximation will therefore be well below 1% as long as the product $r_0\alpha_{\mathrm{m}}<0.01$.

The two further non-constant parameters in $\mathrm{d}P_{\mathrm{dv}}(r, \phi, z)$, $T_{\mathrm{c}}(r, \phi, z)$ and $\Omega(r, \phi, z)$, are both themselves integrals, expressed in the spherical polar coordinates centred on $\mathrm{d}V(r, \phi, z)$. For computational convenience it is best to combine these quantities into the single expression $\Omega_{\mathrm{Tc}}(r, \phi, z)$. The integral is within a similar boundary to that of equation 4.4, in this case the intersection between the collection fibre core and the cross section at z=0 of a cone of light of half-cone angle θ_{NAc} with its apex at the scattering element d*V*. Again, as in equation 4.4, the integral of equation 4.7 is given in two parts.

$$\Omega_{Tc1}(r',z')=2\int_{\theta_1}^{\theta_2}\int_{0}^{\phi(\theta)}\exp\left(\alpha_c z\tan(\theta)\right)\sin(\theta)\mathrm{d}\theta\mathrm{d}\phi=2\int_{\theta_1}^{\theta_2}\phi(\theta)\exp\left(\alpha_c z\tan(\theta)\right)\sin(\theta)\mathrm{d}\theta$$

$$\Omega_{Tc2}(r',z')=2\int_{0}^{\theta_1}\int_{0}^{\pi}\exp\left(\alpha_c z\tan(\theta)\right)\sin(\theta)\mathrm{d}\theta\mathrm{d}\phi=2\pi\int_{0}^{\theta_1}\exp\left(\alpha_c z\tan(\theta)\right)\sin(\theta)\mathrm{d}\theta\mathrm{d}\phi \qquad \textbf{(4.7)}$$

$$\phi(\theta)=\mathrm{acos}\left(\frac{(z'\tan(\theta))^2+(r')^2-r_c}{2z'\tan(\theta)\cdot r'}\right)$$

Table 4.2 The limits for the integrations of equation 4.7: the solid angle is limited by the numerical aperture of the collection fibre, or the physical size of the fibre, or both, depending on the position of the scattering volume d$V(r, \phi\ z)$ in the collection cone. The parts of equation 4.7 required for each position relative to the collection fibre, and the limits of the integration, are given in this table. The region numbers are those marked in figure 4.4, and refer to the position of the scattering volume d$V(r, \phi\ z)$.

Region	Inequality	Integral	Limits
Outside	$r'<r'_{NAc}+r_c$	None	Not applicable
1	$r'+r'_{NAc}\leq r_c$	Ω_{Tm2}	$\theta_1=\theta_{NAc}$
2	$r'=0$ & $r'_{NA}>r_c$	Ω_{Tm2}	$\theta_1=\mathrm{atan}(r_c/z')$
3	$r'>r_c$ & $r'+r'_{NAc}>r_c$ & $r'>r'_{NAc}-r_c$	$\Omega_{Tm1}+\Omega_{Tm2}$	$\theta_1=\mathrm{atan}(r_c-r'/z')$, $\theta_2=\theta_{NAc}$
4	$r'\leq r'_{NAc}+r_c$ & $r'\geq r_c$ & $r'\geq r'_{NAc}-r_c$ & $z'>0$	Ω_{Tm1}	$\theta_1=\mathrm{atan}(r'-r_c/z')$, $\theta_2=\theta_{NAc}$
5	$r'>0$ & $r'<r_c$ & $r'\leq r_{NAc}-r_c$	$\Omega_{Tm1}+\Omega_{Tm2}$	$\theta_1=\mathrm{atan}(r_c-r'/z')$, $\theta_2=\mathrm{atan}(r_c+r'/z')$
6	$r'\geq r'_{NAc}$ & $r'<r'_{NAc}-r_c$	Ω_{Tm1}	$\theta_1=\mathrm{atan}(r_c-r'/z')$, $\theta_2=\mathrm{atan}(r_c+r'/z')$

For scattering volumes *at* the probe tip the collection *NA* is limited by the *NA* of the fibre. Away from the fibre tip, the solid angle is determined by the boundary of the integration (as defined by the limits listed in table 4.2): close to the fibre tip, this may be set by the fibre *NA*, or by the fibre *NA* on one side and the physical edge of the collection fibre on the other. Further from the collection fibre, the boundary of the integration is determined only by the physical size of the collection fibre core, and then the approximation for the collection solid angle and sample transmission of equation 4.8 may be made, where r_c is the radius of the collection fibre core.

$$\Omega_{Tc}(z)=\frac{\pi r_c^2}{z^2}\cdot\exp(-\alpha_c z) \qquad \textbf{(4.8)}$$

Although this approximation has not been used in any of the calculations presented here, it is conceptually useful, as the fall of Ω_{Tc} with increasing distance *z* is explicit. It is this rapid fall in collection solid angle that the light-guiding sample cells of chapter 5 attempt to counter, thus greatly enhancing the collection efficiency.

The coordinates *r*' and *z*' in equation 4.7 and table 4.2 describe the position of the scattering element d*V* with respect to the circular-cylindrical coordinates centred on the collection fibre. These coordinates are related to circular cylindrical coordinates centred on the emission fibre tip (*ie* the coordinates of d*V*(*r*, ϕ, *z*)) by the transforms of equation 4.9. These expressions should be used as the arguments to equation 4.7 in equation 4.2. The distance r'_{NAc}=ztan(θ_{NAc}), referred to in table 4.7, is the radius of the cone of angle θ_{NAc} from the scattering element d*V*(*r*, ϕ, *z*) at the collection fibre tip (*ie* the cone of light that is within the collection fibre *NA*).

$$z' = z$$
$$r' = \sqrt{\left((D - r\cos(\phi))^2 + (r\sin(\phi))^2\right)} \qquad \textbf{(4.9)}$$

The expressions given in equations 4.2 to 4.7 have been evaluated as numerical integrals using the Mathcad 6 Plus software from Adept Scientific, UK.

4.3. Theoretical Predictions and Experimental comparison

4.3.1. Measurement of the irradiance across the emission cone, *E*(*r*, *z*)

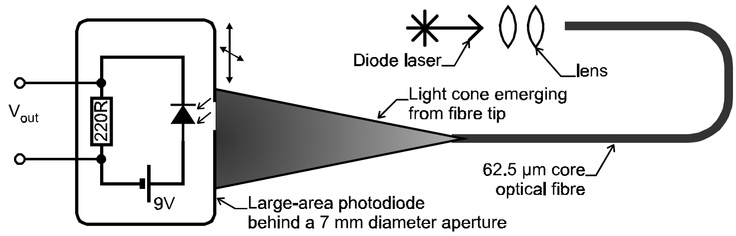

Figure 4.6 A schematic of the scanned-detector arrangement used to measure the irradiance across a plane normal to the axis of the emission cone.

The expression for the normalised irradiance across the emission cone *E*(*r*, *z*), the normalised collection efficiency per metre d*P*(*z*), and the total light collection efficiency (from a depth *z*) *P*(*z*), have each been compared with measured values. To measure the irradiance across the emission cone the arrangement shown in figure 4.6 was used. A 1 m long section of 62.5 µm core, step index, optical fibre was cleaved at each end. Light from a CorkOpt laser diode was coupled into it via the arrangement described in section 3.1, figure 3.4, using an FC-type bare fibre adaptor. A large area silicon photodiode, mounted behind a 7 mm diameter aperture was scanned perpendicular to the emission cone axis at a distance of 184 mm from the fibre tip. The detector was moved in 12.5 mm steps along both orthogonal axes.

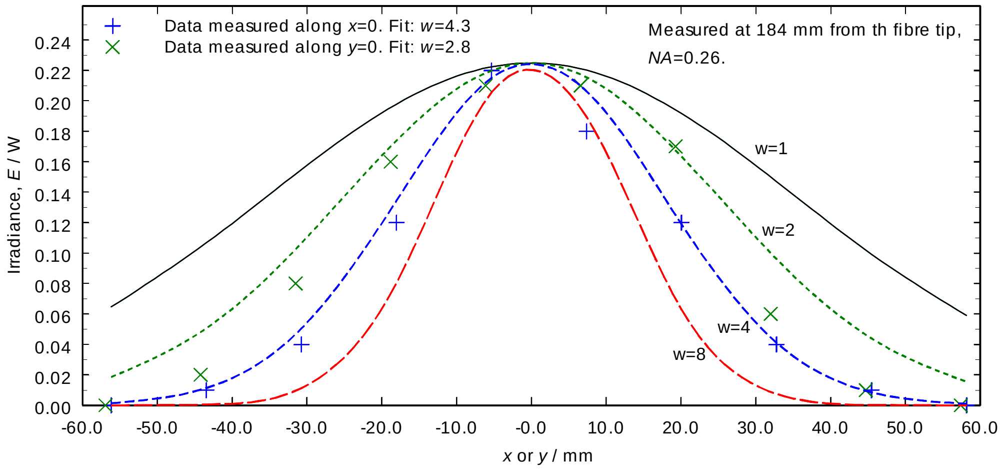

Figure 4.7 The intensity across the output from a pigtailed diode laser. Measurement noise is largely due to optical interference between the modes of propagation through the 50 µm core fibre. The prediction of equation 4.6 for the cases *w*=1, 2, 4, and 8 is also plotted.

Although to the naked eye the spot appeared circular, equation 4.6 was fitted to the measured data and two values of *w*, 4.3 and 2.8, were found for the orthogonal data sets. The measured data is plotted against equation 4.6 with different values of *w* in figure 4.7. In the use of equation 4.6 in this chapter, a value of *w*=4 has been used unless stated otherwise. As is shown in figure 4.16 (section 4.4), changing this value by ±2 makes little difference to the functions d$P(z)$ and $P(z)$.

4.3.2. Measurement of differential fibre probe collection efficiency, d*P*(*z*)

Two series of experiments were made to measure d$P(z)$ and $P(z)$; the fibre separation D, the solution absorbance α_m and α_c, and the refractive index n of the scattering medium were independently varied. In the first of the experiments d$P(z)$ was measured directly, by measuring the light scattered and collected from a sheet of PTFE; in the second $P(z)$ was measured from a depth z of a fluorescent solution.

To ensure that the fibre separation D was accurately controlled, 22 fibres with 125 µm outer diameter were permanently bonded into a 3 mm tall, 140 µm wide, aluminium slit, and polished to a 1 µm finish, by the same method as described in chapter 3. One end of the slit was defined as the top, and the fibres numbered sequentially from 1 to 22. Optical fibres, numbers 2, 3, 6, and 15, were used as collection fibres in these experiments, fibre number 1 being the emission fibre in each case. The slit was photographed, and the distances between each fibre centre to the centre of fibre number 1 were measured from this, as illustrated in figure 4.8. (Measured dimensions are ±5 µm.)

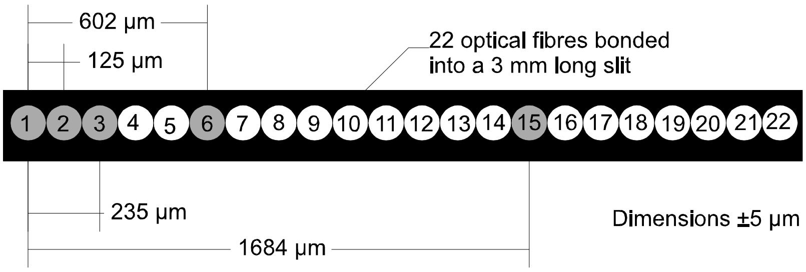

Figure 4.8 22 fibres were bonded into a slit and polished to a 1 µm finish. The measured axial separations *D* between the emission fibre (marked 1 in this figure) and the collection fibres (marked 2, 3, 6, and 15) were 125 µm, 235 µm, 602 µm, and 1684 µm respectively. The slit was positioned vertically in the experiments.

In each experiment the slit was held vertical by a crocodile clip and mounted on a thumb-screw-operated translation stage, which had a Vernier scale marked with minor divisions of 0.2 mm. The maximum translation was 19 mm, and the zero position was obtained by gently butting the end of the slit against the target using the thumb screw. The random error in the distances read from the Vernier scale is estimated as ±0.05 mm; systematic error is discussed with each experiment.

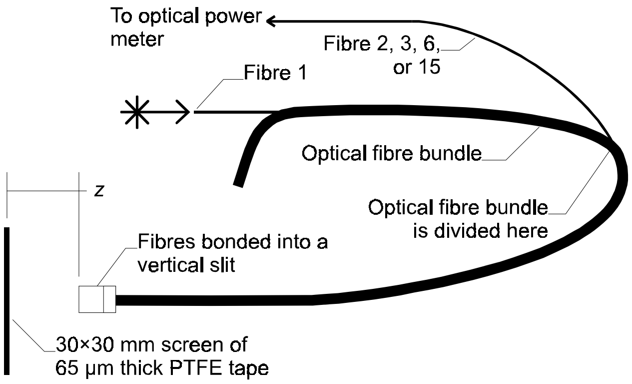

Figure 4.9 A schematic of the arrangement used to measure d$P(z)$ directly from the elastic scattering from a screen made from PTFE tape.

The arrangement of figure 4.9 was used to measure d$P(z)$ directly. A screen made of PTFE tape was mounted perpendicular to the array of fibres, and the thumb screw of the translation stage was used to butt the fibre against the screen. By observing the screen from behind, the systematic error in the position of the fibres with respect to the screen was estimated as ±0.05 mm. The thickness of the PTFE tape was measured three times with a micrometer, and a value of 65±5 µm was obtained.

All the fibre ends were cleaved, fibre 1 was inserted into a bare fibre adapter, and 11 mW of light was coupled into it from the 676 nm CorkOpt laser diode, using the arrangement of chapter 3, figure 3.4. The light scattered from the screen into the collection fibre was measured with an optical power meter from Newport (model 835 with detector head model 818). An offset of 57 nW in the measured intensity has been subtracted from the measured power, no adjustment has been made to the *z* data. Making the measurement in air (refractive index *n*=1) produces larger emission and collection cones than when the probe is immersed in a liquid analyte; the cone angle of 15.5° simulates a fibre of *NA*=0.36 immersed in water.

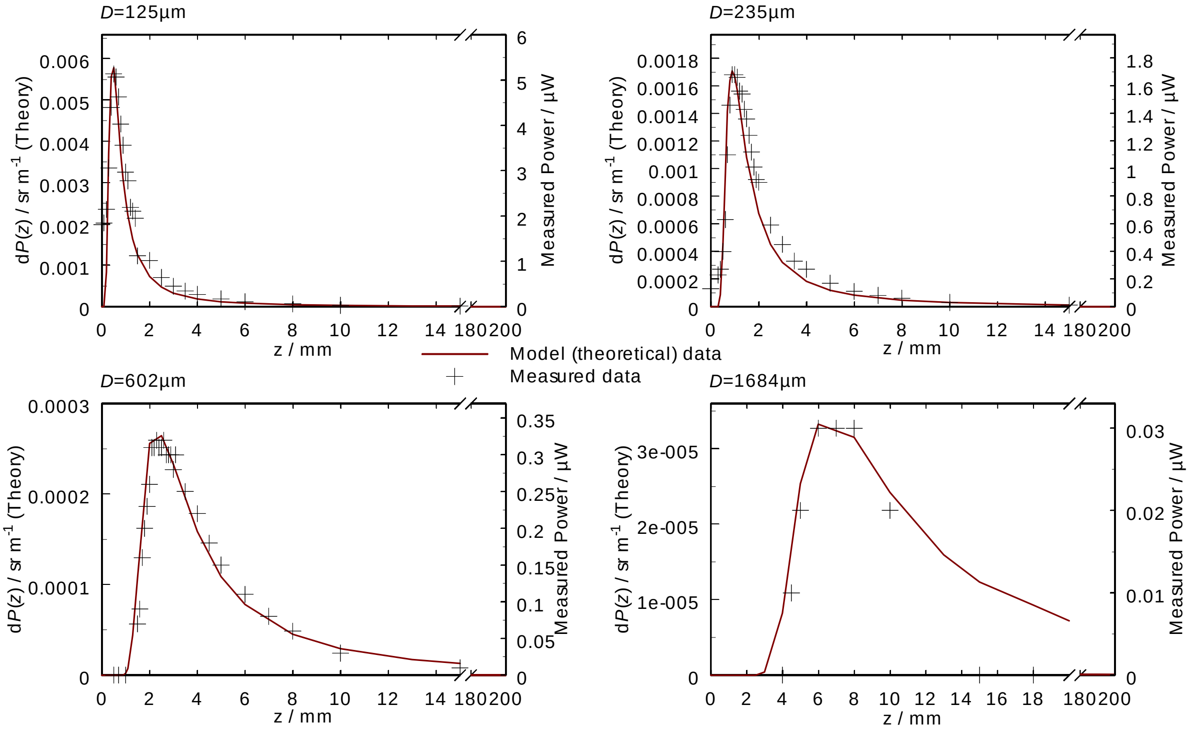

Figure 4.10 The calculated differential collection efficiency d*P* (*z*) (left hand axis) is plotted against the measured value (right hand axis), measured using the arrangement of figure 4.9.

The measured data is plotted against the calculated differential collection efficiency in figure 4.10. The non-zero values of the measured data at low *z*, where the collection should be zero, are due to multiple scattering across the PTFE tape. The position of the peak in d*P*(*z*) agrees exactly with the measured data, although the shape of the curve formed by the measured data is slightly broader than the predicted values, possibly due to the contribution from leaky modes excited from scattering close to the probe tip.

4.3.3. Measurement of fibre probe collection efficiency, *P*(*z*)

For the measurement of $P(z)$ the same arrangement was used to position the probe, which was immersed in an aqueous solution of the fluorescent dye Basic Blue 3, as shown in figure 4.9. The dye was supplied as a powder, labelled ‘330% Panacryl Blue 5G’ (PB5G), from Holliday Dyes and Chemicals, UK. The 330% indicates that the dye was pure, and not diluted with any binder compounds. A 600 mg/L ±4% aqueous solution was prepared by mixing 0.12±0.005 g of the powder into 200 mL of deionised water, measured from a 100 mL pipette. All further solutions of the dye were derived from this, using a micropipette to measure the solution into 1 L volumes of deionised water measured, from a 500 mL volumetric flask. The total error in the concentrations quoted are determined by the error in weighing the powder, ±4%, but the relative error between solutions is less than this.

The optical absorption of a 3.6 mg/L solution of the dye in a 10 mm path length cuvette was measured using a Perkin-Elmer Lambda 9 spectrophotometer, with a cuvette of deionised water in the reference beam. The total absorbance of the PB5G solutions was calculated using literature values for the absorption of pure water[82][83]. The absorbance of each solution is quoted with each of the presented measurements.

The fibre probe was mounted perpendicular to the polished face of a 20 mm wide and 90 mm long FK5 glass block, which was immersed in the solution, shown in figure 4.9. The glass FK5 was used because of its low refractive index[84] of n_r=1.48; the Fresnel reflection between the glass and the aqueous solution is below 0.3%. The position where z=0 was again determined by gently butting the probe against the glass substrate using the thumb screw, but due to the greater difficulty in observing the probe, a systematic error of 0.2 mm was estimated for z in this case.

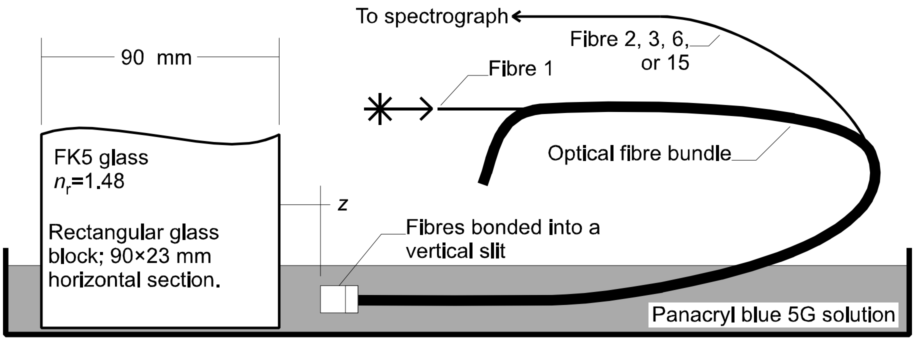

Figure 4.11 A schematic of the arrangement used to measure $P(z)$.

The fluorescent spectra from solutions of four different concentrations (*ie* different sample absorption), and with the four collection fibres, were taken by positioning the collection fibre end at the input of the grating spectrograph using a Melles Griot fibre chuck mounted on an XYZ translation stage. The position of the fibre tip with respect to the input had been optimised by pointing the slit at the room lights, and adjusting the position of the fibre tip until the maximum resolution and intensity was achieved. From the measurement of $P(z)$, the gradient of the line between each pair of measured points has been taken, which gives $\mathrm{d}P(z)$. No gradients have been measured for the case $\alpha_m=0.88\ \mathrm{m}^{-1}$ $\alpha_c=2.4\ \mathrm{m}^{-1}$, as the data is of too poor quality.

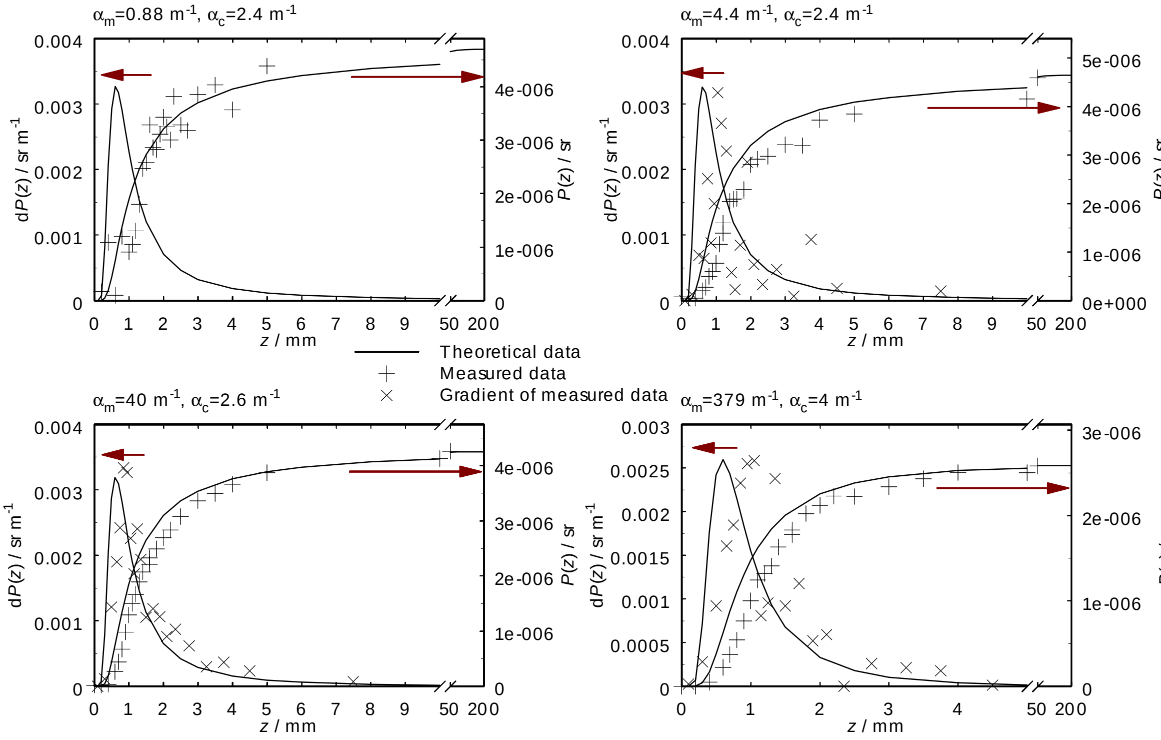

Figure 4.12 The calculated differential collection efficiency d*P* (*z*) (left hand axis) and collection efficiency P(z) (right hand axis) are plotted against the measured data (arbitrary scaling), measured from a depth *z* of aqueous Basic Blue 3 dye. The fibre spacing in each case is 125 µm, the sample absorbances are as noted in the figure.

For the constant fibre separation case, P(*z*) was measured in samples of total absorbance $(\alpha_m+\alpha_c)$ 3.3 cm^{-1} to 383 cm^{-1}. A systematic offset in *z* is apparent between the predicted and the measured values of $P(z)$ and $\mathrm{d}P(z)$, consistent with the estimated systematic error. The calculated differential collection efficiency $\mathrm{d}P(z)$ in the case of the highest absorption solution ($\alpha_m=379\ \mathrm{m}^{-1}$) appears narrower than that derived from the measured data. This is thought to be due to increased collection from close to the fibre tip, due to multiple scattering in this high concentration solution, and the increased significance of leaky fibre modes, excited by emission from close to the to the probe tip in high absorbance solutions. It is apparent from figure 4.12 that absorption effects are negligible as long as $z_{max}\cdot(\alpha_c+\alpha_m)<100$, where z_{max} is the position of the maximum in $\mathrm{d}P(z)$.

The measured data in figure 4.13, which shows the variation of *P*(*z*) and d*P*(*z*) with *D*, in identical solutions, show similar agreement with the calculated d*P*(*z*) and *P*(*z*) curves.

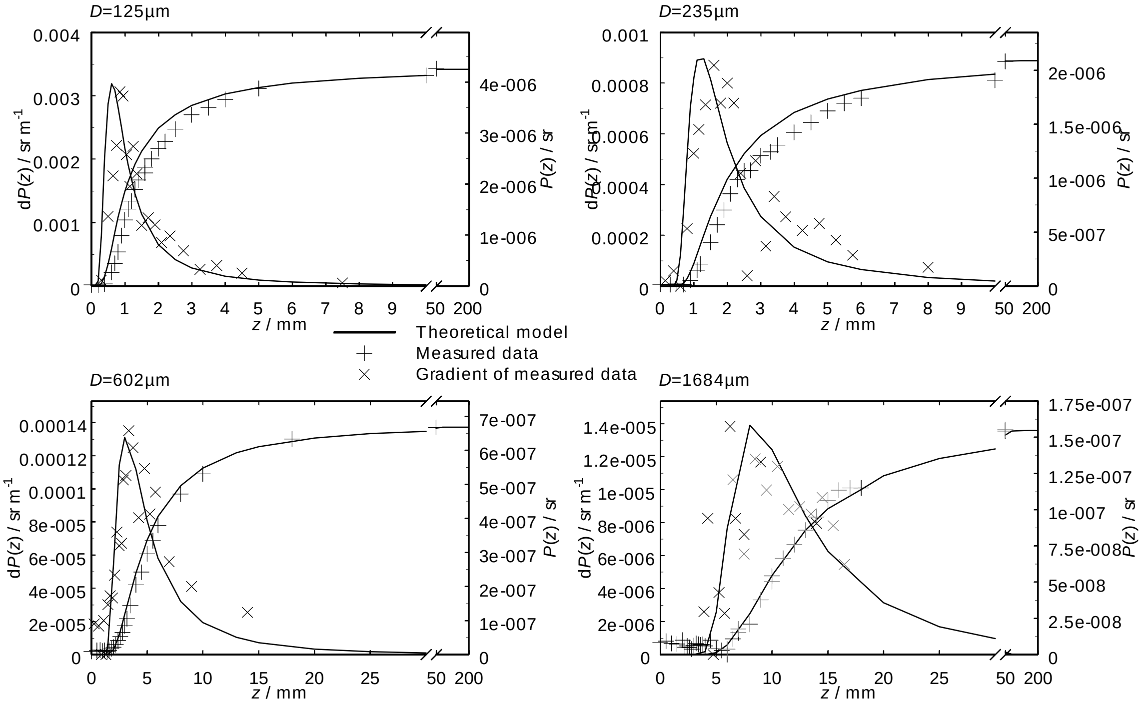

Figure 4.13 The calculated differential collection efficiency d*P* (*z*) (left hand axis) and collection efficiency *P*(*z*) (right hand axis) are plotted against the measured data (arbitrary scaling), measured from a depth *z* of aqueous Basic Blue 3 dye. The solution absorbance at the emission and collection wavelength respectively is α_m= 40 m^{-1} and α_c=2.6 m^{-1}, the fibre spacings *D* are as noted in the figure. Two independently measured data sets are plotted for the case *D*=1684 µm.

The data presented so far have been normalised, and scaled to arbitrary axes. As a further check on the validity of the equations derived in this chapter, an absolute power measurement was made. The 1002 cm^{-1} Raman line of pure toluene was measured, and the integrated power within it compared to the model prediction, with the 1002 cm^{-1} scattering cross section taken from the literature[45].

To make this comparison, a careful measurement of the spectrum from a NIR LED was made, immediately followed by the measurement of the toluene Raman spectrum. The following measurements were made in a windowless laboratory, with all room lights, indicator bulbs, and LEDs switched off or covered.

As is described in chapter 3, a black body spectral intensity response correction is applied by the spectrograph software to each measured spectrum, but the output is in arbitrary units. In order to convert the CCD output voltage to an optical power, the integrated power in the measured feature must be compared with a measurement from a source of known power. The arrangement of figure 4.14 was used to make such a comparison.

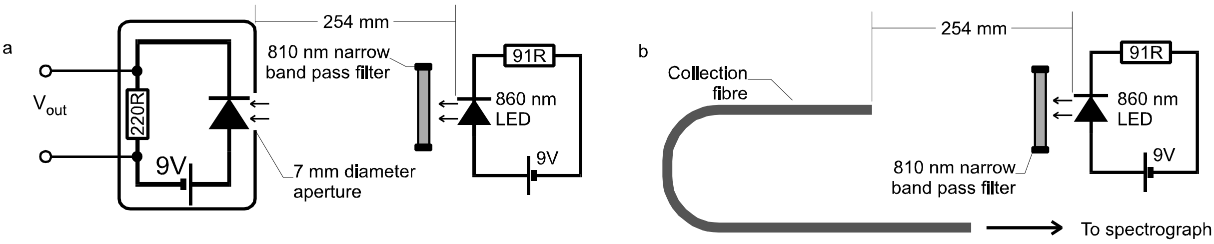

Figure 4.14 a) The irradiance across the beam from the LED was measured using the LAPD. b) An optical fibre was positioned so as to accept 9.8×10^{-13} mW of light at 810 nm.

The irradiance from a NIR LED (TEMT484, from Farnell, UK) was measured through an 810 nm narrow band pass filter (F10-810-4, CVI, USA) using the large area photodiode (described in chapter 3), positioned 254 mm from the tip of the LED. The parallel fibre array was then positioned the same distance from the LED, and the free end of fibre number 2 was positioned at the spectrograph input. The settings on the spectrograph readout software (described in chapter 3) were gain=20, and integration time=0.8 seconds (clock speed=24, start pulse length=3, integration cycles=22222). A dark reading, the average of 2400 readings with the laser switched off, was automatically subtracted from each measurement. A measurement of the LED spectrum comprising 240 readings was recorded, shown plotted against the right hand axis in figure 4.15.

Fibre number 1 was then illuminated with the CorkOpt diode laser, and 3.76 mW of light at 676 nm was measured at the probe tip using the large area photodiode. The parallel fibre array was immersed 2-3 mm below the surface of a 3 mL (30 mm deep) cuvette, full of pure toluene, and a Raman spectrum was recorded as the average of 2400 measurements, shown in figure 4.15.

The measured power of the Raman light collected from toluene agrees within 13% with the value predicted by the equations presented in this chapter.

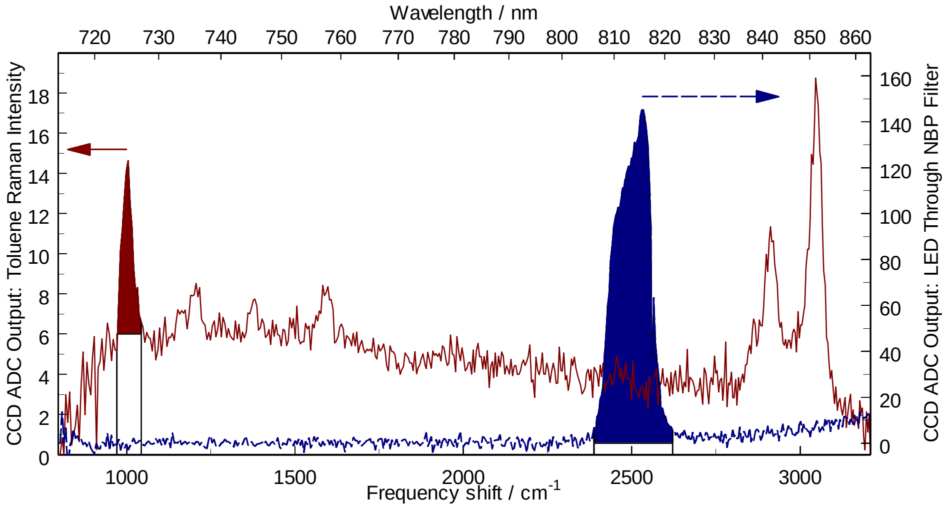

Figure 4.15 The Raman spectrum of pure toluene (plotted against the left hand axis), measured through a parallel-identical-fibre probe: $r_m=r_c=62.5$ µm, $NA_m=NA_c=0.267$, $D=125$ µm. The recorded output from the filtered LED is shown (plotted against the right hand axis). The integrated power (shown shaded) collected from the LED was 9.0×10^{-13} W, and by comparison, the integrated power in the 1002 cm^{-1} toluene Raman line that was collected (shown shaded) was 1.5×10^{-14} W, within 13% of the expected value.

4.4. Further Predictions, and Comparison with Other Work

In this section, the model developed earlier in this chapter is applied to representative arrangements of emission and collection fibres. The predictions of the model are presented as graphs of the differential quantity d$P(z)$, plotted against the left hand axis of the graphs, and the integral of this quantity from 0 to z, $P(z)$, against the right hand axis. The cases are not intended to serve as an exhaustive catalogue of possible configurations, but to illustrate the effects of the model parameters on the light collection efficiency of a parallel-fibre probe.

To make this discussion as general as possible, in this section all light collection is assumed to be from samples with zero absorbance. With zero solution absorbance, if the linear dimensions r_m, r_c, and D of a probe are all scaled by a factor F, then differential collection efficiency is transformed as d$P(z/F)$, and the collection efficiency as $F\cdot P(z/F)$.

4.4.1. The effect of the beam width parameter, *w*

In figure 4.16 the effect of the beam width parameter w is shown to be of most significance for a single-fibre probe, where the effect of increasing w (*ie* more tightly confining the emission light within the emission cone, see figure 4.7), is to increase the amount of light gathered by the probe. For the case of parallel optical-fibre probes, the effect is less marked: the total amount of light gathered is again greater for the larger values of *w*, but the maximum in d*P*(*z*) moves away from the probe tip, resulting in less light being collected from the region immediately adjacent to the probe.

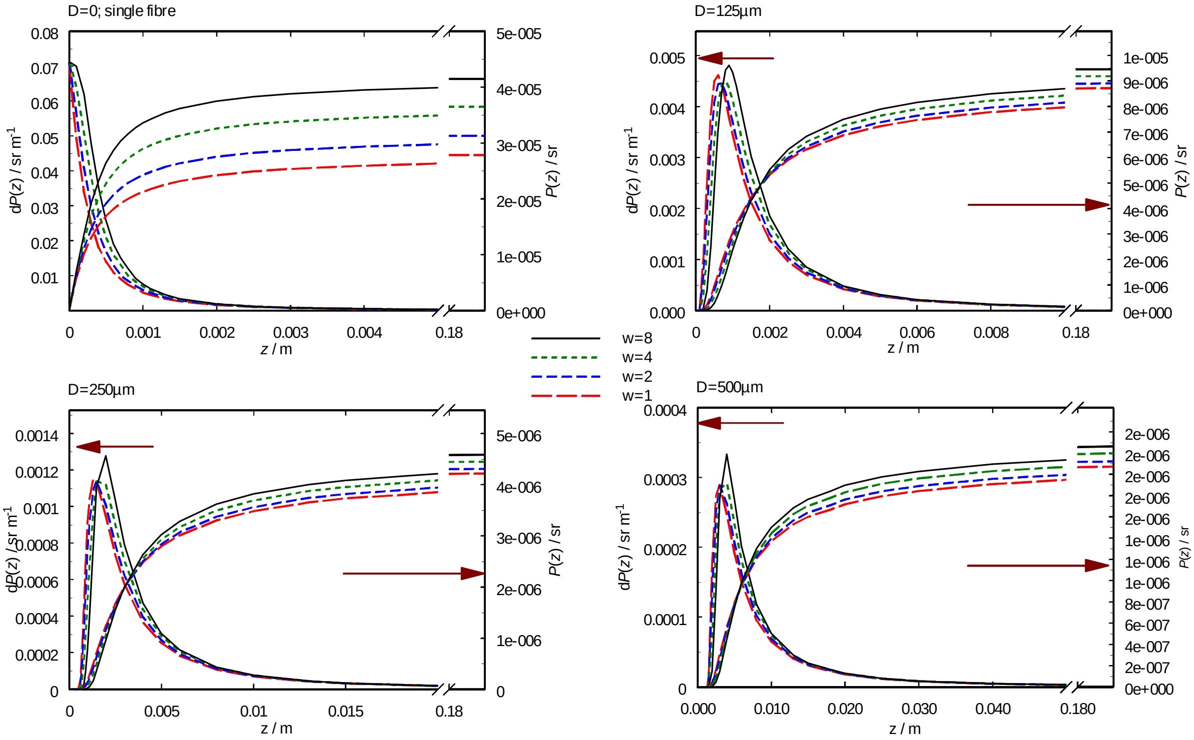

Figure 4.16 The beam width parameter *w* varied from 1 to 8 for identical-fibre probes with the given fibre separations *D*. The NA of the fibres is 0.2, the core radius is 50 µm; the solution has a refractive index *n*=1.33, and an absorbance of zero.

4.4.2. The effect of the fibre numerical aperture, *NA*

The effect of simultaneously varying the *NA* of both the emission and collection fibres is shown in figure 4.17; the light collection increases approximately in direct proportion to the fibre *NA*. In this model the distribution of light across the emission cone is scaled with the fibre *NA*, and so a smaller emission fibre *NA* has a tighter distribution of emitted light, similar to increasing the beam width parameter. The effect of changing just the collection fibre *NA* is shown in figure 4.18, along with the alternative case of varying only the emission fibre *NA*.

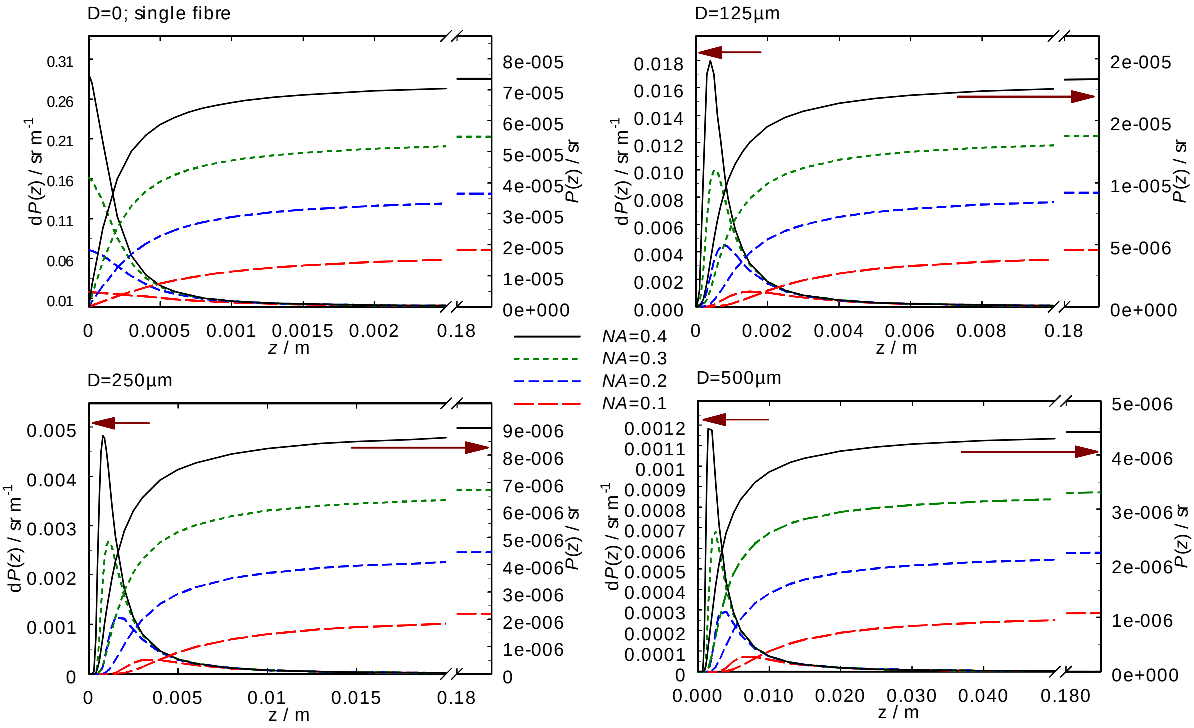

Figure 4.17 The collection and emission fibre *NA* is varied from 0.1 to 0.4 for identical-fibre probes with the given fibre separations *D*. The beam width parameter *w* is 4, the core radius is 50 µm; the solution has a refractive index *n*=1.33, and an absorbance of zero.

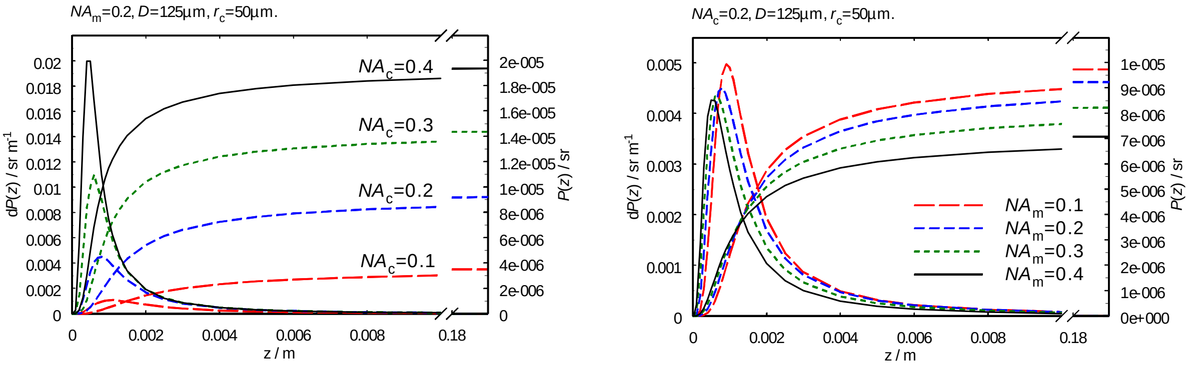

Figure 4.18 The effect of varying either the emission or collection fibre NA; the collection or emission fibre *NA* is varied from 0.1 to 0.4 for otherwise identical-fibre probes with fibre separations *D*=125 µm. The beam width parameter *w* is 4, the core radius is 50 µm; the solution has a refractive index *n*=1.33, and an absorbance of zero.

4.4.3. Many-fibre probes

The model that has been developed in this chapter is now applied to three hypothetical many-fibre probe configurations, illustrated in figure 4.19. Such probes are efficient means of delivering scattered light to a spectrometer, because the collection fibres can be arranged as a column at the spectrometer input, effectively transforming the circular cross section of the collection volume to a slit without sacrificing optical throughput.

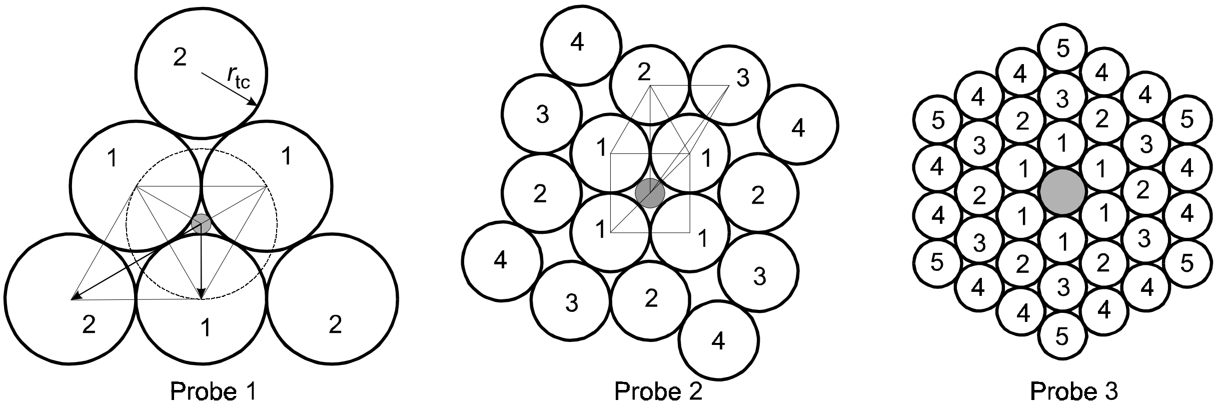

Figure 4.19 Three hypothetical many-fibre probe configurations; the single emission fibre is shown shaded, and the collection fibres are shown white, and numbered according to their distance from the centre of the emission fibre. The drawings are not to scale.

Table 4.3 The separations *D* between emission and collection fibres for probe configurations 1 to 3 in figure 4.19, where the emission fibre radius is constant at 100 µm.

Probe	Total collection fibre radius (core + cladding), r_{tc}†	Separation *D* between emission fibre and collection fibres × number of collection fibres at that separation				
		1	2	3	4	5
1	$\frac{50\mu m}{\frac{2}{\sqrt{3}}-1}=323\mu m$	$\frac{2}{\sqrt{3}}r_{tc}$ =373µm ×3	$\frac{5}{\sqrt{3}}r_{tc}$ = 933µm ×2*	Not applicable	Not applicable	Not applicable
2	$\frac{50\mu m}{(\sqrt{2}-1)}=121\mu m$	$\sqrt{2}r_{tc}$ =171µm ×4	$(1+\sqrt{3})r_{tc}$ =329µm ×4	$r_{tc}\sqrt{6-4\sqrt{2}\cos165}$ =409µm ×4	$4.11r_{tc}$ =496µm ×1*	Not applicable
3	50µm	$2r_{tc}$ =100µm ×6	$2\sqrt{3}r_{tc}$ =173µm ×6	$4r_{tc}$ =200µm ×6	$2\sqrt{7}r_{tc}$ =265µm ×12	$6r_{tc}$ =300µm ×2*

*The number of useful collection fibres is limited by the 3.2 mm detector height. †The collection fibre core radius $r_c=r_{tc}-5$ µm.

The probes considered here are designed within the constraints that the total emission fibre diameter is 100 µm (which is the smallest diameter of fibre that it is practical to work with), and that the sum of the diameters of the collection fibres is no more that 3.2 mm (to match a 1/4 inch high detector).The separations between the numbered fibres and the emission fibres are listed in table 4.3.

All the fibres in each probe are assumed to have a cladding of 5 µm thickness, a numerical aperture of 0.2, and to be immersed in an absorption free liquid of refractive index of 1.33. The beam width parameter *w*=4. Predictions for fibres of each spacing are graphed in figure 4.20. The contributions of each collection fibre in the three probes are added together, and presented in the final (bottom right) graph of figure 4.20.

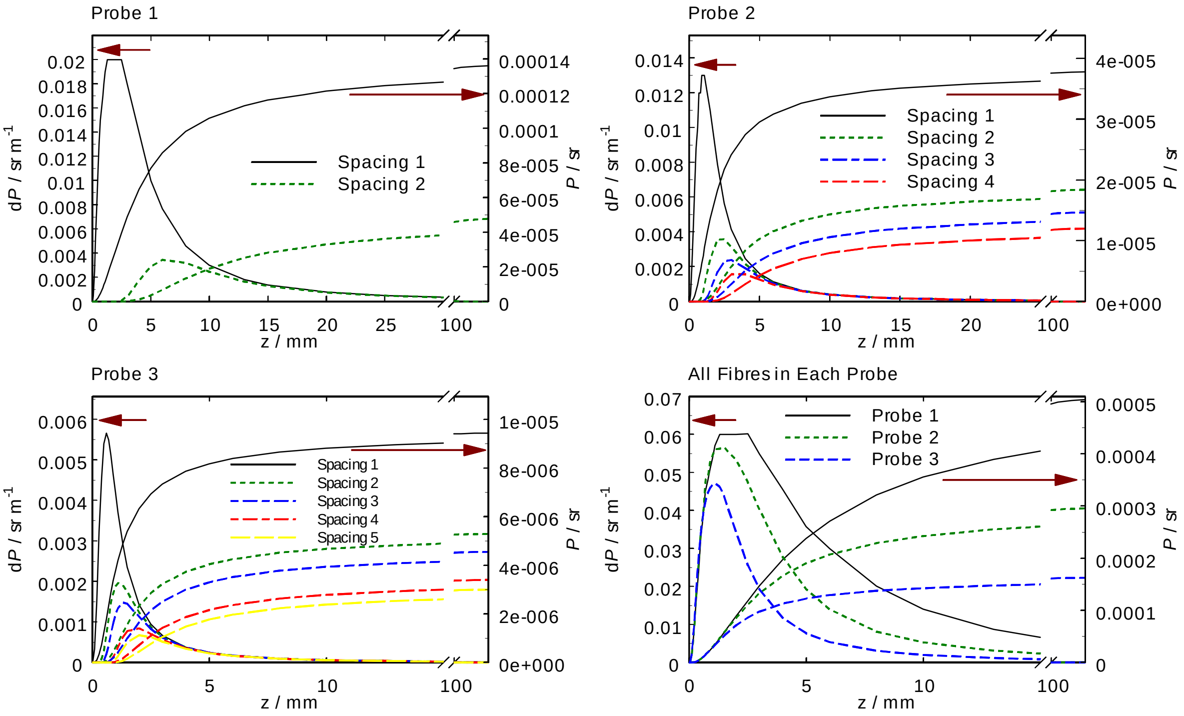

Figure 4.20 The collection efficiency of parallel fibre probes (d$P(z)$ and $P(z)$) for the fibre spacings of the probes illustrated in figure 4.19, given in table 4.3. The emission fibre radius in each case is 100 µm.

The increase in collection efficiency is slower than linear with collection fibre diameter, and in circumstances where the spectrograph input aperture was smaller than the collection fibre diameter (or the image of that diameter), then the smaller diameters could be preferable.

To contrast with the results of figure 4.20, the data from probes of the same configurations, subject to the same total height limit, but each made with identical *collection* fibres has been calculated. In this case the collection fibre radii are all 323 µm radius, and the emission fibre radius is varied to fit the probe configuration.

Table 4.4 The separations *D* between emission and collection fibres for probe configurations 1 to 3. The collection fibre radius is constant at 323 µm.

Probe	Total emission fibre radius (core + cladding)[†], r_{tm}	Separation D between emission fibre and collection fibres × number of fibres at that separation[*]	
1	$\left(\frac{2}{\sqrt{3}}-1\right)\times 323$ µm =50 µm	(2/√3)×323 µm =373 µm ×3	(5/√3)×323 µm =933 µm ×2
2	(√2-1)×232 µm =133.9 µm	√2×232 µm =457 µm ×4	(1+√3)×323 µm =883 µm ×1
3	323 µm	2×323 µm =646 µm ×5	Not applicable

[*] The number of useful collection fibres is limited by the 3.2 mm detector height. [†] The emission fibre core radius $r_m = r_{tm} - 5$ µm.

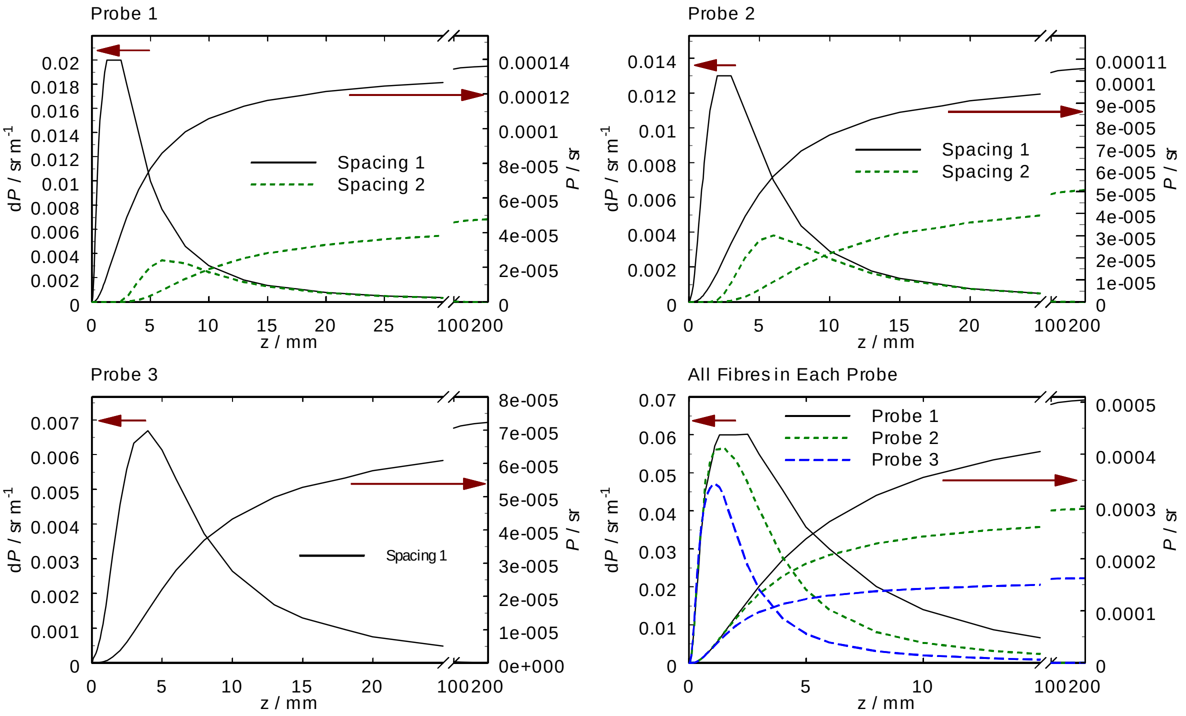

Figure 4.21 The collection efficiency of parallel fibre probes (d*P*(*z*) and *P*(*z*)) for the fibre spacings of the probes illustrated in figure 4.19, given in table 4.4. The collection fibre radius in each case is 323 µm.

Again, it is the probe 1 configuration that is the most efficient, but the effect is less pronounced, and all three configurations are equally efficient in collecting scattered light from the region closest to the probe tip. In this case the fibre arrangement at the input to the spectrometer from each probe is identical, and so no configuration has an advantage in the case that the input slit is smaller than the collection fibre diameter. From these results, it is seen that the most efficient probe design in that in which the emission fibre is as small as possible. This is due to the higher irradiance (*ie* higher concentration of power) across the output beam from the smaller fibre, and the smaller separation D between the centre of the emission and collection fibre.

4.5. Conclusions

In this chapter a complete descriptive model of the most common and generally applicable configuration for optical-fibre sensors has been developed. It has been shown to be capable of accurate quantitative predictions, as well as qualitatively describing the performance of parallel-optical-fibre probes, and has been tested over a wide range of sample absorbances and fibre separations, as well as with different sample refractive index or fibre numerical aperture. No previous studies of this problem by other workers that have given any consideration to absorbing samples were found in the literature, and none performed as extensive or well controlled study of the effect of the axial separation between the emission and collection optical fibres. Also, no other work has compared the absolute collection efficiency of the optical-fibre probes with theory. In this work the absolute collection efficiency was found to agree within experimental error to a literature value of the Raman scattering cross section of toluene.

For example, the most complete study of the theory of parallel-fibre probes in the literature, that of Cooney and his coworkers[75], showed a discrepancy of 0.21 mm (a 15% error) between the predicted and measured location of the maximum in dP for a 200 µm core flat tipped probe with 220 µm seperation. The results from this work (figure 4.10), although measured with 62.5 µm core fibres, were measured using essentially the same method, and show exact correspondence with prediction within the 0.05 mm resolution of the experiments, over a range of fibre separations of 125 µm to 602 µm.

The model developed in this work has been expressed in the coordinate system defined by the symmetry of the problem, which has allowed straight forward evaluation of the equations by the MathCad software. Other workers have defined the problem in Cartesian coordinates, or used step functions to define the limits of the numerical integrations. Using coordinates with the same symmetry as the problem allows more efficient numerical algorithms to be used to evaluate the integrals.

The particular form of the irradiance distribution used in the model has been shown to be of most importance for single-fibre probes, where the overlap between the emission and collection cone is complete, and most of the collected light originates from the region adjacent to the probe tip. For the case of parallel-fibre probes, no light is collected from the region immediately adjacent to the probe tip, and the form of $dP(z)$ is determined more by the increase in overlap between the emission and collection cones than by the distribution of light across them. This is in agreement with other authors, although the model for the irradiance described in this work is more complete.

The effect of solution absorbance has been shown to be negligible while the product $z_{max} \cdot (\alpha_c + \alpha_m) < 100$, where z_{max} is the position of the maximum in $dP(z)$. With this result the absorbance may be neglected for many solutions of interest, speeding calculation time. The omission of leaky modes from the analysis has not resulted in a large deviation between theory and experiment, however, it may be desirable to include leaky modes in a more complete analysis. This could be achieved by making the upper limit of ϕ in equation 4.7 a function of the distance between the point at which a ray strikes the collection fibre and the centre of the fibre end face. This is not a trivial problem, and might considerably increase the time required to calculate the numerical integrals.

Finally, it has been shown that for efficient collection of light from a scattering sample from a multiple-fibre probe, the emission fibre radius should be as small as possible, and the collection fibre core radius should be as large as possible, within the constraints of the spectrograph input slit width.

5. Cell Designs

Several novel sample cell designs, designed to enhance the collection efficiency of optical-fibre probes, are described in this chapter. All the cells described rely on some form of light-guiding for their operation, whether partial (*ie* Fresnel reflection), or total (*ie* waveguiding, by total-internal reflection). A definition of the enhancement provided by light-guiding sample cells is given, and the mathematics governing the magnitude of the enhancement is developed. The individual experimental configurations, fabrication techniques, and measured enhancements are described in the subsequent sections.

5.1. Collection Enhancement From A Light-Guiding Cell

One way to enhance the collection efficiency of an optical-fibre probe is through the use of a capillary tube which has a diameter approximately equal to the probe diameter (figure 5.1)[85][86][87][88][89]. By confining incident light, and scattered light, to within the fixed cross-section of the capillary, then, in the absence of absorption, the intensity of the light collected from a cross-section of differential thickness dz will remain constant with the distance z from the probe tip (see figure 5.1). In terms of the mathematical model of the previous chapter, the collection solid angle is constant from the distance z_i at which the collection cone intercepts the capillary wall. The enhancement provided by any cell is defined as the ratio of the signal collected from a cell of length z_i to that measured by the probe alone, in an infinitely deep sample. It should be noted that the sample *volume* within a capillary cell of length z would typically be much less than that required to study a sample with the probe by itself.

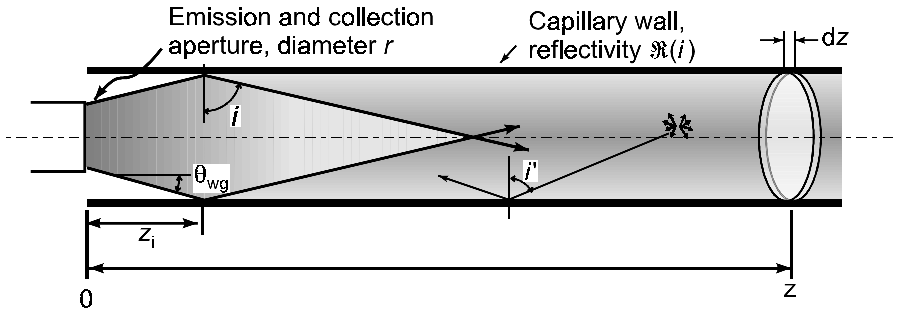

Figure 5.1 The coupling between an optical-fibre probe and a light-guide: An incremental quantity of collected flux, d$P(z)$, is considered to originate from the thin slice of thickness dz. The reflectivity of the cell walls is a function of incident angle, $\Re(i)$.

Raman signal enhancement of over 30 have been observed by Schwab and McCreery[76], who used a 70 cm long capillary of 1.3 mm internal diameter. Dyer and Hendra[87] have used a capillary, internally coated with gold, for enhancing the Raman spectra of gases using NIR excitation. Walrafen and Stone[85] used a glass tube to form a waveguide with liquid analytes of high refractive index, and reported enhancements of between 100 and 1000.

5.1.1. Collection enhancement factor model

In this analysis it is assumed that the light-guiding capillary cell (the *light-guide*) is cylindrical, and the incident and collected light enters and leaves the cell via an optical fibre probe (the *probe*) with a circular aperture, which is centred on the cylinder axis, as shown in figure 5.1. The probe aperture is assumed to be smaller than the cylinder cross section, and emission from the analyte is assumed to be isotropic, a reasonable assumption for the small range of angles over which it is collected by the probe; in this work the useful *NA* of the probe was 0.17, limited by size of the diffraction grating in the spectrograph. Again, only light that is fully guided by the probe is considered here (see section 4.2), which may result in an underestimate of the total collected flux. First, a model for the case of perfect light-guides (*ie* waveguides) with a *NA* greater than that of the probe is developed, and then it is shown how this may be generalised to include lossy light-guides.

Within a waveguide, any light making an angle of less than θ_{wg} to the axis will undergo repeated total internal reflection, where 90°-θ_{wg} is the critical angle given by Snell's law. Excitation light diverges from the probe until it intersects the waveguide wall, at the point marked z_i in figure 5.1. Because the waveguide *NA* is less than that of the probe, the light is reflected back towards the centre of the waveguide. Fluorescent or Raman light is emitted within the cylinder, and some of this light will follow a path back to the probe.

The proportion S of the light emitted by the analyte that is guided towards one end of the waveguide is given by equation 5.1.

$$S = \frac{2\pi(1 - \cos(\theta_{wg}))}{4\pi} = \sin^2\left(\frac{\theta_{wg}}{2}\right) \qquad \mathbf{(5.1)}$$

The most efficient means of coupling this light to a probe is to immerse the probe into the liquid-core of the waveguide. For a collection aperture perfectly matched in size to the water cylinder cross section, the coupling efficiency L_{NA} between the probe and the waveguide is given by equation 5.2,

$$L_{\mathrm{NA}} = \frac{\Omega_{\mathrm{p}}}{\Omega_{\mathrm{wg}}} = \frac{4\pi\sin^2(\theta_{\mathrm{p}}/2)}{4\pi\sin^2(\theta_{\mathrm{wg}}/2)} \tag{5.2}$$

where θ_{p} is the half-cone angle of the probe, Ω_{p} is its solid angle, and Ω_{wg} is the solid angle of light guided within the waveguide.

In the case where the waveguide cross section is larger than the probe aperture, the coupling efficiency due to radius mismatch[90] is given by equation 5.3.

$$L_{\mathrm{radii}} = \frac{r^k}{R^k} \tag{5.3}$$

Here r is the probe radius, R is the waveguide radius, and k is a constant between 1 and 2 which depends on the distribution of scattered light within the waveguide. A value of k=1 represents the case where all rays pass through the waveguide axis, whereas k=2 represents the case where skew rays carry an equal amount of energy (*ie* all waveguide modes are equally excited). Even if the incident light is delivered to the waveguide under the conditions for k=1, and if the waveguide walls are perfectly smooth, the scattered light distribution will only approximately follow that of the incident light. Random perturbations of the ray paths at the waveguide walls will further randomise the light distribution so that $1 \le k \le 2$.

The two equations 5.2 and 5.3 multiply to give the fraction of flux transferred from the waveguide to the probe. To find the total flux collected, the differential flux element d$P(z)$ is integrated between the probe tip and the end of the capillary (see section 4.2). Again, d$P(z)$ is the photon flux scattered *and then collected* from a cylindrical differential volume element (a tube cross-section of thickness dz), at a distance z from the probe, as shown in figure 5.1.

Before the emission and collection cone intersects the waveguide wall at z_{i}, the waveguide has no effect on the amount of flux collected. Beyond the point z_{i} the total irradiance on the waveguide cross section is constant, assuming that no light is absorbed. By reciprocity, the flux collected by the probe from any cross section, d$P(z)$, will also be constant beyond z_{i}. For the general case where the sample is absorbing, d$P(z)$ is a function of z, and is given by equation 5.4.

$$\begin{aligned} \mathrm{d}P(z) &= P_0 n_\sigma \sigma \cdot \exp(-(\alpha_{\mathrm{x}} + \alpha_{\mathrm{m}})z) \cdot S \cdot L_{\mathrm{NA}} \cdot L_{\mathrm{radii}} \cdot \mathrm{d}z \\ &= P_0 n_\sigma \sigma \cdot \exp(-(\alpha_{\mathrm{x}} + \alpha_{\mathrm{m}})z) \cdot \sin^2(\theta_{\mathrm{p}}/2) \cdot \frac{r^k}{R^k} \cdot \mathrm{d}z \end{aligned} \tag{5.4}$$

Here P_0 is the total flux emitted from the probe tip, n_σ is the number density of scattering molecules, and σ is the molecules total scattering cross section in the direction of collection. The variables α_m and α_c are the attenuation coefficients at the emission and collection wavelengths respectively, and are discussed more fully in the following section; however, if α_m and α_c are both small, then d$P(z)$ is approximately constant. Equations 5.2-5.4 are only valid for $z>z_i$; before this point the flux collected by the probe is unaffected by the presence of the waveguide, and dP(z) is as given in equation 4.2.

By integrating the flux excited and then collected along a waveguide of length z_c, the expression for the total flux collected, $P(z_c)$, is given by equation 5.5.

$$\begin{aligned} P(z_c) &= \int_{z_i}^{z_c} \mathrm{d}P(z)\cdot\mathrm{d}z + P_{BP}(z_i) \\ &= \sin^2(\theta_p/2)\cdot\frac{r^k}{R^k}\cdot\frac{P_0 n_\sigma \sigma}{\alpha_x+\alpha_m}\Big(\exp(-(\alpha_x+\alpha_m)z_c)-\exp(-(\alpha_x+\alpha_m)z_i)\Big) + P_{BP}(z_i) \end{aligned} \qquad \textbf{(5.5)}$$

The constant $P_{BP}(z_i)$ is the flux collected by the probe between $z=0$ and $z=z_i$ (unaffected by the waveguide), as found using the equations of chapter 4. If the waveguide is long (large z_c), or narrow (small z_i) $P_{BP}(z_i)$ may be ignored. In this work results are presented in terms of the enhancement factor F, which is the ratio of the intensity measured by the probe coupled with the waveguide, $P(z_c)$, to that measured using the probe alone, $P_{BP}(\infty)$. $F(z)$ shares the same dependance on the waveguide parameters as $P(z)$. From equation 5.5 it is seen that when $P_{BP}(z_c)$ is negligible, then the flux collected, and hence the enhancement F, is proportional to R^{-k}.

5.1.2. Attenuation mechanisms and imperfect light guides

Two mechanisms of light loss affect the efficacy of the capillary enhancement: light attenuation in the analyte (absorption and scattering), and imperfect reflections from the interface between the tube and the analyte. Both of these losses are dependant on the angle at which the light travels through the tube. Attenuation of light by the analyte is proportional to the path length of the light[91] (multiple scattering events being ignored), and while the attenuation coefficient of the analyte itself (at the incident wavelength), α_m, is not dependant on angle, the pathlength through the capillary is. For a distance z through the tube, the path length of a ray at an angle i to the tube wall normal is $z/\sin(i)$.

For an imperfect waveguide with a reflectivity less that one, only a fraction $\Re(i)$ of the light will be reflected at each encounter with the walls of the capillary. The loss of light may be due to imperfect light-guiding, *eg* if the light is confined only by Fresnel reflection, when the conditions for waveguiding are not met; or because of roughness or contamination on the capillary walls which scatters light from the waveguide. After a total m reflections, the intensity is $\Re(i)^m$ of its initial value. The number of reflections m that an axial ray striking the walls of a capillary of radius R and length z experiences is $z/2R\cdot\tan(i)$.

The combined differential change of power $d\Phi$ for light travelling through a tube at an angle i can be written

$$d\Phi = -\Phi\left(\frac{\alpha_m}{\sin(i)} - \frac{\ln(\Re(i))}{2R\tan(i)}\right) dz. \qquad \text{Corrected July 1999} \quad \textbf{(5.6)}$$

The bracketed expression in equation 5.6 defines an angle dependant *total attenuation coefficient*, K for axial rays travelling through the waveguide at an angle i to the capillary wall normal. For light at the wavelengths emitted and collected by the probe, the coefficients are given respectively by

$$K_m(i) = \left(\frac{\alpha_m}{\sin(i)} - \frac{\ln(\Re(i))}{2R\tan(i)}\right)$$
$$K_c(i') = \left(\frac{\alpha_c}{\sin(i')} - \frac{\ln(\Re(i'))}{2R\tan(i)}\right) \qquad \text{Corrected July 1999} \quad \textbf{(5.7)}$$

Accepting the condition that the probe is constructed from optical fibres with NA much less than 1 (silica fibres of NA 0.2 satisfy this), then K_m and K_c may be taken as constants, independent of angle, and substituted directly into equation 5.5, with the mean value of i. This will be accurate to within 5% while the product $(K_m+K_c)\cdot z$ is less than 2.

No exact expression for the intensity of light collected from a probe coupled with a capillary light-guide (as was given in section 4.2 for the case of the probe alone) is presented here. This is because of the more complicated geometry of the situation; more angular variables would be required to describe the path of rays back to the probe, increasing computation time exponentially for little increase in precision.

5.2. Fresnel Capillary Cells

An example of an imperfect light guide as described in the previous section is a glass capillary tube filled with an aqueous solution. Because the refractive index of water (approximately 1.3) is below that of any glass (typically 1.5 for silica glasses), there can be no total-internal reflection (*ie* waveguiding). However, as described in section 2.3.3, light incident on a boundary between materials of different refractive indices will be at least partially reflected by Fresnel reflection.

5.2.1. Silica cells

The fraction of light that is reflected due to refractive index mismatch can become large if the light is incident at grazing angles. The reflectivity for unpolarised light is[92]

$$\Re_{\mathrm{av}}(i) = \frac{1}{2}\left(\frac{n_{\mathrm{ti}}^2\cos(i) - \sqrt{n_{\mathrm{ti}}^2 - \sin(i)^2}}{n_{\mathrm{ti}}^2\cos(i) + \sqrt{n_{\mathrm{ti}}^2 - \sin(i)^2}}\right)^2 + \frac{1}{2}\left(\frac{\cos(i) - \sqrt{n_{\mathrm{ti}}^2 - \sin(i)^2}}{\cos(i) + \sqrt{n_{\mathrm{ti}}^2 - \sin(i)^2}}\right)^2 \quad \textbf{(5.8)}$$

where i and t are as shown in figure 5.2, t is given by equation 2.20, and n_{ti} is the relative refractive index between the capillary and the analyte, n_t/n_i.

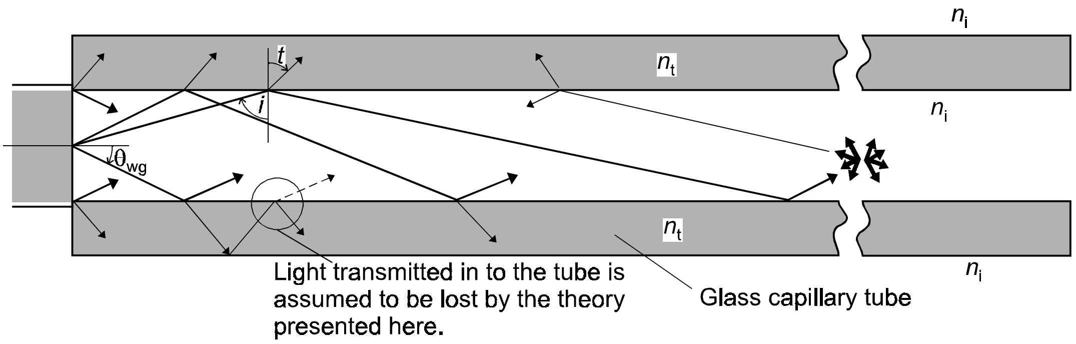

Figure 5.2 Light may be partially confined in a medium of lower refractive index than its surroundings by Fresnel reflections.

$$T(z) = \frac{1}{\theta_p}\int_{\pi/2-\theta_p}^{\pi/2} \exp\left(-K_m(i)\cdot z\right)\mathrm{d}i \quad \textbf{(5.9)}$$

Making the assumption that the cone of light emitted from the fibre tip is homogeneous, the fraction T of the input light remaining within the tube after a distance z is given by equation 5.9, where θ_p is the semi-cone angle of the fibre immersed in the analyte. This integral has been evaluated numerically, and is plotted against tube length in figure 5.3. Also plotted in figure 5.3 are measured values of the light transmitted through a de-ionised-water-filled Pyrex tube against tube length, with the parameters of equation 5.7 empirically adjusted to give the best fit ($T(i)$ has been increased by 0.35 and α_m has been increased by 2 m^{-1} to 2.4 m^{-1}). The transmission through the cell walls may be due to surface roughness of the internal walls, and the increased absorption due to scattering from particles unavoidably introduced into the water.

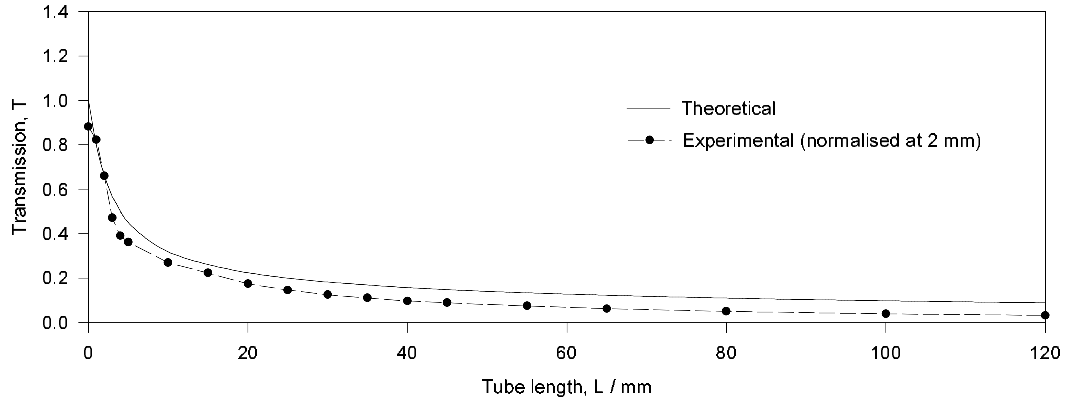

Figure 5.3 The transmission of a water-filled tube of diameter d=0.5 mm, where light is confined by Fresnel reflections. The experimental data has been scaled so that it coincides with the theoretical curve at z=2 mm.

Using an experimental set up with the fibre probe sheathed in a glass capillary tube as in figure 5.4, the enhancement of the capillary and single fibre sensor combination was evaluated (figure 5.5). The theoretical curve takes into account the light exiting from the tip of the capillary, and incorporates the empirically measured transmission data (figure 5.3). The estimated error bars are taken from the measured noise in the detector array dark reading, which has been subtracted from each measurement.

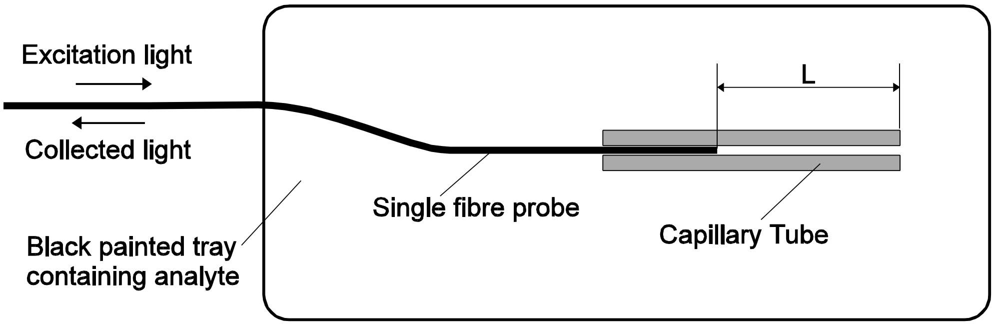

Figure 5.4 Using a capillary tube to enhance the collection efficiency of a single fibre probe. The capillary and fibre tip are immersed in the analyte, and the tube slides freely along the fibre.

The maximum theoretical enhancement of 1.8 (figure 5.5) is limited by the relatively high absorption coefficient of the fluorescent analyte (22 m^{-1}). For a low concentration of contaminant in water the maximum enhancement is approximately 5, over a capillary tube length of 25 cm).

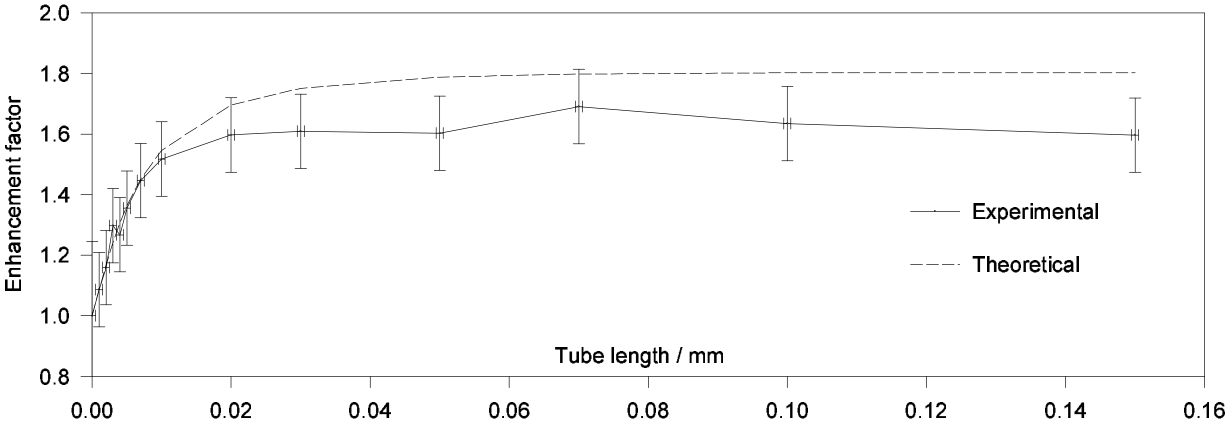

Figure 5.5 The measured collection enhancement of a single fibre probe in a 0.5 mm inner-diameter Pyrex capillary tube.

The relatively high enhancements reported by Schwab and McCreery[130] resulted from their tubes being suspended in air, which allows guiding of light at the external surface of the tube, and the lower absorbance of their analyte. Further enhancement could be achieved by using capillaries of higher refractive index, such as silicon (n=5).

Better still is to use of a capillary which fully confines the light within it.

5.3. Waveguiding Capillary Cells

In this section three novel approaches to this problem are presented, all suitable for use with aqueous solutions.

5.3.1. Teflon-AF amorphous fluoropolymer

The copolymers marketed by the Du Pont company under the trade name *Teflon* typically consist of more than 90% of the monomer TFE, with co-monomers introduced to reduce the crystallinity and shorten the length of the poly(tetrafluoroethylene) chains within the compound[93]. The copolymer is then more amenable to thermal processing or solvation in certain solvents. However, any crystallites formed in the copolymer are optically scattering. These polymers are renowned for their low surface energy, chemical inertness, and strength. The Teflon-AF brand shares these properties, but it is unique among the Teflon compounds because it is optically transparent, with much lower scattering, and is unique among solid polymers, having a refractive index[94] in the visible and NIR of less than 1.32.

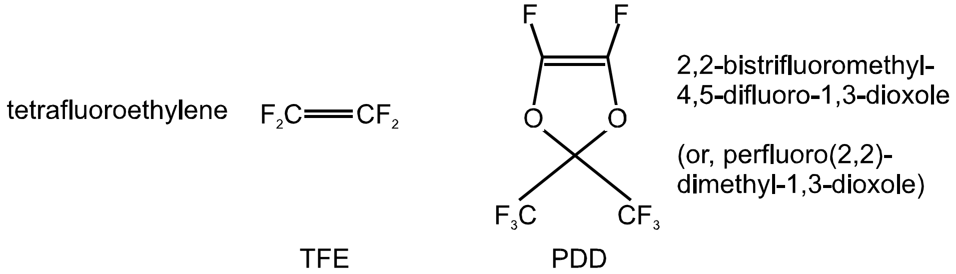

Figure 5.6 The co-monomers of the Teflon AF family of amorphous fluoropolymers.

Teflon AF is a copolymer of TFE and PDD (see figure 5.6), and typically comprises 60% PDD, or more. It is the ring structure of PDD which prevents crystallinity, and hence renders the copolymer optically transparent over the whole visible region, extending to approximately 2.7 μm in the near infrared. In addition, the PDD ring structure results in nano-voids in the copolymer, so that the refractive index of the resulting compound is significantly lower than other materials. Two variants of Teflon AF are readily available, AF-1600, and AF-2400, having glass transition temperatures of 160°C and 240°C, and refractive indices of 1.312 and 1.295 respectively. The Raman spectrum, and results from a differential thermal analysis of Teflon AF-1600 are presented in appendix F.

Teflon AF copolymer can be processed by compression moulding, or may be deposited from solution in certain fluorinated solvents, the approach taken in this work. Teflon AF-1600 has been used because it was available in a more concentrated solution. The films were deposited from solution in FluorInert FC75 (ICI, UK), a totally fluorinated compound, onto silica glass capillary tubes[95]. It was found that, despite pre-treating the silica surface with a fluoro-silane compound (the tubes were boiled under reflux for 1 hour in a 0.5% solution of 1H,1H,2H,2H-perfluorodecyltriethoxysilane in methanol), adhesion of the films was poor in the presence of water. In fact, tubes of Teflon AF with approximately 10 μm thick walls could be formed by leaving internally-coated glass tubes submerged in water for an hour or so. The water migrated between the silica and the fluoropolymer coating, and the fluoropolymer tube was released. It could eventually be gently pulled out by hand, and left to dry in air. Layers of Teflon AF deposited onto a PTFE substrate are much more stable however.

5.3.2. Teflon AF as a waveguide cladding material

Although Snell's law defines the critical angle for total internal reflection, energy penetrates the waveguide cladding as an evanescent wave, the intensity of which decays exponentially with depth. For efficient waveguiding the thickness t of the AF layer should be larger than the penetration depth δ of the light incident onto the tube wall from the core. This depth is given by equation 5.10, where n_t is the refractive index of the cladding (AF film), n_i is the refractive index of the liquid core, and λ_i is the wavelength of the incident light[96].

$$\delta = \left(\frac{2\pi}{\lambda_i} \sqrt{\frac{\sin^2(i)}{(n_t/n_i)^2} - 1} \right)^{-1} \tag{5.10}$$

It has been assumed that all energy which penetrates the AF coating is lost from the waveguide. Under this assumption, the transmission of rays at an angle i to the normal of the waveguide wall is then given by equation 5.11, where z is the axial distance travelled through the waveguide, and R is the waveguide radius. The power to which the exponential term is raised is the number of reflections that a ray undergoes in the length z. Rays incident on the tube wall at angles close to the critical angle are poorly guided, due to their greater penetration depth and the larger number of reflections which they undergo.

$$T = (1 - \exp(-t/\delta(i)))^{\frac{z}{2R \cdot \tan(i)}} \qquad \text{Corrected July 1999} \tag{5.11}$$

In figure 5.7 the total transmission through the tube (averaged over all guided ray angles) has been plotted. It is seen that once the rays close to the critical angle have left the waveguide, then the transmission levels off. Analyte absorption has been ignored here, but may be significant, depending on the liquid under study, and the incident wavelength. It is apparent that, for efficient transmission through the waveguide, a film thickness of at least 15 μm is desirable. Sufficient solution was deposited in each tube so that, on average, coatings of at least this thickness in were deposited.

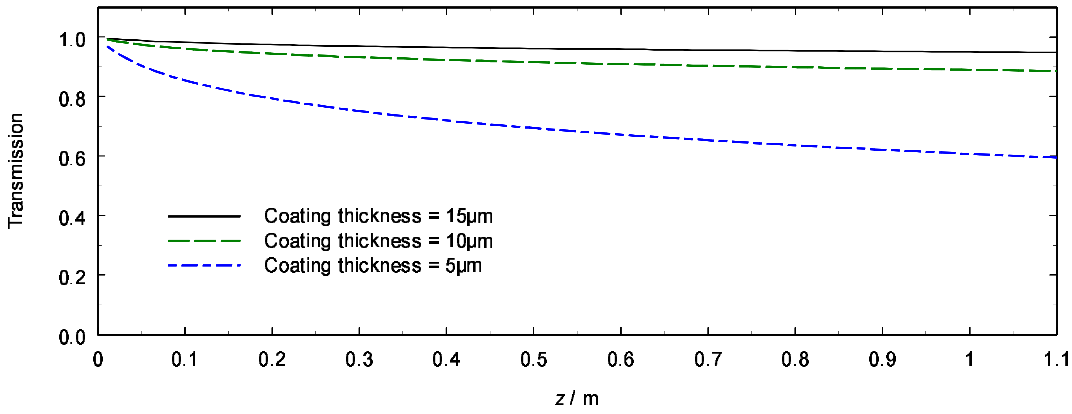

Figure 5.7 The calculated total transmission through a 0.955 mm radius liquid-cored, AF-1600 clad waveguide against length, assuming that at L=0 light is isotropically distributed over the NA of the waveguide, and that there are no skew rays. The liquid core is assumed to have a refractive index of 1.33, and have no absorption.

5.3.3. Experimental measurements and results

Two experiments are described here. The first was to quantify the performance of the cells as optical waveguides, and the second was to evaluate their utility as spectroscopic cells, where they were used to enhance the collection of fluorescence from a 30 µg/L solution of Panacryl Blue 5G (see section 4.3.3 for more details of the dye solution).

5.3.3.1. Cell transmission and numerical aperture

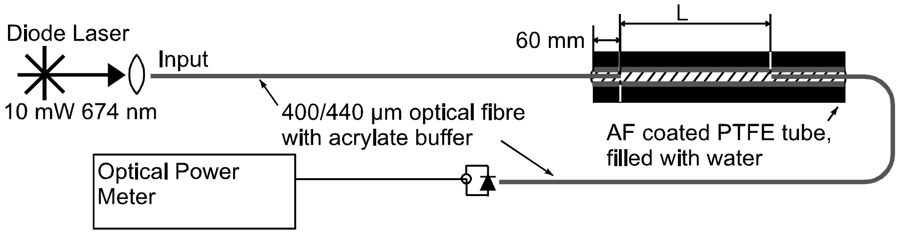

Figure 5.8 Measuring the transmittance through a water-filled internally-Teflon-AF-coated PTFE tube. The light delivery and collection fibres were inserted into each end of the water filled tube, and the length *L* between them was varied.

The arrangement illustrated in figure 5.8 was used to measure the *transmission* of the water or fluorescent-dye cored waveguides. They were filled with liquid using a syringe, and the liquid remained within the tube, held by surface tension. Light from a 674 nm diode laser was coupled into the aqueous core via an optical fibre inserted up to 60 mm into one end of the capillary. A similar fibre was inserted into the other end of the tube, which was coupled to a calibrated optical power meter.

The optical fibres were Heraeus low OH silica, with an *NA* of 0.22, core diameter of 400 µm, cladding diameter of 440 µm, and a total diameter (including an acrylate buffer) of 650 µm. The laser coupling optics filled the *NA* of the fibre. When studying the 0.955 mm radius waveguides a section of approximately 40 mm at the tip of each fibre was sleeved with the smaller radius PTFE tube, to keep the fibres close to the centre of the waveguide.

5.3.3.2. Fluorescence collection enhancement

A similar arrangement was used to measure the fluorescent enhancement due to the use of the waveguides, illustrated in figure 5.9. First, the intensity of fluorescence collected by immersing the fibre probe directly into the fluorescent dye was measured. Then, the waveguides were filled with the fluorescent dye solution, and the probe inserted into the aqueous core. Excitation light at 674 nm, and scattered light, was coupled to and from the probe via a 50:50 coupler. The scattered light was resolved using a concave-grating CCD-spectrograph.

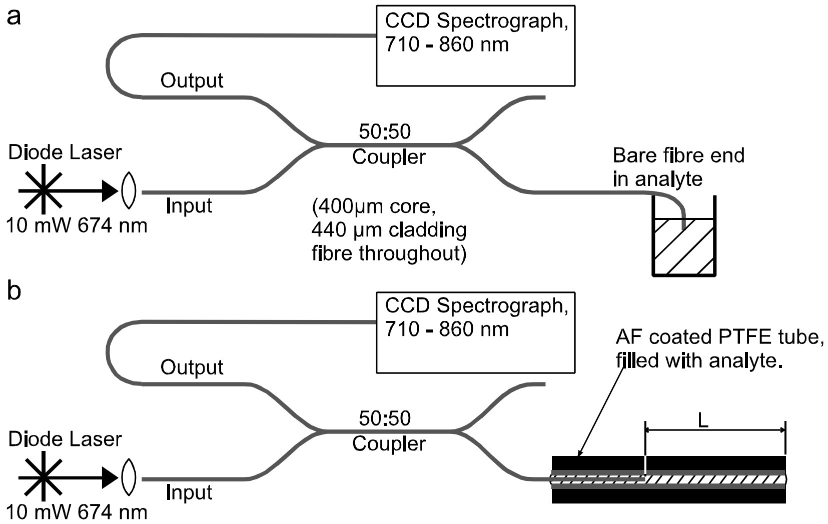

Figure 5.9 Measuring the fluorescence intensity of light collected using a bare optical fibre probe, and with the probe sheathed in an internally-Teflon-AF-coated PTFE tube. The length *L* was varied.

5.3.3.3. Transmission and fluorescence collection results

In this section the transmission and fluorescent collection enhancements of the waveguides are presented. First the results for the shorter (less than 200 mm) waveguides are given, and then the results for the longer (greater than 800 mm) waveguides.

5.3.3.4. Optical transmission of the water filled tubes

The graphs in this section (figures 5.10 and 5.11) show the optical power collected from water- and dye-solution-cored waveguides in transmissive mode. The total apparent absorption coefficient (K / mm) has been calculated in each case from the slopes of the regression lines shown, and its value is given (inset) in each graph. These transmission measurements were made at a wavelength of 674 nm, where the absorption of water is 20×10^{-3} m^{-1}, and the absorption of the 30 µg/L Panacryl Blue solution is 14.9×10^{-3} m^{-1}. These values are seen to be insignificant compared with the loss of the waveguides themselves.

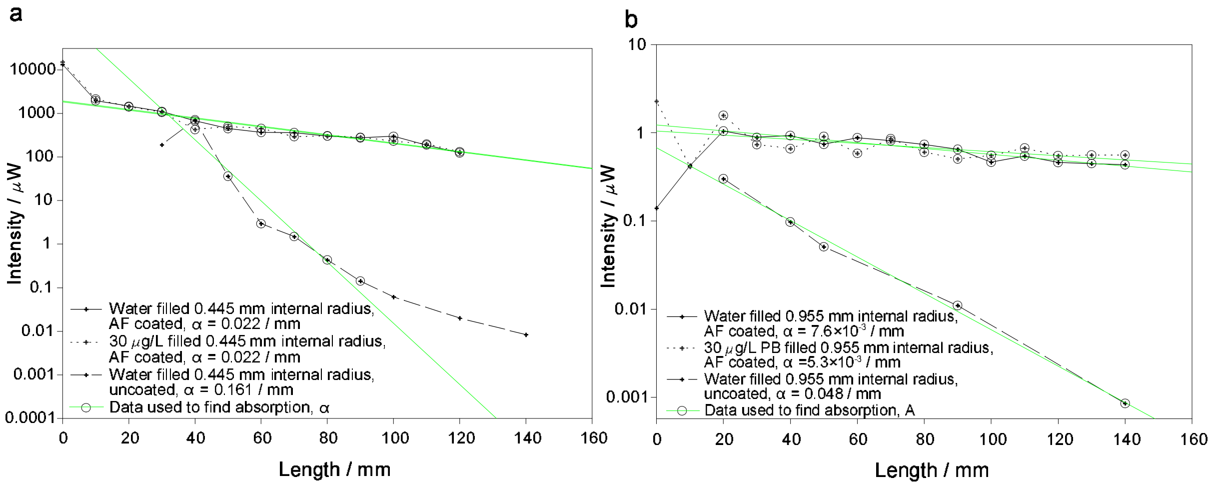

Figure 5.10 The optical transmission through the short AF-1600 coated water- and dye-solution-filled waveguides, compared with a section of uncoated tube; a) 0.445 mm internal radius b) 0.955 mm internal radius.

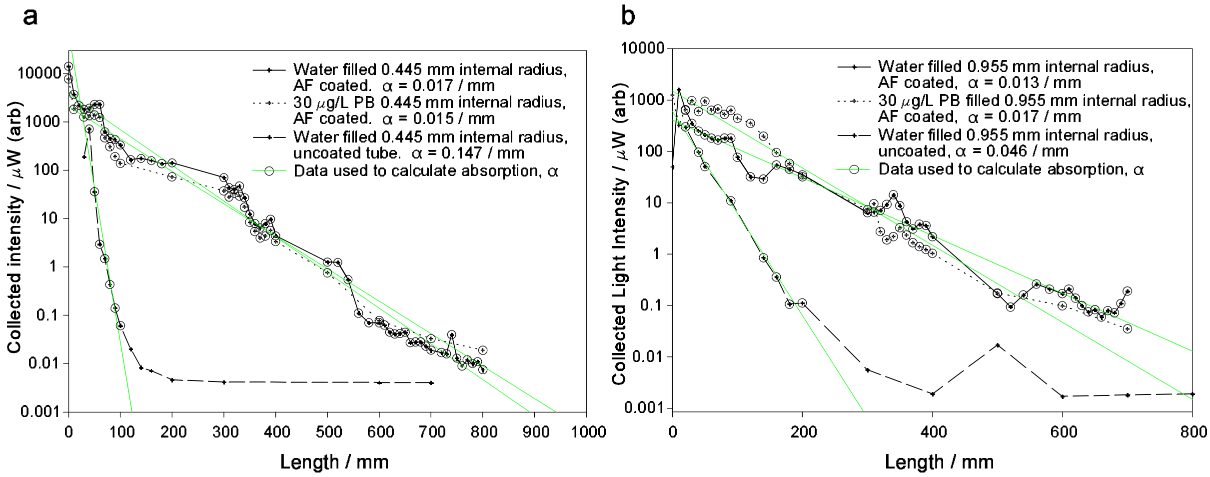

Figure 5.11 The optical transmission through the long AF-1600 coated water- and dye-filled waveguides, compared with a section of uncoated tube; a) 0.445 mm internal radius b) 0.955 mm internal radius

Variations in the level of side scattering from the long tube were clearly visible, probably due to variations in the AF film thickness.

5.3.3.5. Fluorescent collection enhancement using waveguiding cells

In this section the enhancement in the collection efficiency of a single optical fibre probe when coupled with the waveguiding cells, as shown in figure 5.9, is presented (figures 5.12 and 5.13).

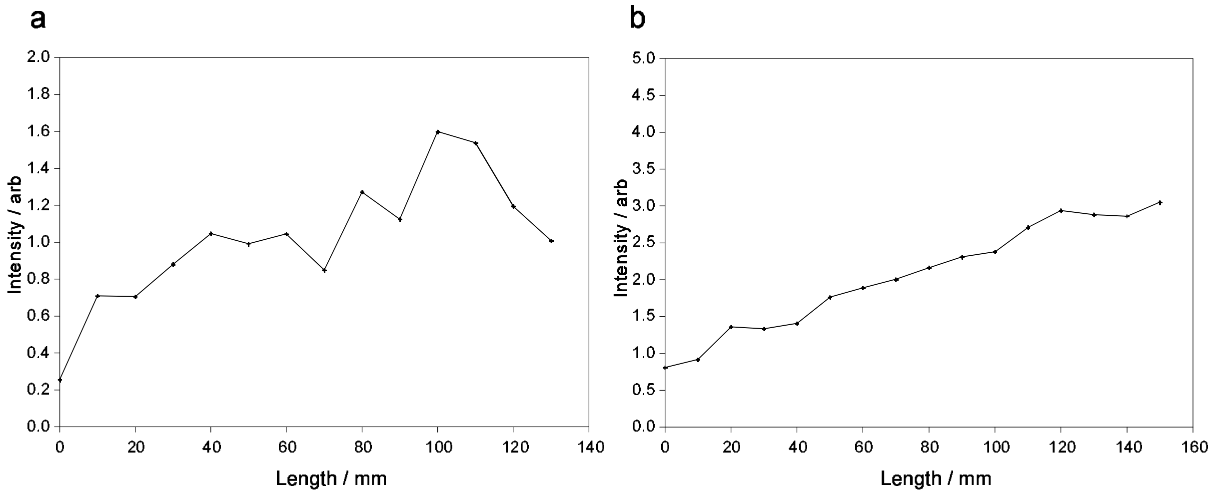

Figure 5.12 The fluorescent collection enhancement from coupling a single optical fibre probe with the short AF-1600 coated waveguides. a) 0.445 mm internal radius b) 0.955 mm internal radius.

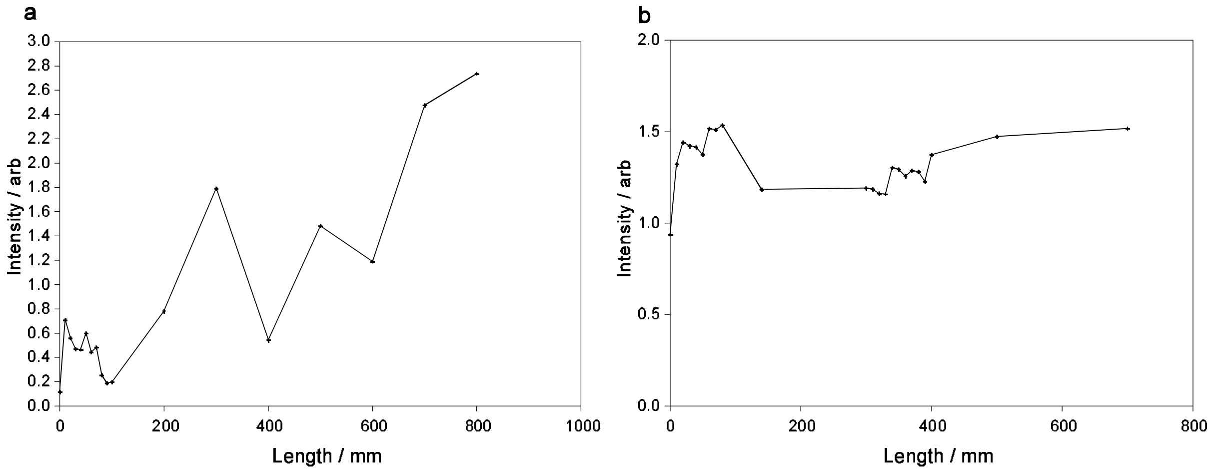

Figure 5.13 The fluorescent collection enhancement from coupling a single optical fibre probe with the long AF-1600 coated waveguides. a) 0.445 mm internal radius b) 0.955 mm internal radius.

The effects of variations in the film thickness are evident here in the large and rapid changes in collection enhancement, especially in figure 5.13. The collection efficiency was only reasonable when the probe tip was sheathed in a strongly guiding part of the cell. Other poorly-guiding regions were found to prevent the enhancement increasing linearly with length, as expected by theory.

Throughout the experiments the movement of the optical fibre against the cell walls did not cause any visible damage to the AF films. In addition, immersion for several days in water and IPA did not affect the adhesion of the films to the PTFE wall.

5.3.4. Gold Coated Capillary Cells

Metallic reflection is another approach to confining light within a capillary tube. Most metals have high reflectivity of light from the visible to infra-red region of the spectrum[97], and Pyrex tubes, internally coated with gold metallic films were chosen for inertness, and novelty. (The reflectivity of silver and gold is approximately equal for wavelengths above 600 nm; however, gold is more resistant to corrosion, but also much harder to deposit onto the tube.)

The internally gold-coated capillary was supplied to us by the Chemistry Department, having been coated by Mike Caplen using a proprietary process. The metallic surface was deposited by a chemical process, and was not perfectly smooth. By cutting a short section axially, inspection under a microscope revealed pinholes of approximately 5 μm diameter in the 5 μm thick coating. Surface profiling (using a 5 μm radius stylus) revealed peak to peak surface roughness of 0.5 μm over a distance of 1 mm. This has reduced the reflectivity of the gold surface, which has been taken as a constant, 0.7, independent of angle in fitting the theoretical curve to the results of figure 5.14.

The experimental results (figure 5.14) show the effects of bubbles in the capillary tube. Bubbles seemed to adhere more strongly to the gold coated wall than to the bare Pyrex, and they act as efficient scattering centres, much reducing the apparent reflection coefficient of the metal surface. As the fibre probe was moved down the length of the capillary the collected intensity falls in the immediate vicinity of a bubble.

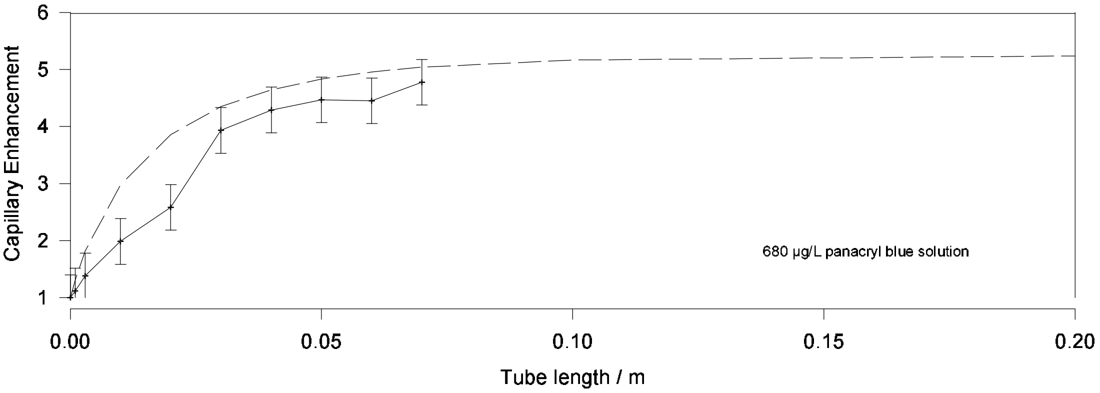

Figure 5.14 The calculated and measured values of the collection enhancement of a single optical-fibre sensor with an internally gold coated capillary tube.

5.3.5. Falling Analyte Stream

Surface roughness of the capillaries has been a dominant factor in all the approaches described so far. By taking the novel approach of dispensing with the capillary, the analyte can be made to form a waveguide by itself. By allowing the analyte to flow through a circular nozzle, a continuous cylindrical stream can be formed, which forms a perfect waveguide with a large *NA*. The most convenient method of coupling light in and out of the stream is via an optical fibre probe, figure 5.15, or it is possible to use lenses to make the measurement non-contact.

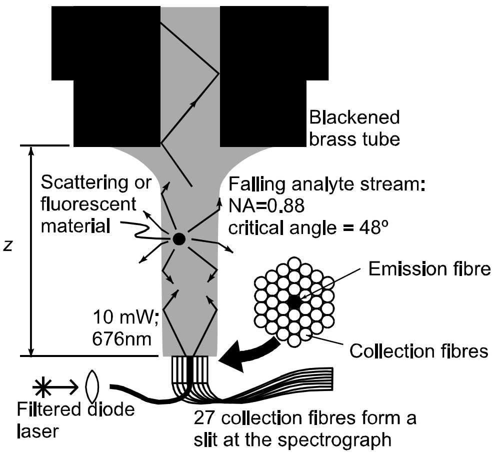

Figure 5.15 A falling analyte stream is a novel and efficient means of confining light within an analyte. Light is easily coupled in and out of the analyte stream via an optical fibre probe placed at the bottom of the stream.

5.3.5.1. Stream stability

The stability of low velocity liquid streams has been considered by Weber[98]. His formula for the critical length of a water stream (the stable length of the stream) is given in equation 5.12.

$$z_c = \frac{2vR_c}{\gamma}\left(\sqrt{2\rho\gamma R_c} + 3\eta\right)\log_e\left(\frac{R_c}{\Psi_0}\right) \qquad \textbf{(5.12)}$$

Here z_c is the critical (stable) length of the stream, R_c is the critical radius of the stream, v is the average fluid velocity at the break-up point, ψ_0 is the amplitude of the disturbance which causes the stream to break up, η is the viscosity of the fluid, ρ is the density of the fluid, and γ is the surface tension of the fluid.

5.3.5.2. The shape of water streams in free fall

Falling water streams of circular cross section are described in this section. The shape of a fluid stream falling vertically under gravity has been found by solving the Navier-Stokes equations in cylindrical coordinates

$$\begin{aligned} \rho\left(u_r \frac{\partial u_z}{\partial r} + u_z \frac{\partial u_z}{\partial z} \right) &= \rho g - \frac{\partial P}{\partial z} \\ \rho\left(u_r \frac{\partial u_r}{\partial r} + u_z \frac{\partial u_r}{\partial z} \right) &= - \frac{\partial P}{\partial r} \end{aligned} \qquad \textbf{(5.13)}$$

where the z-axis is the axis of symmetry of the falling water stream, the r-axis is normal to z, u is the velocity of the fluid, P is the hydrostatic pressure in the fluid, and g is gravitational acceleration.

A number of approximations can be made to simplify these equations, for water streams: the viscosity of water has negligible effect, the radius of the stream is not a strong function of z, and the water velocity is a function of z only.

The solution is then given by[99]

$$z = \frac{Q^2}{2\pi^2 g}\left(\frac{1}{R^4} - \frac{1}{R_0^{\,4}} \right) + \frac{\gamma}{\rho g}\left(\frac{1}{R} - \frac{1}{R_0} \right) \qquad \textbf{(5.14)}$$

where Q is the volume flux of fluid in m^3s^{-1}, R is the radius of the stream, and R_0 is the radius of the nozzle.

The predictions of equation 5.14 are shown later, with the experimentally measured values, in figure 5.19. It is seen that a cylindrical shape is a reasonable approximation to the shape of the water jets discussed in this work.

5.3.5.3. Experimental Methods and Results

Three experiments are described here. The first was to determine the maximum stable stream lengths which could be produced, the second determined the shapes formed by the falling streams, and the third was a measurement of the fluorescence collected from the falling analyte stream. The description of each experiment is followed by the results of that experiment.

5.3.5.4. Stream stability and shape experiments

To test the predictions of equation 5.12, a number of water streams were established, and their stability estimated using the apparatus shown in figure 5.16. The work described in this section (5.3.5.4) was completed by Jane Hodgkinson at North West Water.

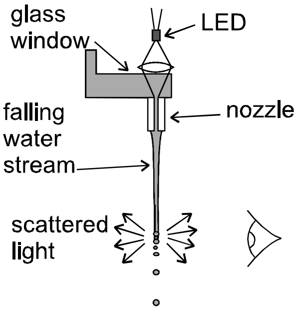

Figure 5.16. The apparatus used to determine the stable length of falling water streams.

Light from an LED was coupled into the top of each stream using a lens. For each nozzle, the water flux was gradually increased, while the point of first break-up of the stream was estimated visually from the right-angle scattered light.

Two extremes of behaviour were observed, believed to correspond to regions of laminar flow and turbulence, with a transition region in between. As the water velocity was increased, the stream's stable length increased, up to a point where the stream length dropped back, breaking up at much shorter lengths. Streams in the low velocity region were more stable than those in the high velocity region, with clearer break-up points. Because in this work only the longest stable streams are of interest, results are presented only for the low velocity region.

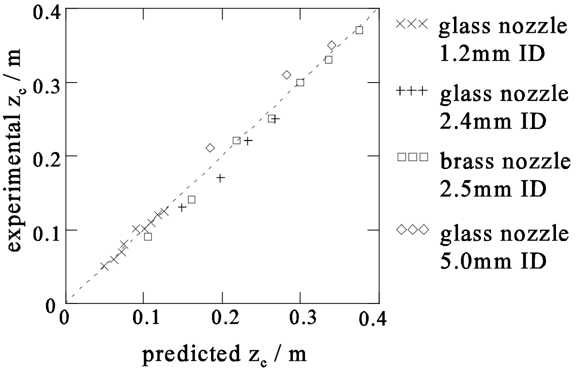

Figure 5.17. Predicted *vs* experimental values of the critical stream length, for a variety of nozzle sizes

Data from low velocity streams were fitted to equation 5.12 using the method of least squares, assuming that the same amplitude ψ_0 would apply in each case, and varying the value of ψ_0 to give the best fit. The critical stream radius, R_c, was calculated using equation 5.14. The agreement between experimental data and predicted values of the critical stream length is shown in figure 5.17. Slight systematic differences between the different nozzles could be explained by either different mechanical roughness, or slightly different nozzle weights, resulting in a different response to external vibrations. Both of these could have affected the amplitude of the initial disturbance (ψ_0).

The shapes of water streams exiting from the nozzles (diameters ≤ 7 mm) were determined for a range of flow rates. The experimental apparatus is shown in figure 5.18.

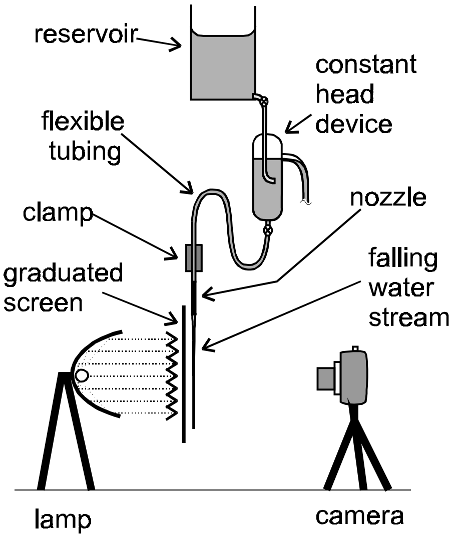

Figure 5.18. The apparatus used to determine the shape of falling water streams. The camera was at a distance sufficient to make parallax error negligible.

The nozzles consisted of approximately 100 mm lengths of cylindrical glass capillary. These thin tubes were sufficiently long to ensure that the fluid exited the nozzle with laminar flow. The capillaries had been cleaved perpendicular to the axis to give a clean, sharp orifice edge. Water streams produced using a variety of nozzle sizes and flow rates were photographed, and measurements were taken from the images using digital calipers. The theory was shown to be valid over the range of diameters and flow rates of interest here, and results are displayed below for two different flow rates Q, and nozzle radii R_0.

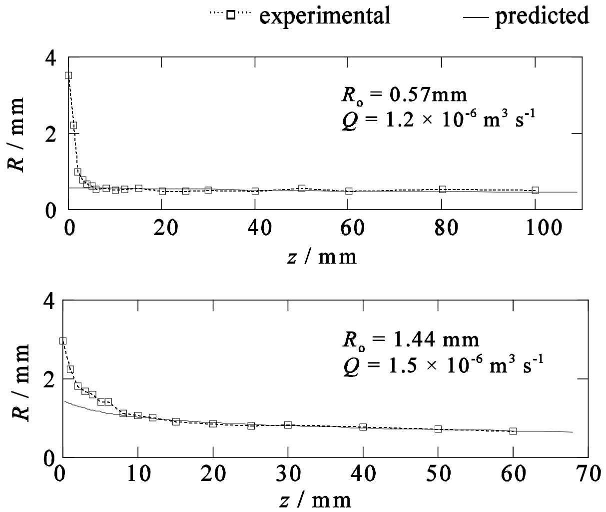

Figure 5.19 The theoretically predicted stream readii *R*, plotted with the measured diameters.

At the top of each stream the water wetted the entire end of the capillary, which was considerably larger than the bore. Therefore, the streams were much wider at the top than equation 5.14 predicts, but the stream radius quickly approached the prediction. This behaviour is not believed to affect the stability of streams at large distances from the nozzle.

Identically shaped nozzles were constructed from different materials in order to test this hypothesis. Tubes of cleaved glass, machined brass and machined PTFE, with identical dimensions, were used to establish water streams under the same conditions. Up to approximately 50 g of Plasticine was attached to each nozzle to reduce the amplitude of vibrations, and to ensure that the nozzle masses were approximately the same in each case. The end of the glass nozzle was fully wetted, the brass nozzle end was partially wetted and the PTFE nozzle end was not wetted at all. Despite these variations, no significant difference between any of the streams could be found, in either their shape at large values of *z*, or their stability.

For the purpose of enhancing fluorescence collection, narrow streams were required, with nozzle bores of 1.0-2.5 mm, it was not practical to produce narrower bore streams. The assumption that the falling stream is cylindrical is most valid for the streams issuing from the smaller nozzles.

5.3.5.5. Fluorescence collection enhancement

A schematic diagram of the equipment used in these experiments is given in figure 5.20. Light was delivered to, and collected from, a falling analyte stream via a multiple optical-fibre bundle (Oxford Electronics, UK). All of the fibres were identical, 95 µm core diameter, 105 µm outer diameter (including the polyimide buffer), step index fibres, with an NA of 0.22. The fibres were bonded into an SMA type ferrule, with the collection fibres were arranged in 3 concentric rings around a single, centrally-located light-delivery fibre. The 6 fibres in the first ring were arranged on a radius of 128 μm, the 13 fibres in the second ring were on a radius of 240 μm, and the 19 fibres in the outer ring were on a radius of 336 μm. The probe tip measured 0.8 mm across. At the other end of the probe cable, the collection fibres (all six fibres from the inner-most ring, 10 fibres from the middle ring, and 10 from the outer ring) were arranged to form a 3 mm vertical array, input to the grating/CCD spectrograph.

30 mW of light at 676 nm was emitted by a laser diode (CorkOpt PC-670-D), and filtered through 2 band pass dielectric stack filters (CVI Corp. F10-676.4-4 and Infra-Red Engineering LDF-670). 10.6 mW of light was delivered by the probe tip. Each measurement was shot noise limited.

Four Falling analyte streams were studied, formed from 30 mm sections of blackened brass capillary tube of approximately 10 mm external diameter, and 1.0 mm, 1.5 mm, 2.0 mm and 2.5 mm internal diameter. The holes were drilled on a lathe, and the nozzles blackened using a commercial brass blackening chemical. The nozzles were inserted 15 mm into the end of a 1.2 m long section of silicone rubber tubing, and held in place by friction. The silicone rubber tube was clamped approximately 10 mm above the nozzle in a vertical translation stage.

The analyte was pumped to a 200 mL header tank approximately 1 m above the nozzle by a peristaltic pump from a reservoir below the nozzle. The level of liquid in the header tank was held essentially constant, by means of an overflow pipe for excess fluid (K in figure 5.20). In this way, pressure fluctuations caused by the pump were minimised. The flow rate was controlled by the valve at the bottom of the header tank (marked L in figure 5.20). This was adjusted to give the longest stable stream possible, and then the flow rate was found by measuring the time taken by the stream to deliver 25 mL of the solution into a 30 mL beaker.

In each experiment, 1 L of 12 μg/L (±4%) fresh Panacryl Blue 5G (330%) solution in de-ionised water was circulated around the flow rig. In order to establish the signal collected by the conventional fibre probe a fluorescent measurement was taken with the bare probe dipped just below the surface of the reservoir before each measurement from the falling analyte stream. (The depth of analyte below the probe was approximately 90 mm for all four measurements. The measured intensity was not affected by the small variations of sample depth between each measurement.)

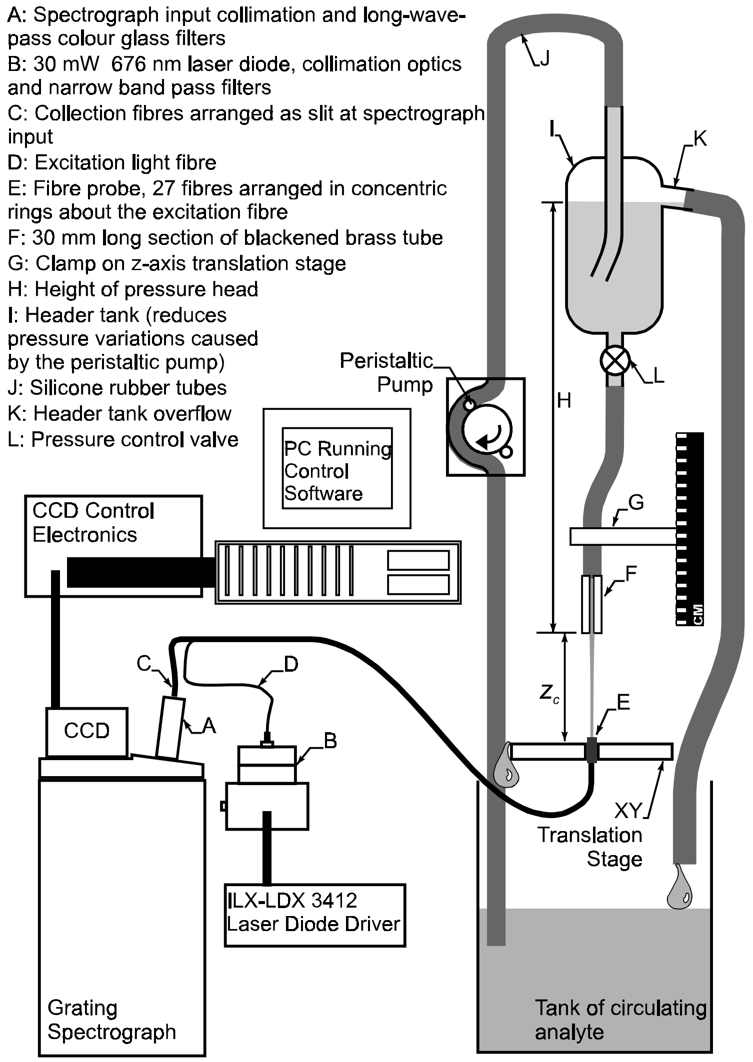

Figure 5.20 A schematic of the complete setup for collecting emitted light from a falling analyte stream.

The optical fibre probe was mounted on an X-Y translation stage, positioned at the base of the falling stream of PB solution, and aligned at the centre of the falling stream. By adjusting the translation stage, the nozzle was butted against the probe tip to establish the position of z=0. The fluorescence collected by the optical fibres was recorded for increasing lengths of stream by retracting the nozzle and then realigning the probe.

The absorbance of Panacryl Blue at 60 mg/L in deionised water was measured using a Perkin-Elmer Lambda-9 spectrophotometer, through a 10 mm path length cuvette, with a cuvette of deionised water in the reference beam. In this way an accurate value of the absorbance coefficient of the 120 µg/L solution could be calculated (as at this weak concentration it was too low to measure directly with any accuracy). It was found that over the measured wavelength range (710 nm to 860 nm) the solution absorbance was that of water. At the incident wavelength, 676 nm, the total solution absorbance coefficient was calculated as 6.1×10^{-3} (absorbance units, cm^{-1}). The wavelength at which the collection enhancement was measured was 740 nm. The literature value[82] for the absorbance coefficient of water at 740 nm, 10.3×10^{-3} cm^{-1}, was used.

5.3.5.6. Fluorescence collection results and analysis

Due to environmental noise in the laboratory, and possibly pressure variations caused by the pump, the stable lengths of falling analyte were shorter than the theoretical maximum. Breaks began to form in streams of length greater than approximately 80 mm, the exact point depending on which nozzle was used. These breaks caused brief reductions or loss of signal collected by the probe as they fell with the analyte. Beyond approximately 100 mm (160 mm for the 2.5 mm diameter nozzle) these breaks became so frequent that it was likely that the intensity of the recorded spectra would be reduced. Data from these unstable regions has not been presented here.

Spectra were recorded over a 150 nm range for each jet length. In figure 5.21, a spectrum recorded with the bare probe is shown, superimposed on that from a 92 mm stream coupled with the probe. The slight distortion around the peak in the case of the 92 mm measurement is due to reabsorption of the fluorescent light by the solution during the longer path length back to the collection optics (the *inner filter effect*).

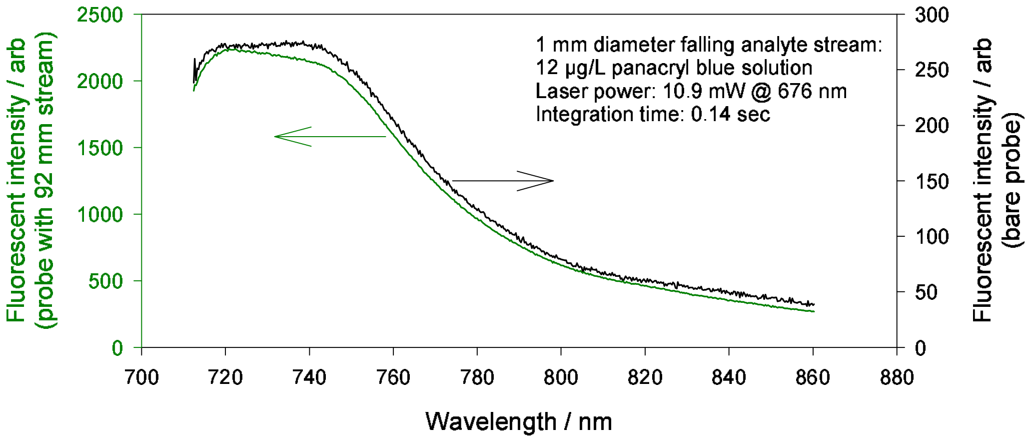

Figure 5.21 The fluorescent spectrum of Panacryl blue 5G in water, measured with a bare fibre probe (upper trace; note the different axes), and with the same probe coupled with a 92 mm length falling analyte stream. The fluorescence was excited by 11 mW at 676 nm..

The enhancement factor *F* (the ratio of the intensity measured by the probe coupled with the falling analyte stream to that measured using the probe alone) has been plotted against stream length in figure 5.22. The enhancement at 740 nm was measured, as this wavelength is close to the emission maximum, and the solution absorbance is low. From the figure it is be seen that, for short stream lengths (less than 10 mm), the falling analyte stream made little difference to the amount of light collected by the fibre probe. The shape of the stream was poorly defined for streams of such short length. With approximately 10 mm between the nozzle and the probe, the falling analyte stream formed a cylinder of liquid over the probe tip, and the enhancement began to rise in proportion to the length of the analyte stream.

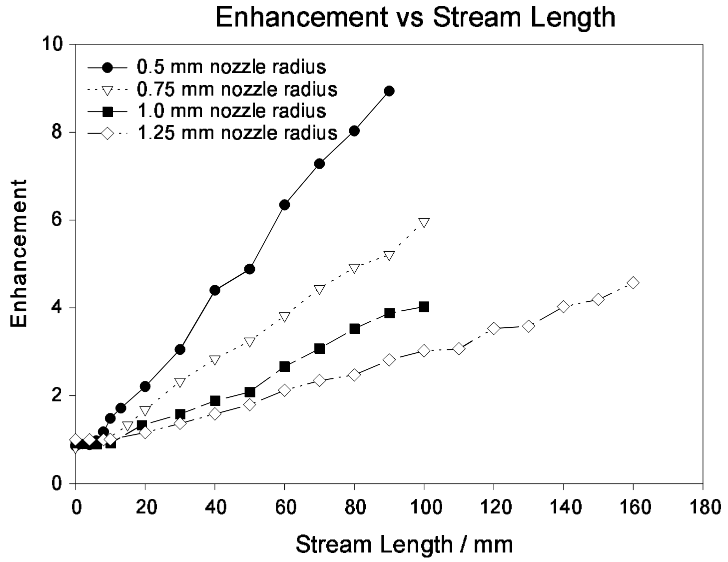

Figure 5.22 Enhancement factors vs stream lengths for nozzle diameters of 1.0 mm, 1.5 mm, 2.0 mm, and 2.5 mm.

It was expected that a deviation from a straight line in these results due, to sample absorbance, would be seen; no such deviation was apparent. It is believed that this is due to the tapered shape of the falling stream, which has the effect that d$\Phi(0)$ is greater for longer streams.

The flow rate, mean square of the radius R of the falling stream between z=10 mm and the maximum stable length (calculated from equation 5.14), and the gradient m of the enhancement(estimated from figure 5.22) are tabulated below. Equation 5.4 suggests that $m{\cdot}(R_{60})^k$ should be constant, which is seen to be the case where k (from equation 5.3) is set equal to 2, *ie* scattering from the surface of the water jet is has randomised the ray paths of light confined within it.

Table 5.1

Nozzle Radius / mm	Probe radius, a / mm	Flow Rate, Q / 10^{-6}m^{3}s	Stream radius squared, R^2/mm^2	Gradient of Enhancement, m / mm	$(m \cdot R^2)$ / 10^{-3}mm^3
0.5	0.775	1.727	0.208	0.0957	27
0.75	0.775	2.269	0.398	0.0527	26
1	0.775	3.181	0.654	0.0364	34
1.25	0.775	4.039	0.848	0.0237	24

5.4. Conclusions

In this chapter, the theory which describes the collection enhancement obtained by coupling an optical fibre probe with a light confining cell has been described. This theory, which was developed during this work, is more complete than the models currently available in the literature, which either rely on simplistic descriptions of the optical-fibre probe used to collect light from the cell[88], or Monte Carlo simulations[86]. Neither of these approaches offer as much physical insight into the situation as the model developed here, which predicts the measured enhancements in terms of the radius and NA of the collection optics, and the refractive index and absorbance of the analyte itself.

The surface quality of all of the light guides has been shown to be critical to their performance as spectroscopic cells: the theoretically perfectly waveguiding AF-coated, and gold-coated, cells displayed large losses due to surface imperfections. More investigation to perfect the deposition of consistently smooth layers of Teflon-AF is needed, but this work has indicated the potential of the material as a cladding to low-refractive-index-liquid core waveguides.

In particular, Teflon-AF fluoropolymer has been shown to form a flexible and stable layer when deposited onto a PTFE substrate. In addition, the use of such a structure to enhance the light collection efficiency from a fluorescent emission measurement has been modelled and demonstrated. The technique is equally suited to measurement of Raman light emission, and it is convenient to couple the cell to an optical fibre probe. A maximum signal enhancement of 3 times was measured in this work, much larger enhancements are expected if surface quality could be improved. The tube which displayed the best waveguiding, and the most linear increase in enhancement with cell length, was the short 0.955 mm internal radius tube; this was the only tube to be coated in one layer, and this may be a pointer towards a better fabrication process.

The best performance of the light-guiding configurations that were investigated in this work was from the falling analyte stream. It was convenient to couple the falling analyte stream to an optical fibre probe, and a signal enhancement of 9 times was measured in this work. There is no reason why further enhancement to the apparatus, such as better vibration isolation, should not increase this value by at least further factor of ten.

6. Conclusions

Techniques of remote spectroscopy via silica optical fibres have been described in this thesis, with consideration to both the applied and theoretical challenges.

A modular, compact, and sensitive spectrograph has been designed and built, and optical fibre probes, and compatible sampling arrangements, have been mathematically modelled and studied experimentally. Dedicated computer control software for instrument control, data collection, and signal processing has been written. By combining each of the elements investigated in this work, a complete system for monitoring a wide range of fluorescent or Raman-active liquid samples could be built. In addition, any of the elements (such as the light guiding cells, or the continuous background subtraction signal processing scheme) could be integrated within alternative monitoring instrumentation.

Analytes have been studied using inelastic scattering (including fluorescent emission) spectroscopy, rather than by absorption techniques, due to the ease of probe construction, relative immunity to elastic scattering (turbidity), and the possibility of making non-contact measurements. The equipment was optimised to measure over a wide spectral range rather than with a high spectral resolution to enable a wide range of analytes to be studied. When monitoring analytes with particularly narrow spectral features (such as Raman lines, which can be less than 1 cm^{-1} (0.05 nm at 700 nm)), then a higher signal-to-noise ratio could be achieved by using a diffraction grating with a greater dispersion. The decreased spectral range could be acceptable if specific analytes were to be monitored, with characteristic features within a small spectral range. (Using a grating with a higher dispersion would offer no advantage if the spectral features were broader than the spectrograph resolution.)

A 676 nm semiconductor laser was chosen as an excitation source, so that a wide range of samples could be studied in a wavelength range of optimum detection efficiency (determined by the detector array responsivity and diffraction grating efficiency) and low aqueous sample absorbance (the absorbance of water increases rapidly beyond 800 nm). The dispersive spectrograph design was based around a concave holographic diffraction grating, with a silicon CCD detector cooled to 0ºC. This combination ensures low stray light levels, high sensitivity, and optimum signal to noise ratio.

The spectrograph was operated under computer control to allow the use of novel data averaging techniques. This involved writing custom software and using a switched sample-channel and reference-channel optical fibre probe, to provide the possibility of improving the signal to noise ratio beyond that possible by signal averaging alone. (By continuously subtracting a current background reading, low-frequency noise within the system can be removed from each measurement; this would not be the case if a previously recorded background signal was subtracted.)

The mathematics of light collection from a parallel-optical-fibre probe has been developed, and the derived mathematical model applied to a number of common optical-fibre-probe configurations. These model predictions were shown to be accurate within experimental uncertainty: in particular, more accurate than the models put forward previously in the literature, most recently by Zhu and Yappert[77][78], and by Cooney[75]. The model is applicable to single fibre probes, as well as multiple-fibre probes formed from dissimilar optical fibres. It has been shown to be capable of accurate quantitative predictions, as well as qualitatively describing the performance of optical-fibre probes, and has been tested over a wide range of sample absorbances and fibre separations, as well as with different sample refractive indices or fibre numerical aperture.

None of the previous studies of the problem found in the literature have given any consideration to absorbing samples, or have described such an extensive or well controlled study of the effect of the axial separation between the emission and collection optical fibres. There was also no work which directly compared the mathematical prediction of the absolute collection efficiency of the optical fibre probes with measured values. By using a literature value of the Raman scattering cross section of toluene, the measured collected light intensity was found to agree within experimental error to the prediction of the model described in this thesis.

The mathematical model to describe coupling optical-fibre probes to cylindrical light-guides has also been tested against experimental results, using four distinct types of light guide. This model has also been shown to be both valid through a wide range of experimental measurements, and also more complete than other published models, which either rely on simplistic descriptions of the optical-fibre probe used to collect light from the cell[88], or Monte Carlo simulations[86].

The surface quality of low-index-polymer-clading light guides has been shown to be critical to their performance as spectroscopic cells. More investigation to perfect the deposition of consistently smooth layers of Teflon-AF is needed, but the work described in this thesis has indicated the potential of the material as a cladding for low-refractive-index-liquid core waveguides. In particular, Teflon-AF fluoropolymer has been shown to form a flexible and stable layer when deposited onto a PTFE substrate. In addition, the use of such a structure to enhance the light collection efficiency from a fluorescent emission measurement has been modelled and demonstrated.

The most efficient and best performing of the light-guiding configurations that were investigated in this work was the falling analyte stream. It was convenient to couple the falling analyte stream to an optical fibre probe, and a high light confinement is achievable with any liquid, not just those with refractive index greater than 1.47. Surface fouling problems are minimised, as are problems with the analysis of reactive or corrosive liquids.

A signal enhancement of 9 times was measured in this work. Further enhancement to the apparatus, such as better vibration isolation, could potentially increase this value by at least a further factor of ten.

6.1. Possibilities for Future Work

The possibilities for further application of this work are as numerous as the number of analytes that are amenable to optical spectroscopic analysis. Some specific suggestions for the further development of this work, and in the light of the experience and knowledge gained from it, are made here.

The referenced cell subtraction software has not been fully evaluated, due to problems with cracks in the particularly fragile optical fibres used in the probe bundles; time did not permit the reassembly of the bifurcated bundle for proper evaluation. Fuller investigation and analysis is warranted to demonstrate the drift reduction and *S/N* ratio enhancement achievable using this technique, which will depend on the type of optical detector used. The particular configuration described in this thesis relies on alternate measurements between the reference cell and signal cell. An immediate saving in measurement time could be made if the CCD detector was used in an imaging mode, so that the signals from the two cells could be measured concurrently. This was not possible during this work because the CCD detector was hard-wired in a 1-dimensional configuration (all of the pixels in each column are summed together).

Although experimental measurements have shown that the parallel-fibre-probe light-collection model is accurate within experimental error in its prediction of the region of space from which most light is collected, there are slight deviations between the mathematical predictions and experimental results (figure 4.10). This deviation is ascribed to leaky fibre modes, and the inclusion of these modes would make the mathematical model complete. This could be achieved by making the upper limit of ϕ in equation 4.7 a function of the distance between the point at which a ray strikes the collection fibre and the centre of the fibre end face. This is a complex problem, and is likely to considerably increase the time required to calculate the numerical integrals.

The parallel-fibre-probe model predicts the region of space from which most light will be collected by an optical fibre probe. This information is valuable when coupling indicator films with optical fibre probes, as the optimum position for the optically active layer can be identified without any experimental trial and error.

Further investigation of the methods of depositing Teflon-AF on to the internal surface of capillary tubing to achieve a smooth polymer layer would be valuable, because such a light guide would form a more efficient sample cell. An alternative technique, of pulling a tube of the low-index polymer by a similar technique to that used for pulling silica capillary tube was ruled out during this work on cost grounds, however, this approach may be appropriate if this work was to be taken further. PTFE tubing has already been pulled in such a manner at the ORC.

Work towards stabilising the water jet could yield an order of magnitude improvement in collection efficiencies where the analyte absorbance does not limit the amount of light collected. This work is developmental, but nevertheless valuable, if it was hoped to apply the technique in a more routine manner.

References

1. Boisdé G and Harmer A; “Chemical and Biochemical Sensing with Optical Fibers and Waveguides”; Artech House, Norwood, MA. 1996.

2. Wolfbeis OS (Editor); “Fiber Optic Chemical Sensors and Biosensors Volume 2”; CRC Press, Boca Raton, FL. 1991.

3. Dakin, J P and Culshaw B; “Optical Fiber Sensors Applications, Analysis and Future Trends Volumes 1-4”; Artech House, Norwood, MA. 1997.

4. Hirshfeld T, Deaton T, Milanovich FP and Klainer SM; “The feasibility of using fiber optics for monitoring ground water contaminants”; Optical Engineering, 22, 527-531. 1983.

5. Boisdé G, Blanc F, Mauchien P and Perez JJ; “Fiber optic chemical sensors in nuclear power plants”; Fiber Optic Chemical Sensors and Biosensors, volume 2” (edited by Wolfbeis OS), chapter 14, 135-149, CRC Press, Boca Raton. 1991.

6. Gantner E and Steinert D; “Applications of laser Raman spectrometry in process control using optical fibers”; Fresenius Journal of Analytical Chemistry, 338, 2-8. 1992.

7. Thorne AP; “Spectrophysics” (2nd Ed), Chapman and Hall Ltd (London). 1988.

8. Heitmann W; “Attenuation analysis of silica-based single-mode fibers”, Journal of Optical Communications, 11, 122-129. 1990.

9. Senior JM; “Optical Fibre Communications Principles and Practice” (2nd ed), Prentice Hall International (UK) Ltd, Hemel Hempstead. 1992.

10. Proceedings of SPIE - The International Society for Optical Engineering, 1681, “Optically Based Methods for Process Analysis”, Somerset, NJ, USA, Mar 23-26, (Conf. code 17498). 1992.

11. Proceedings of SPIE - The International Society for Optical Engineering, 2365, “Optical Sensing for Environmental and Process Monitoring”, McLean, VA, USA, Nov 7-10, (Conf. code 22254). 1994.

12. Boisdé G, Blanc F, Perez JJ; “Chemical measurements with optical fibers for process control”, Talanta, 35, 75-82. 1988.

13. Freeman JE, Childers AG, Steele AW, Hieftje GM; “A fibre-optic based sensor for bioanalytical absorbance measurements”, Analytical Chemistry, 56, 2246-2249. 1985.

14. Nave SE, O’Rourke PE, Toole WR; “Sampling probes enhance remote chemical analyses”, Laser Focus World, 83-87. December 1995.

15. FCI Environmental, Inc; 1181 Grier Drive, Las Vegas, Nevada. (Geotechnical Instruments, in UK).

16. Coleman JT, Eastham JF, Sepaniak MJ; “Fiber-optic based sensor for bioanalytical absorbance measurements”, Analytical Chemistry, 56, 2246-2249. 1984.

17. Polanyi ML; “In Vivo Oximeter with Fast Dynamic Response”; Review of Scientific Instruments, 22, 1050. 1962.

18. Hodgkinson J; “Photoacoustic and Photothermal Detection of Trace Contaminants in Water”; PhD Thesis, University of Southampton. 1998.

19. Sontag H and Tam AC; “Optical detection of nanosecond acoustic pulses”, IEE Transactions on Ultrasonics, Ferroelectrics and Frequency Control, vol UFFC-33, 500-506. 1986.

20. Hand DP, Hodgson P, Carolan TA, Quan KM, Mackenzie HA, and Jones JDC; “Detection of photoacoustic waves in liquids by fibre-optic interferometer”, Optics Communications, 104, 1-6. 1993.

21. Hand DP, Freeborn S, Hodgson P, Carolan TA, Quan KM, Mackenzie HA and Jones JDC; “Optical fiber interferometry for photoacoustic spectroscopy in liquids”, Optics Letters, 20, 213-215. 1995.

22. Tam AC; “Applications of photoacoustic sensing techniques”, Reviews of Modern Physics, 58, R83-R121. 1986.

23. Bohnert B, Faubel W, and Ache HJ; “Comparison of collinear and transverse photothermal deflection spectroscopy for trace analysis of pesticides in water”, Fresenius Journal of Analytical Chemistry, 343, 513-517. 1992.

24. Klainer S, Hirschfeld T, Bowman HR, Milanovich FP, Perry D, and Johnson D; “A monitor for detecting nuclear waste leakage in a sub-surface repository”, Report, Livermore-Berkeley Laboratory. 1981.

25. Chudyk WA, Carrabba MM, Kenny JE; “Remote detection of Ground water contaminants using far-ultraviolet laser induced fluorescence”, Analytical Chemistry, 57, 1237. 1985.

26. Berlman IB; “Handbook of Fluorescent Spectra of Aromatic Molecules, 2nd Ed”, Academic Press, New York. 1974.

27. Bublitz J, Dickenhausen M, Gräz M, Todt S, Schade W; “Fiber-optic laser-induced fluorescence probe for the detection of environmental pollutants”, Applied Optics, 34, 3223. 1995.

28. Panne U, and Neissner R; “A fibre-optical sensor for polynuclear aromatic hydrocarbons, based on multidimensional fluorescence”, Sensors and Actuators B, B13-14, 288. 1993.

29. Hillrichs G, Karlitschek P, Neu W; “Fiber optic aspects of UV laser spectroscopic in situ detection of water pollutants”, SPIE Proceedings Vol. 2293, Chemical, Biochemical, and Environmental Fiber Sensors VI, 07/24 - 07/29/94, San Diego, CA, USA. 1994.

30. Dmitriev VG, Gurzadyn GG, Nikogosyan DN; “Handbook of Nonlinear Optical Crystals”, Springer. 1991.

31. Demas JN and Keller RA; “Enhancement of luminescence and Raman spectroscopy by phase-resolved background suppression”, Analytical Chemistry, 57, 539. 1985.

32. Chike KE, Myrick ML, Lyon RE, and Angel SM ; “Raman and near-infrared studies of an epoxy resin”, Applied Spectroscopy, 47, 1631. 1993.

33. Lombardi DR, Mann CK, Vickers TJ; “Determination of water in slurries by fiber-optic Raman spectroscopy”, Applied Spectroscopy, 49, 220-224. 1995.

34. Willis HA, van der Maas JH, Miller RGJ [Eds]; “Laboratory Methods in Vibrational Spectroscopy, Third edition”, John Wiley and Sons. 1987.

35. Hollas JM; “Modern Spectroscopy, Second Edition”, Wiley. 1992.

36. Jeffry A; “Mathematics for Engineers and Scientists”, Van Nostrand Reinhold International, London, p. 363. 1989.

37. Rosser WGV; “An Introduction to Statistical Physics”; Ellis Horwood, Chichester, 249. 1982.

38. Hecht E; “Optics, second edition”, Addison-Wesley Publishing Company, MA. 1987.

39. Szymanski HA; “Raman Spectroscopy Theory and Practice”, Plenum Press. 1967.

40. Marshall BR, Smith RC; “Raman scattering and in-water ocean optical properties”, Applied Optics, 29, 71. 1990.

41. Davies PCW; “Quantum Mechanics”, Chapman and Hall. 1984.

42. Halliday D, Resnick R; “Fundamentals of Physics, 2nd ed”, Wiley. 1981.

43. Guenault AM; “Statistical Physics”, Routledge. 1988.

44. Wolfbeis, OS [Ed]; “Fiber Optic Chemical Sensors and Biosensors Volume I”, CRC Press. 1991.

45. Schrötter HW and Klöckner HW; “Raman Spectroscopy of Gases and Liquids [edited by Weber, A]”, Springer-Verlag, 123-66. 1979.

46. Eysel, HH and Bertie, JE; “Raman intensities of liquids: Precise relative measurement of some potential secondary standards, and an interim scale of absolute intensities for blue and green excitations”, Journal of Raman Spectroscopy, 19, 59. 1988.

47. Skinner JG and Nilsen WG; “Absolute Raman scattering Cross-section measurement of the 992 cm^{-1} line of benzene”, Journal of the Optical Society of America, 58, 113. 1968.

48. Eysel HH, Lipponer KG, Oberle C, Zahn I; “Raman intensities of liquids: Absolute scattering activities and electro-optical parameters of the halate ions ClO_3^-, BrO_3^-, and IO_3^- in aqueous solutions”, Spectrochimica Acta, 48A, 219. 1992.

49. Fischer WB, Fischer WB, Eysel HH, Nielsen OF, Bertie JE; “Corrections to the baseline distortions in the OH-stretch region of aqueous solutions”; Applied Spectroscopy, 48, 107. 1994.

50. Hofmann, W, Moser, H; Ber. Bunsenges. Physik. Chem., 68, 129. 1964

51. Barletta, RE and Veligden, JT; “Resonance Raman spectrum of carbon tetrachloride”; Applied Spectroscopy, 49, 532. 1995.

52. Potts WJ; “Low-temperature absorption spectra of benzene, toluene, and para-xylene in the farther ultraviolet region”, Journal of Chemical Physics, 23, 73. 1955.

53. Katzin LI; “Regularities in the absorption spectra of halides”, Journal of Chemical Physics, 23, 2057. 1955.

54. Fleischmann M, Hendra PJ, and McQuillan AJ; “Raman spectra of pyridine adsorbed at a silver electrode”, Chemical Physics Letters, 26, 163. 1974.

55. Albrecht MG, and Creighton JA; “Anomalously intense Raman spectra of pyridine at a silver electrode”, Journal of the American Chemical Society, 99, 5215. 1977.

56. Garrell RL; “Surfce enhanced Raman spectroscopy”, Analytical Chemistry, 61, 401A. 1989.

57. Chang RK, and Furtak TE (Eds); “Surface enhanced Raman scattering”, Plenum Press. 1982.

58. Allen CS, Schutz GL, and Van Duyne RP; “Tunable laser excitation profile of surface enhanced Raman scattering from pyridine adsorbed on a copper electrode”, Chemical Physics Letters, 75, 201. 1980.

59. Alak AM, and Vo-Dinh T; “Surface enhanced Raman spectrometry of chlorinated pesticides”, Analytica Chimica Acta, 206, 333. 1988.

60. Storey JME, Shelton RD, Barber TE, and Wachter EA; “Electrochemical SERS detection of chlorinated hydrocarbons in aqueous solutions”, Applied Spectroscopy, 48, 1265. 1994.

61. Carron K, Peitersen L, and Lewis M; “Octadecylthiol-modified surface-enhanced Raman-spectroscopy substrates - A method for the detection of aromatic compounds”, Environmental Science and Technology, 26, 1950. 1992.

62. Lloyd CJ, Perkins AE, and Carr RJG; “Dynamic Light Scattering and its Application in Concentrated Suspensions”;Optical Fibre Sensors Applications, Analysis, and Future Trends Volume Four, Editors: Dakin JP and Culshaw B; Artech House Inc, Norwood, MA, 109-127. 1997.

63. Hecht E; “Optics Second Edition”; Addison-Wesley, Reading, MA, pp94-104. 1987.

64. Hecht E; “Optics Second Edition”; Addison-Wesley, Reading, MA, pp 375-376. 1987.

65. Lerner JM, and Thevenon A; “The Optics of Spectroscopy”, Instruments SA Inc. 1988.

66. Bar-Lev A; “Semiconductors and Electronic Devices, 2nd Ed”, Prentice Hall. 1984.

67. O'Malley M, and O'Mongain Eon; “Charge-coupled devices: frame adding as an alternative to long integration times and cooling”, Optical Engineering, 31, 3, 522-526. 1992.

68. Ott H W; “Noise Reduction Techniques in Electronic Systems, Second Edition”, Wiley, New York, Chapters 2 and 3. 1988.

69. Horowitz P, and Hill W; “The Art of Electronics, second edition”, Cambridge University Press, UK, 457-462. 1989.

70. Angel SM, and Myrick ML; “Wavelength selection for fiber optic Raman spectroscopy, part 1”; Applied Optics, 29, 1350. 1990.

71. Fryling M, Frank CJ, and McCreery RL; “Intensity Calibration and Sensitivity Comparisons for CCD/Raman Spectrometers”, Applied Spectroscopy; 47, 12, 1965-1974. 1993.

72. Myrick ML, and Angel SM; “Elimination of background in fiber-optic Raman measurements”, Applied Spectroscopy, 44, 565. 1990.

73. Ma J, and Ying-Sing L; “Fiber Raman background study and its application in setting up optical fiber Raman probes”, Applied Optics, 35, 2527-2533. 1996.

74. Plaza P, Dao NQ, Jouan M, Fevrier H, and Saisse H; “Simulation et optimisation des capteurs à fibres optiques adjacentes”, Applied Optics; 25, 3448-3454. 1986.

75. Cooney TF, Skinner HT, and Angel SM; “Comparative Study of Some Fiber-Optic Remote Raman Probe Designs”, Applied Spectroscopy 50, 836-848. 1996.

76. Schwab SD, and McCreery RL; “Versatile, Efficient Raman Sampling with Fiber Optics”, Analytical Chemistry, 56, 2199-2204. 1984.

77. Zhu ZY, and Yappert MC; “Determination of Effective Depth and Equivalent Pathlength for a Single-Fiber Fluorometric Sensor”, Applied Spectroscopy, 46, 912-918. 1992.

78. Zhu ZY, and Yappert MC; “Determination of Effective Depth and Equivalent Pathlength for Double-Fiber Fluorometric Sensors”, Applied Spectroscopy; 46, 919-924. 1992.

79. Snyder AW, and Love JD; “Optical Waveguide Theory”, chapter 24, Chapman & Hall, London, UK. 1983.

80. Graham JD, Graham C, and Whitcombe A; “A-level Mathematics: Course Companion — 2nd edition — Letts Study Aids”; Charles Letts & Co Ltd, London, p 42. 1988.

81. Dakin JP; “Loss Measurements in Glass and Glass-Fibre Optical Waveguides”; PhD thesis, Southampton University, 191. 1974.

82. Smith RC, and Baker KS; “Optical properties of the clearest natural waters (200-800 nm)”, Applied Optics, 20, p 177. 1981.

83. Hale GM, and Querry MR; “Optical constants of water in the 200 nm region”, Applied Optics, 12, p 555. 1973.

84. “Tables from The Schott Optical Glass Catalogue No. 3111”. 1986.

85. Walrafen GE and Stone J; “Intensification of Spontaneous Raman Spectra by use of Liquid Core Optical Fibers”, Applied Spectroscopy, 22, 585. 1972.

86.Tunnicliff DD and Jones AC; “A multiple-pass Raman cell for liquids”, Spectrochimica Acta; 18, 569-578. 1962.

87. Dyer CD, and Hendra PJ; “Near-infrared Fourier transform Raman spectroscopy of gases”, Analyst, 117, 1393. 1992.

88. Zhu ZY and Yappert MC; “Sensitivity enhancement in capillary/fiber-optic fluorometric sensors”, Analytical Chemistry, 66, 761. 1994. (Also see quoted references.)

89. Benoit V, and Yappert MC; “Effect of Capillary Properties on the Sensitivity Enhancement of Capillary/Fiber Optical Sensors”, Analytical Chemistry, 68, 183-188. 1996.

90. Senior JM; “Optical Fibre Communications Principles and Practice Second Edition”, Prentice Hall International (UK), Hemel Hempstead, UK, p. 222. 1992.

91. Brady JE, and Holum, JR; “Fundamentals of Chemistry, third edition”, John Wiley and Sons. 1988.

92. Hecht E; “Optics, second edition”, Addison-Wesley, Reading MA, 95-96 and 102. 1987.

93. Buck WH, and Resnick PR; “Properties of amorphous fluoropolymers based on 2,2-bistrifluoromethyl-4,5-difluoro-1,3-dioxole”, 183rd Meeting of the Electrochemical Society, Honolulu, HI, May 17 1993. (Available from Du Pont.)

94. Lowry JH, Mendlowitz JS, and Subramanian NS, “Optical characteristics of Teflon AF fluoroplastic materials”, Optical Engineering, 31, pp. 1982-1984. 1992.

95. Mackenzie S J, and Dakin J P, “Internally Teflon AF coated capillary cell for optical-fibre remote spectroscopy”, Presented at CLEO-Europe/EQEC’96, Hamburg, Germany, September 1996.

96. Hecht E; “Optics, second edition”, Addison-Wesley, Reading MA, 107. 1987.

97. Hecht E; “Optics, second edition”, Addison-Wesley, Reading MA, 113. 1987.

98. Weber C; “Zeitschrift für Angewandte Mathematik und Mechanik”, 2, 136. 1931.

99. Anno JN; “The mechanics of liquid jets”, DC Heath. 1977.